

Modelling of Streamer Breakdown in Air Under Positive Polarity HVDC in Subtropical Conditions

Keshlan Moodley

15th December 2021

In fulfilment of the Master of Science, College of Agriculture, Engineering and Science, University of
KwaZulu-Natal

Supervisor: Dr AG Swanson

COLLEGE OF AGRICULTURE, ENGINEERING AND SCIENCE

DECLARATION 1 - PLAGIARISM

As the candidate's supervisor, I agree to the submission of this dissertation.

Name: Dr AG Swanson.....

Signed:

Date: 14th December 2021..

I, Keshlan Moodley....., declare that

1. The research reported in this thesis, except where otherwise indicated, is my original research.
2. This thesis has not been submitted for any degree or examination at any other university.
3. This thesis does not contain other persons' data, pictures, graphs or other information, unless specifically acknowledged as being sourced from other persons.
4. This thesis does not contain other persons' writing, unless specifically acknowledged as being sourced from other researchers. Where other written sources have been quoted, then:
 - a. Their words have been re-written but the general information attributed to them has been referenced
 - b. Where their exact words have been used, then their writing has been placed in italics and inside quotation marks, and referenced.
5. This thesis does not contain text, graphics or tables copied and pasted from the Internet, unless specifically acknowledged, and the source being detailed in the thesis and in the References sections.

Signed:

Acknowledgements

Throughout the writing of this dissertation, I received a great amount of support and assistance.

First and foremost, I am extremely grateful to my supervisor, Dr Andrew Swanson for his invaluable advice, continuous support, and patience throughout my Master's dissertation. His immense knowledge as well as vast amount of experience has motivated me substantially whilst performing my academic research and in my daily life.

In addition, I would like to thank my parents (Logan Moodley and Devika Moodley) as well as my sister (Deshini Moodley) for their wise counsel and whose love and guidance are with me in whatever I pursue.

Finally, I would like to praise and thank God, the Almighty, who has granted countless blessings, knowledge, and opportunities to me, so that I have been finally able to accomplish this dissertation.

Abstract

Atmospheric air is an essential component in high voltage power systems as it is used to provide electrical insulation. Therefore, it is required that research is extensively performed on the gaseous insulator to ensure reliability of the system. This dissertation presents the research that has been performed on the streamer breakdown of needle-plane air gaps that were less than 15 cm in length.

An experiment was conducted to investigate the streamer breakdown in air gaps. The investigation also included determining the influence of humidity and pressure on the breakdown voltage when HVDC is applied to the high voltage electrode in subtropical conditions. The results indicated that humidity did not influence the breakdown voltage for small gap lengths but both humidity and pressure have a directly proportional relationship with the breakdown voltage of air gaps longer in length. It was observed in the results that the breakdown voltage reduced in magnitude when the humidity increased, and this could have been a result of the breakdown developing out of the glow discharge without impulses when the HVDC was applied. It was observed that the atmospheric pressure did not influence the breakdown voltage for the smaller gap lengths, but the breakdown voltage was directly proportional to the pressure for larger gap lengths.

High-speed photography was implemented in the experiment to capture the streamer breakdown mechanism that occurred in these air gaps. An analysis of the results obtained from the experiment showed that the needle-plane electrode combination created single, straight streamers whose stem increased in length when the gap length increased. Branches would also occur from the streamer when the gap length was greater than or equal to 12 cm and the streamer would occasionally take a bent path for gap lengths greater than 10 cm when propagating towards the cathode. Streamers would take this bent path because of space charge being present along the normal path when propagating towards the cathode. This caused the streamer to propagate around the space charge as it is unable to propagate through regions of high concentration.

The dissertation also consisted of a numerical simulation on COMSOL Multiphysics which modelled the initiation of a cathode directed streamer and the propagation of it in an air gap. The necessary steps that were taken for the implementation and simulation of the electrical streamer in a 0.1 cm needle-plane gap is also included. The results of the numerical simulation were presented and analysed. The model was used to investigate the influence of both humidity and pressure on the breakdown voltage. The results indicated that the breakdown voltage of an air gap increased when humidity increased in the system as the atmospheric pressure was controlled. The breakdown voltage is also directly proportional to the atmospheric pressure when the humidity in the system was controlled.

The experimental results and the numerical results obtained indicate that the breakdown voltage of an air gap is dependent on the humidity and pressure of the system and that space charge influences the path a streamer takes when propagating to the cathode.

Contents

Acknowledgements	ii
Abstract	iii
Contents	v
List of Figures	x
List of Tables	xiv
Acronyms	xvi
1 Introduction	1
1.1 Research Question	2
1.2 Hypothesis	2
1.3 Importance of Study and Contribution	2
1.4 Dissertation Structure	3
2 Literature Review	4
2.1 Atmospheric Air	4
2.2 Sulphur Hexafluoride	5
2.3 The 4 th State of Matter: Plasma	6
2.3.1 Collisional Plasma	6
2.3.2 Weakly Ionized Plasma	6
2.4 Gaseous Reactions	7
2.4.1 Collisions	7
2.4.2 Elastic Collisions	7
2.4.3 Inelastic Collisions	8
2.4.4 Ionization Reactions	8
2.4.5 Photoionization	9
2.4.6 Background Ionization	9
2.4.7 Excitation Reactions	9
2.4.8 Electron Attachment Reactions	10
2.4.9 Three Body Collisions	10
2.4.10 Electric Field	10

2.4.11	Electron Mobility	11
2.4.12	Diffusion	11
2.4.13	Electron Temperature	12
2.5	Breakdown Mechanisms in Gases	12
2.5.1	Townsend Mechanism	13
2.5.2	Secondary Effects.....	14
2.5.3	Townsend's Second Ionization Coefficient.....	15
2.5.4	Streamer Mechanism.....	16
2.5.5	Positive (Cathode Directed) Streamers	17
2.5.6	The Positive Streamer Breakdown Mechanism	18
2.5.7	Streamer Inception	20
2.5.8	Electrode Configuration for Streamer Initiation	20
2.5.9	The Different Types of Streamer Breakdown	21
2.5.10	The Influence of Atmospheric Conditions on the Breakdown Voltage.....	23
2.5.11	Electrode Influences on the Breakdown Voltage	24
2.6	Swarm Parameters Implemented for the Numerical Simulation of a Positive Streamer.....	25
2.6.1	Collisional Cross Sections.....	25
2.6.2	Electron Impact Reactions	26
2.6.3	LXCAT Database	28
2.6.4	The Cross Section Analysis of Nitrogen, Oxygen and Water.....	29
2.6.5	BOLSIG+	32
2.6.6	Data Requirements for BolSig+ Simulation	34
2.7	Results of the BolSig+ Simulation	36
2.7.1	Mobility	36
2.7.2	Diffusion	37
2.7.3	Townsend Ionization and Attachment Coefficients	37
2.7.4	Effective Ionization Coefficient	38
3	Streamer Breakdown of Air Experiment	40
3.1	Experimental Setup.....	42

3.1.1	Experimental Procedure Layout.....	42
3.1.2	Oscilloscope	44
3.1.3	Phantom Miro M110 High Speed Camera	45
3.1.4	Experimental Test Procedure	46
3.2	Results	47
3.2.1	Comparisons of Breakdown Voltage to the Gap Length Between Electrodes	47
3.2.2	Electric Field Strength.....	48
3.2.3	Comparisons of Breakdown Voltage to the Absolute Humidity	49
3.2.4	Comparisons of Breakdown Voltage to Pressure.....	50
3.2.5	Comparisons of Breakdown Voltage to Temperature	51
3.2.6	The Formation of a Positive Streamer Using High Speed Photography	52
3.2.7	The Influence of Gap Length on the Appearance of Streamers	53
3.2.8	The Influence of Pressure on the Appearance of Streamers	56
3.2.9	The Bent Path a Cathode Directed Streamer Takes	57
3.3	Chapter Summary	60
4	Numerical Simulation of a Cathode Directed Streamer in Air	62
4.1	Plasma Interface in COMSOL Multiphysics.....	64
4.1.1	Drift Diffusion Equations Used for Plasma Modelling.....	64
4.1.2	Transport Settings	67
4.1.3	Transport Mechanisms and Plasma Properties	67
4.2	Geometry	69
4.3	Plasma Chemistry	70
4.3.1	Electron Impact Reactions	70
4.3.2	Reactions	71
4.3.3	Electron Mobility and Diffusivity	72
4.3.4	Reduced Electric Field vs Mean Electron Energy	72
4.4	Initial Conditions	72
4.4.1	Plasma Cloud	72
4.4.2	Electric Potential	74

4.5	Voltage.....	75
4.6	Background Ionization	76
4.7	Meshing	76
4.8	Study Settings	78
4.9	Results of Simulation.....	79
4.9.1	Parameters and Variables Implemented	79
4.9.2	Electron Density	81
4.9.3	Electric Field Distribution	84
4.9.4	Electric Potential	86
4.9.5	Electric Current	87
4.9.6	Mean Electron Energy.....	88
4.9.7	Positive and Negative Ion Density	89
4.9.8	A Comparison of Breakdown Voltage to Relative Humidity Using COMSOL Multiphysics	91
4.9.9	A Comparison of Breakdown Voltage to Pressure Using COMSOL Multiphysics	93
4.10	Chapter Summary	94
5	Conclusion	96
5.1	Recommendations	97
6	References	99
	Appendix A	111
	Tabulated Results Obtained from the Bolsig+ Simulation	111
	MATLAB Code Used for the Calculation of the Effective Ionization Coefficient	112
	Appendix B	113
	HVDC Generator	113
	Calibration of Haefely Hipotronics Vertical Sphere Gap System	114
	The Procedure of Atmospheric Correction	115
	Tabulated Results Obtained in the Experiment.....	117
	Day 1	117
	Day 2.....	119

Day 3	120
Day 4	121
Appendix C	122
Numerical Simulation of a 2 cm Air Gap	122
Numerical Instabilities Observed.....	123

List of Figures

Figure 1 - The development of an electron avalanche that occurs from one free electron when there is an electric field applied [36].	13
Figure 2 - A parallel plate capacitor that has a gaseous insulating medium and is separated by a distance d [12].	13
Figure 3 - The change in current that results from an increase in voltage [12].	14
Figure 4 - The change in the gap current with gap length in a uniform E [12].	15
Figure 5 - An illustration of the Townsend breakdown mechanism. (i) – The ejection of the electron from the cathode is seen. (ii) – Multiple avalanches are generated. (iii) – After 4 generations there is a build-up of positive space charge by the anode. (iv) – An electrical breakdown by constriction takes place because of this [36].	16
Figure 6 - The distribution of charge carriers in an avalanche and its contribution to the applied uniform electric field. It should be noted that $E_1 > E$, $E_2 < E$ and $E_3 > E$ [32].	17
Figure 7 - Primary electrons from the avalanche that are being swept into the anode [36].	18
Figure 8 - Secondary avalanche being fed into the primary avalanche [36].	19
Figure 9 - A self-propagating streamer that causes electrical breakdown [36].	19
Figure 10 - An illustration of the various streamer breakdown mechanisms that occurs in an air gap [18]. (i) – Arrested streamer mechanism. (ii) – The stem mechanism. (iii) – The secondary streamer mechanism.	22
Figure 11 - Plot of the cross sections for electrons interacting with Nitrogen [70]. Take note that both the x-axis and y-axis are on a log scale.	29
Figure 12 - Plot of the cross sections for electrons interacting with Oxygen [71]. Take note that both the x-axis and y-axis are on a log scale.	30
Figure 13 - Plot of the cross sections for electrons interacting with water [72]. Take note that both the x-axis and y-axis are on a log scale.	31
Figure 14 - Plot of the electron mobility as a function of the reduced electric field [61]. Both the x-axis and y-axis are on a log scale.	36
Figure 15 - Plot of the diffusion coefficient as a function of the reduced electric field [61].	37
Figure 16 - Plots of the Townsend ionization and Townsend attachment coefficient as a function of the reduced electric field [61]. It should be noted that the y-axis is only on a log scale.	38
Figure 17 - Plot of the effective ionization coefficient as a function of the reduced electric field [61]. It should be noted that the y axis is on a log scale.	39
Figure 18 - The layout for the experimental procedure: (i) – HVDC control unit, (ii) – HVDC generator, (iii) – High voltage needle electrode, (iv) – Grounded plane electrode, (v) – High voltage measurement system, (vi) – Oscilloscope, (vii) – High speed camera (viii) – Computer	42

Figure 19 - The needle-plane electrode configuration implemented in the experimental procedure: (i) – High voltage needle electrode, (ii) – Varied gap distance , (iii) – Grounded plane electrode.....	43
Figure 20 - The Haefely Hipotronics vertical sphere gap system with its control unit for autonomous operation. The control unit is set to 1 162 mm which represents a gap length of 15 cm between the high voltage and grounded electrode.	44
Figure 21 - A Yokogawa DL9140 digital oscilloscope. The image on the right indicates that electrical breakdown has occurred in the air gap as the applied voltage has collapsed.	44
Figure 22 - The experimental setup that was implemented with the inclusion of a high-speed camera for recording the streamer breakdown of various air gaps. The cage that was designed and fabricated to protect the camera from an arc discharge is also seen.	45
Figure 23 - The results obtained from the experimental procedure indicating the different breakdown voltages of various air gap lengths obtained over the course of 4 days.....	47
Figure 24 - A FEMM model showing the electric field created between a needle and plane electrode in air. The electrodes are separated by a distance of 2 cm and a voltage of 14.66 kV is applied to the needle electrode.....	48
Figure 25 - The variation of breakdown voltage as a function of absolute humidity (g/m ³) for electrode gap lengths of 2 cm, 5cm, 10 cm, 12 cm and 15 cm.	49
Figure 26 - The variation of breakdown voltage as a function of pressure (hPa) for electrode gap lengths of 2 cm, 5cm , 10 cm, 12 cm, and 15 cm.....	50
Figure 27 - The variation of breakdown voltage as a function of temperature (° C) for electrode gap lengths of 2 cm, 5cm , 10 cm, 12 cm and 15 cm.....	51
Figure 28 - The initiation and propagation of a cathode directed streamer for a gap length of 12 cm when a voltage of 58.74 kV was applied to the anode. Note that a single streamer occurred. (i) – The initiation of the streamer is seen. (ii) – The extension of streamer. (iii) – A further extension of the streamer from the anode. (iv) – The streamer has extended halfway across the gap. (v) – The primary streamer has progressed and completely crossed the gap. (vi) – Electrical breakdown of the gap has occurred as a bright light has been emitted. A branch from the streamer is seen.....	52
Figure 29 - Electrical breakdown of the 12 cm air gap is seen at point (a). A breakdown voltage of 58.74 kV was applied to anode.	53
Figure 30 - The propagation of the streamer for a gap length of 5 cm. (i) – The streamer has propagated from the anode towards the cathode. (ii) – The streamer has extended further towards the cathode. (iii) – Electrical breakdown of the air gap.....	54
Figure 31 - The propagation of the streamer for a gap length of 10 cm (i) – The initiation of the streamer is seen. (ii) – The extension of streamer from the anode. (iii) – The primary streamer has progressed and completely crossed the gap. (vi) – Electrical breakdown of the gap has occurred as a bright light has been emitted.....	54

Figure 32 - The initiation and the propagation of a streamer for a gap length of 15 cm. (i) – The extension of the streamer from the anode is seen. (ii) – A further extension of the streamer as well as branches is seen from the streamer. (iii) – The primary streamer has crossed the gap as well as multiple branches is seen. (iv) – An increase in the amount of light emitted by the streamer and the presence of a single branch near the cathode. (v) Electrical breakdown of the gap has occurred as a bright light has been emitted.....	55
Figure 33 - The initiation of a streamer from the anode when the atmospheric pressure was 994.0 hPa in the laboratory. A voltage of 77.50 kV is applied to the anode and the resulting branches is seen at the anode tip.	56
Figure 34 - An illustration of the branching that occurred at the anode tip for a pressure of 906.59 hPa in [96]......	57
Figure 35 - The bent path a streamer takes for a gap length of 15 cm when approaching the cathode.....	57
Figure 36 - The bent path a streamer takes when approaching the cathode for a 15 cm gap length. The location of an increased region of space charge is assumed in the frame.....	58
Figure 37 - An illustration of the bent path the HV arc took in the presence of a laser induced plasma in [98]......	58
Figure 38 - A FEMM model showing the electric field distribution in an air gap when there is a presence of excess space charge in the form of spheres. It is seen that the streamer takes a bent path when propagating towards the cathode.....	59
Figure 39 - The geometry of the streamer domain that was implemented in COMSOL Multiphysics.....	69
Figure 40 - The initial plasma cloud at t=0 s that was implemented in this dissertation for the initiation of the streamer. The Gaussian seed of electrons, positive ions and negative ions is located 0.001 cm from the high voltage electrode. (i) – The initial seed of electrons is seen. (ii) – The initial seed of positive ions is seen. (iii) – The initial seed of negative ions is seen.....	73
Figure 41 - The step voltage that has a magnitude of 3 kV which is applied to the anode.	75
Figure 42 - The mesh created on COMSOL Multiphysics which consists of triangular elements sized between 2 μm and 8 μm . (i) – The extremely fine mesh created throughout the entire domain. (ii) – A magnified portion of the domain showing the triangular elements.	78
Figure 43 - The 2D surface plots of the electron density for the initiation and the propagation of a streamer in a 1 mm air gap. (i) – t = 0.3 ns. (ii) – t = 0.6 ns. (iii) – t = 1 ns. (iv) – t = 1.5 ns. (v) – t = 2 ns. (vi) – t = 2.4 ns.	81
Figure 44 - A line graph showing the variation of the log of the electron density on the streamer axis for different time steps.	83
Figure 45 - The 2D surface plots of the electric field for the cathode directed streamer that propagates in a 1 mm air gap. (i) – t = 0.3 ns. (ii) – t = 0.6 ns. (iii) – t = 1 ns. (iv) – t = 1.5 ns. (v) – t = 2 ns. (vi) – t = 2.5 ns.....	84

Figure 46 - The variation of the electric field on the streamer axis for different time steps.	85
Figure 47 - The 2D surface plots of the electric potential for the cathode directed streamer that propagates in a 1 mm air gap. (i) – t = 0.3 ns. (ii) – t = 0.6 ns. (iii) – t = 1 ns. (iv) – t = 1.5 ns. (v) – t = 2 ns. (vi) – t = 2.5 ns.	86
Figure 48 - Plot indicating the magnitude of electric current at the anode tip at different times.	87
Figure 49 - The 2D surface plots of the electron mean energy (eV) profile for the streamer that propagates in a 1 mm air gap. (i) – t = 0.3 ns. (ii) – t = 0.6 ns. (iii) – t = 1 ns. (iv) – t = 1.5 ns. (v) – t = 2 ns. (vi) – t = 2.5 ns.	88
Figure 50 - Line graph showing the variation of the positive ion density on the symmetrical axis for different time steps.....	89
Figure 51 - Line graph showing the variation of the negative ion density on the symmetrical axis for different time steps.....	90
Figure 52 - Plot of the Townsend attachment coefficients as a function of the reduced electric field [61]. The water content values which were investigated in this comparison was 0%, 0.5%, 1% and 1.35% and these water composition values correspond to a relative humidity of 0%, 35%, 70% and 94.4% respectively. It should be noted that the y axis is on a log scale.	91
Figure 53 - The variation of breakdown voltage as a function of relative humidity (%) for an electrode gap length of 0.1 cm.....	92
Figure 54 - The variation of breakdown voltage as a function of pressure (atm) for an electrode gap length of 0.1 cm.	93
Figure 55 - The 2D surface plots of the electron density for a streamer modelled at different pressures in a 1 mm air gap . (i) – p = 1 atm. (ii) – p = 2 atm. (iii) – p = 3 atm.	93
Figure 56 - The circuit diagram of the high voltage direct current generator with ratings of the components that was used in the experimental procedure. The needle-plane air gap was the "load" for the experiment.....	113
Figure 57 - The MATLAB code created to correct the breakdown voltage to standard atmosphere conditions.	116
Figure 58 - The geometry of the 2 cm air gap that was implemented in COMSOL Multiphysics.....	122
Figure 59 - The 2D surface plots of the electron density which shows the initiation of the streamer at 1 ns.	122
Figure 60 - The 2D surface plot and line graph of the electron density. The numerical instabilities in these plots are seen.....	123

List of Tables

Table 1 - The electron impact reactions with the active species of Nitrogen used in this dissertation [66].	26
Table 2 - The electron impact reactions with the active species of Oxygen used in this dissertation [57].	27
Table 3 - The electron impact reactions with the active species of Water used in this dissertation [57].	27
Table 4 - The electron impact reactions used in the modelling of the streamer in air on COMSOL Multiphysics.	70
Table 5 - The three-body reaction used in the modelling of the streamer in air on COMSOL Multiphysics.	70
Table 6 - The reactions used in the modelling of the streamer in air on COMSOL Multiphysics.	71
Table 7 - The surface reactions used in the modelling of the streamer in air on COMSOL Multiphysics.	71
Table 8 - The settings used to create the ideally sized mesh that is used for the numerical modelling of a streamer.	77
Table 9 - List of parameters and variables used to model the cathode directed streamer for this dissertation.	80
Table 10 - The results obtained from the BOLSIG+ simulation. The reduced electric field was varied from 0-1000 Td and the values for the corresponding mean electron energy, electron mobility, diffusion coefficient, Townsend's ionization, and attachment coefficient is seen.	111
Table 11 - Table indicating the values the control unit was set to when a specific gap length was being investigated.	114
Table 12 - The atmospheric conditions and the breakdown voltage recorded for various air gaps on day one of the experiment. To improve accuracy, the experiment was conducted five times and the average breakdown voltage was used.	117
Table 13 - The atmospheric conditions and the corrected breakdown voltage recorded for various air gaps on day one of the experiment.	117
Table 14 - The atmospheric conditions and the breakdown voltage recorded for various air gaps on day two of the experiment. To improve accuracy, the experiment was conducted five times and the average breakdown voltage was used.	119
Table 15 - The atmospheric conditions and the corrected breakdown voltage recorded for various air gaps on day two of the experiment.	119
Table 16 - The atmospheric conditions and the breakdown voltage recorded for various air gaps on day three of the experiment. To improve accuracy, the experiment was conducted five times and the average breakdown voltage was used.	120

Table 17 - The atmospheric conditions and the corrected breakdown voltage recorded for various air gaps on day three of the experiment.	120
Table 18 - The atmospheric conditions and the breakdown voltage recorded for various air gaps on day four of the experiment. To improve accuracy, the experiment was conducted five times and the average breakdown voltage was used.	121
Table 19 - The atmospheric conditions and the corrected breakdown voltage recorded for various air gaps on day four of the experiment.....	121
Table 20 - The settings used to create a mesh that resulted in numerical instabilities.	123

Acronyms

AC	Alternating Current
DC	Direct Current
HVDC	High Voltage Direct Current
EEDF	Electron Energy Distribution Function
BE	Boltzmann Equation
FEMM	Finite Element Method Magnetics
FEM	Finite-Element Method
FCT	Flux-Corrected Transport
MUSCL	Monotonic Upwind-Centred Scheme for Conservation-Law
PDE's	Partial Differential Equations
PARDISO	Parallel Sparse Direct Solver
2D	Two-Dimensional
3D	Three-Dimensional
AMR	Adaptive Mesh Refinement
BDF	Backward Differentiation Formulas
RAM	Random Access Memory

1 Introduction

Atmospheric air is one of the most important gases that are used in an electrical power system as it is implemented to provide electrical insulation. It is utilized in various applications such as high voltage techniques and power distribution. Atmospheric air is also used to measure high voltages [1]. The insulator possesses several advantages with a few of these being economical, lightweight, and recyclable when compared to both solid and liquid insulators [2]. It is essential that the equipment used in a power system are reliable to ensure that there is a continuous transmission of energy from the power station to the consumer. Since atmospheric air is an important component in a power system, it is essential that the necessary research is performed on the insulation to ensure the reliability of the system [3].

It is important to understand the parameters that define the insulation capabilities of a dielectric as it determines the performance of it when used in practice. These parameters are the geometric arrangement of electrodes, the electric field strength, the composition of the gas, and the climatic conditions of it [1, 4]. Parameters such as the temperature, pressure as well as humidity vary within the atmosphere, and this subsequently influences the performance of the dielectric [1].

Due to there being an increase in the transmission of power in tropical countries [5], it is essential that research is conducted to investigate the effect high humidity has on the flashover characteristics of power lines and stations. Although humidity has a negligible effect on the breakdown voltage in a uniform air gap, it is important that the influence it has on the electrical discharge in an inhomogeneous field be studied as these fields are created in practice for a vast number of insulator configurations [1, 4, 5].

South Africa is a country that consists of climate zones where the northern parts of the country are in equatorial tropics whilst the southern parts of the country belong to subtropical regions [6]. KwaZulu-Natal is a province in South Africa that consists of a moderate climate, and it experiences months of high humidity and temperatures. The relative humidity experienced by the province throughout the year is in the range of 71% - 81% whilst the average daytime temperature throughout the year is in the range of 23 °C – 29 °C [7].

The application of a high voltage electric field to an air gap enables one to determine the dielectric strength of it in the conditions being investigated. Air breakdown most likely occurs because of transient streamers forming in the gap. This happens for a very short period which is in the range of microseconds and if the conditions are right, a conductive channel is created between the high voltage and grounded electrode [8]. Hence, the study performed in this dissertation is based on the streamer breakdown of air gaps and includes investigating the influence of atmospheric conditions, such as

humidity and pressure, on the breakdown voltage of an air gap. High-speed photography is also implemented in the investigation to capture streamers that were formed in the needle-plane air gap.

1.1 Research Question

The research questions that are investigated in this dissertation are:

Will the breakdown voltage of an inhomogeneous air gap be influenced by atmospheric pressure and humidity?

Does the presence of space charge in air influence the path of a streamer when propagating towards the cathode?

1.2 Hypothesis

The hypothesis is that an increase in humidity causes the breakdown voltage of atmospheric air gaps to increase in magnitude.

1.3 Importance of Study and Contribution

Investigations were done previously to determine the influence of humidity on the breakdown voltage of various air gaps. Schmid [1] investigated the impact of humidity on the breakdown voltage for a rod – plane air gap. The gap lengths that were investigated in this experiment were in the range of 20 cm to 100 cm and had either an impulse voltage or a DC voltage applied to the high voltage electrode.

An investigation performed by Wu et al. [4], studied the impact of humidity on the breakdown voltage of a rod – plane gap, sphere -plane gap and toroid – plane gaps. These electrodes were separated by a fixed distance of 60 cm with a switching – impulse waveform being applied to the high voltage electrode.

Kuffel [9] conducted an experiment to determine the effects of humidity on the breakdown voltage in uniform fields. The electrodes used to create these uniform fields were sphere gaps and plane electrode gaps which varied in gap distance from 0.5 cm to 25 cm. The voltage waveforms that were applied to these electrodes for this experiment were both AC and DC waveforms.

A study that was conducted by Rodriguez et al [10], investigated the impact of humidity on the breakdown voltage of different air gaps. These air gaps were created using different types of electrodes such as hemispherical rods, straight rods, or conical rods. The high voltage rods in this experiment had an AC voltage applied to it which had a frequency of either 30 kHz or 60 kHz. Research has been conducted in the past which investigated the effects of humidity on the breakdown

voltage for specific electrode arrangements, gap distances and voltage waveforms. The experiment and numerical simulation that was performed in this dissertation determined the effects of humidity and pressure on a needle – plane air gap. The gap lengths investigated were less than 15 cm which resulted in the streamer breakdown mechanism occurring for all these gap lengths. The electrical streamers that were created during the investigation were cathode directed streamers and was initiated by applying a DC voltage to the electrode. Research involving the influence of humidity on this specific electrode arrangement and gap lengths were not researched significantly in the past hence it was focused on in this dissertation.

1.4 Dissertation Structure

This dissertation consists of five chapters.

Chapter 2 consists of a literature review which introduces gases that are used as electrical insulators and contains a brief discussion of the two gases that are commonly used. The chapter also provides a description on the topic of plasma physics as well as the gaseous reactions that occurs in the 4th phase of matter. The mechanisms that result in a gaseous insulator breaking down as well as the factors that influence the breakdown voltage of an air gap are researched and presented in this chapter. As the dissertation consists of a numerical simulation that modelled the initiation of a cathode directed streamer and the propagation of it in an air gap, it is required that swarm parameters are obtained, and this is further elaborated on in this chapter.

Chapter 3 provides a description on the experimental setup that was implemented to investigate the streamer breakdown of air. It also consists of the results that were obtained in the experiment which were analysed in this chapter.

Chapter 4 consists of the numerical simulation that was implemented to model the initiation and propagation of an electrical streamer in an air gap. It contains the necessary steps that was performed to create the model as well as the results of the simulation which were analysed in this chapter.

Chapter 5 contains the conclusions and recommendations that was obtained from the investigation.

2 Literature Review

Gases are an essential component in an electrical power system as it is used to provide electrical insulation in a vast number of applications. Examples of these applications are gas insulated switchgears, gas-insulated transmission lines, or gas circuit breakers [11]. Several different gases are used as insulators and these are air, Oxygen (O₂), Hydrogen (H₂), Nitrogen (N₂), Carbon Dioxide (CO₂), Krypton (Kr), Argon (Ar) and electronegative gases such as Sulphur Hexafluoride (SF₆) [12, 13].

Any gas holds the advantage of having a low conductivity when being compared to either a solid or a liquid [11]. Gases are also excellent embedding and impregnation media as it possesses the ability to uniformly fill both closed cavities and accessible cavities through the diffusion process [14]. A comparison of the properties for each gas showed that Hydrogen has the advantage of having a better arc extinguishing property, however the gas has a lower dielectric strength when compared to air. It may also become an explosive mixture if it is contaminated with air. Nitrogen properties are similar to air as they both have the highest breakdown field strengths when compared to other natural gases. Carbon dioxide has a dielectric strength that is similar in magnitude to air. It also has an advantage of being a better arc extinguishing insulator when compared to air but only for currents that are of a moderate magnitude. Oxygen has the property of being an acceptable arc extinguishing insulator but has the downside of being a gas that is chemically active. SF₆ consists of an excellent arc-quenching property and is a gas that has an acceptable dielectric strength [12, 13].

2.1 Atmospheric Air

Atmospheric air is the most abundant dielectric material [15]. It has been used as a gaseous insulator for electrical equipment and provides insulation for both transmission and distribution lines since the commencement of the commercial supply of electric power [11, 15, 16]. It is a gas that is mainly composed of Nitrogen, Oxygen, Argon and Water (H₂O) [17].

An advantage of atmospheric air is that it is naturally occurring, “free” and does not require any form of special processing or treatment. The gas can be compressed by an exorbitant amount of pressure, at room temperature, which enables it to have a dielectric strength that is greater in magnitude when compared to other electronegative gases [12, 14]. Air also possesses the ability of immediately recovering its electric strength after the occurrence of a flashover or discharge due to the recombination of free charge carriers. There is also no change in its properties that could be brought about by aging [14]. There is interest that exists on the topic of gas-discharge plasma in atmospheric air as it could be used for the de-pollution of exhaust gases, potential ignition of combustible mixtures or aerodynamic flow control [18].

The breakdown field strength of air under standard conditions in a homogenous field is 30 kV/cm [13]. The breakdown voltage of air is less in uniform conditions when compared to SF₆, but the gaseous insulator consists of an exceptional insulating ability for non-uniform long gaps. These types of gaps are present in overhead lines [11]. It was observed by Takuma et al. [11], that the sparkover voltage of SF₆ was lower than atmospheric air when the electrode distance was increased.

The use of atmospheric air as an insulator can result in adverse effects such as oxidation or it may influence insulators negatively as rainfall or humidity causes the surface strength to decrease. Moisture from the atmosphere can be absorbed by solid insulating materials through the process of diffusion which will result in it building up at various interfaces. The electric strength of insulating oils is reduced in magnitude when moisture or gases are absorbed. Both Oxygen and moisture have the adverse effect of accelerating the aging process in oils. De-ionized water experiences an increase in conductivity if carbon dioxide is absorbed from the atmosphere [13].

2.2 Sulphur Hexafluoride

Sulphur Hexafluoride is a colourless, odourless gas that is non-poisonous, chemically inert and non-flammable [13]. It is used in several applications such as circuit breakers, enclosed switchgear, and in insulated cables as an insulation medium due to it possessing a higher breakdown strength (2.5 times greater than air). Sulphur Hexafluoride also has a better arc quenching characteristic when compared to other gases [13, 14, 19]. The magnitude of the electric strength increases by a factor of 10 above the strength of air when the pressure is increased by 3 to 5 bar. This allows high voltage switchgear to be designed smaller in size thus enabling it to be installed within cities or buildings at a reasonable cost [14].

A disadvantage that is associated with the use of Sulphur Hexafluoride is that poisonous by-products such as Hydrogen Sulphide (H₂S) can be created if it is exposed to high temperatures such as an arc [13, 14]. The use of SF₆ is associated with a higher cost, the gas is sensitive to non-uniform electric fields, and it has a greater liquifying temperature when the gas is operated at a higher pressure [19]. The gas also has a negative environmental impact as it contributes to the greenhouse effect [11]. Although the emission of the gas is less than CO₂, SF₆ is a gas that has the greatest global warming potential (23 900 times greater than CO₂). This resulted in the need of finding a replacement gas by the electric power industry, to perform the function of the gaseous dielectric with less harmful effects on the environment [11, 14].

2.3 The 4th State of Matter: Plasma

Plasma is a type of matter that consists of a partially ionized gas where the charge is electrically neutral in average, and this is referred to as “quasineutral”. Plasma is also a state of matter that exhibits collective properties. For example, the density is required to be of a sufficient magnitude. Plasma consists of neutral atoms or molecules, ions, and electrons. These particles interact with each other by collisions [20].

Plasma is defined by the following properties [21]:

1. Appearance of collective efforts. Examples of these are waves and instabilities.
2. The screening of long-range electric fields by individual particles.
3. The tendency towards charge neutrality.

Plasma is characterised by three fundamental parameters, and these are [22]:

1. The particle density (n) which is measured in particles per cubic meter.
2. The temperature (T) of each species which is measured in electron volts (eV).
3. The steady state magnetic field that is measured in Tesla.

The fractional ionization and cross-section of neutrals are vital for partially ionized plasma [22]. The two types of plasma that exist are non-collisional and collisional plasma. In a non-collisional plasma, the number of collisions that occur between the constituents of the plasma are so infrequent that its effect on the plasma dynamics is neglected. A collisional plasma consists of collisions that occur frequently, and this results in momentum exchange between the particle which causes it to dominate the plasma behaviour [23].

2.3.1 Collisional Plasma

Collisional plasma is further separated into two different classes, and these are partially ionized plasmas and fully ionized plasma. Partially or weakly ionized plasma consists of a large background of relatively neutral constituents whilst a fully ionized plasma consists of electrons and ions only. Dominant collisional processes in a weakly ionized plasma involve head on collisions between electrons and neutrals. Collisions that occur in a fully ionized plasma are between charged particles. The collisions in a fully ionized plasma are governed by the Coulomb interaction force [23].

2.3.2 Weakly Ionized Plasma

Neutral particles, that exist in a weakly ionized plasma, impede the motion of charged particles because they are heavy and compact obstacles. When either an electron or ion collides with a neutral atom, the particle loses a part or all its momentum and this is dependent on the angle at which it rebounds. The probability of the momentum loss experienced is expressed in terms of the equivalent molecular cross section of the neutral atom. The number of collisions per second which is also known

as the electron-neutral collision frequency is proportional to the number density of neutral particles, the average velocity, and the collisional cross section [23]. This is expressed in equation 1 as [23]:

$$\nu_{en} = N_n \sigma_n \langle v \rangle \quad (1)$$

Where:

ν_{en} : Electron-neutral collision frequency

σ_n : Equivalent molecular cross section

N_n : Number density of neutral particles

v : Average velocity

Neutral species are depleted in the gas phase of plasma by dissociation, ionization, dissociative attachment, and excitation processes [24]. The processes that are investigated and used in this dissertation are attachment, elastic, ionization, and excitation processes.

2.4 Gaseous Reactions

An electric field is created when a potential difference is applied across a gap. Therefore, free electrons in a gaseous gap are accelerated when an electric field is applied. These accelerated electrons collide with either gas atoms or molecules that are present in the gap [25].

2.4.1 Collisions

A collision refers to an isolated event that occurs when two or more moving bodies exert forces on each other for a relative short period of time [26].

2.4.2 Elastic Collisions

An elastic collision is a collision where an electron and a molecule collide with each other. All the energy involved in this collision is maintained as kinetic energy which is conserved. This collision is a two-body (binary) collision where the electron is travelling at a speed much greater than the molecule. Therefore, the molecule is considered to be at rest. The electron is then set off on a new trajectory when the collision takes place. This is a dominant type of collision, and it has the possibility to occur for any kinetic energy of the incident electron [25].

Elastic collisions are represented by equation 2 below [25]:



Where:

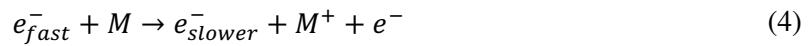
e^- : Electron

M : Neutral molecule or atom

An elastic collision between two particles results in the momentum being redistributed between these particles [27].

2.4.3 Inelastic Collisions

An inelastic collision results in the momentum being redistributed between particles, but only a fraction of the initial kinetic energy is transferred to the internal energy of one or more of the particles. The transfer of internal energy may cause particles to experience an excited state which has a lifetime greater than the relaxation time of the molecular gas. When an inelastic collision occurs, the reaction may result in the molecule being left in a rotational, vibrational, or in an electronically excited state [27, 28]. Both equations 3 and 4 represent an inelastic collision which can either result in an excited particle or the creation of a positively charged particle respectively [27]:



Where:

M^* : Excited molecule or atom

M^+ : Positively charged molecule or atom

2.4.4 Ionization Reactions

Ionization is a fundamental process in plasma as it is responsible for plasma generation which is the birth of new electrons and positive ions [26]. The process of ionization by collision occurs when a free electron collides with a neutral gas molecule [29]. This results in an electron being liberated from a gas molecule and causes the production of a positive ion.

If one must consider a low-pressure gas column which has an electric field applied across two plane parallel electrodes, an electron which is present at the anode is accelerated. This electron collides continuously with other gas molecules when travelling towards the cathode. If the energy gained by the electron due to these collisions exceeds the ionization potential, then ionization takes place. The ionization potential is defined as the energy required to dislodge an electron from its atomic shell [29]. This process results in the primary incident electron removing an electron from the atom or molecule therefore producing a positive atomic or molecular ion and two electrons [26].

An ionization by collision reaction is represented symbolically in equation 5 as [25, 26]:



Where:

ε : Energy gained by the electron

V_i : Ionization potential energy

2.4.5 Photoionization

Photoionization is a type of ionization that is caused by the interaction of radiation or photons with matter. It is a process that occurs when the radiation energy absorbed by the atom or molecule exceeds the ionization energy of that particle [12].

The processes in which radiation can be absorbed by atoms or molecules are [29]:

1. The excitation of a particle to a higher energy state.
2. The continuous absorption by either direct excitation of an atom, the dissociation of a diatomic molecule or direct ionization, etc.

This process is represented symbolically in equation 6 as [12]:



Where:

$h\nu$: Photon energy

It is a secondary ionization process that is required in the streamer breakdown mechanism [12].

2.4.6 Background Ionization

Background ionization is another viable source that provides free electrons to the front of a positive streamer. This is an ionization process that is present in a gas before a streamer commences and is a process that is not produced by the streamer [30]. The process can occur from multiple sources. For example, ambient air consists of radioactive compounds that can either originate from cosmic rays or building materials. These sources lead to a natural ionization level of 10^9 - 10^{10} m^{-3} at ground level. Background ionization also occurs from leftover ionization that has been produced from previous discharges. It is also created from external UV-radiation sources, X-ray sources, the addition of radioactive compounds to the gas and either electron or ion beam injection [30].

2.4.7 Excitation Reactions

An electron is found in the orbit of the lowest energy state when the atom or molecule is in its “normal” state. If the electron is moved to higher energy state, then it is referred to as being in an excited state [16]. A neutral atom or molecule is raised to an excited state if ionization does not take place when a collision between a neutral particle and an electron occurs. This happens as the kinetic energy of the electron is transferred to the neutral molecule [31].

An excitation reaction is represented by equation 7 as [31]:



2.4.8 Electron Attachment Reactions

A negative ion is produced when an electron becomes attached to a neutral molecule or atom. These ions are essential in the breakdown process of gases such as O₂, N₂, SF₆ and air [26]. The presence of these reactions in a minute capacity impacts the behaviour of the ionized gas drastically [32].

An electron attachment collision is represented by equation 8 below [25]:

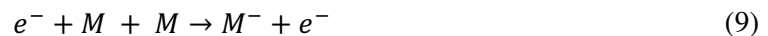


Where:

M^{-} : Negatively charged molecule or atom

2.4.9 Three Body Collisions

A three-body collision occurs when a third body is present in the collision. This third body allows for the recombination process to simultaneously satisfy the conservation requirements for both energy and momentum. The probability of a gas atom taking part in a three-body collision is directly proportional to the pressure of the system [26]. An example of a three-body collision is seen below in equation 9 [25]:



2.4.10 Electric Field

If a single charge is present in an empty space, it causes the space to experience a change. The introduction of a second charge in this same place results in it experiencing a force at every point of that space. The electric field is a concept that describes all possible effects of such forces at various locations in space after a charge has been placed at a particular point [33].

The electric field strength is defined as the force in the field per unit charge and it is a vector quantity [33]. Equation 10 below is used to determine the electric field strength [33].

$$E = \frac{F}{Q} \quad (10)$$

Where:

E : Electric field strength (V/m)

F : Force (N)

Q : Charge (C)

2.4.11 Electron Mobility

The presence of an external force on a system such as an electric field causes both electrons and ions to experience drift even if the plasma is homogenous. Electrons move at random when considered individually because of their finite temperature but when averaged, these electrons drift in the direction that is opposite to the electric field. The electrons drift with a velocity that varies directly with the field and inversely to the density of the gas. Mobility is the parameter that is used to describe the drift of particles in a plasma when it is influenced by an external electric field. It is obtained using equation 11 [23, 34]:

$$\mu = \frac{|v_d|}{E} \quad (11)$$

Where:

μ : Mobility (m²/ V sec)

v_d : Drift velocity

Due to electrons having a mass as well as carrying a charge, the drift of it corresponds to the transport of mass and the electric current [23].

2.4.12 Diffusion

In an electrical discharge, both electrons and ions migrate from a region of higher concentration to a region of lower concentration provided there is a non-uniform concentration of charges. This process is referred to as diffusion and results in a de-ionizing effect at regions of low concentration. Walls that are present in the system, which confine a given volume, increases the de-ionization effect as charged particles experience a loss of charge when colliding with the wall. Mass motion is a result of both mobility and diffusion in a system and is described by the drift velocity. This can either be caused by an unbalanced collision force or the electric field itself [29].

The rate at which diffusion occurs is controlled by the diffusion passing through unit area in unit time perpendicular to the unit concentration gradient [29]. The diffusion coefficient for both electrons and ion species are linked with mobility. It is referred to as the Einstein's relation and is represented by equation 12 below [35]:

$$D = \frac{\mu k_B T}{Q} \quad (12)$$

Where:

D : Diffusion coefficient

k_B : Boltzmann's Constant

T : Species temperature

2.4.13 Electron Temperature

The average energy of electrons present in a plasma is linked to their temperature. Equation 13 represents this relation [26]:

$$w_{av} = \frac{3}{2} k_B T_e \quad (13)$$

Where:

w_{av} : Average energy of the electron

T_e : Electron temperature

The electron temperature is greater than the temperature of the gas at lower pressures. As the pressure of the plasma increases, the rate at which energy transfers from the electron to the neutrals increase thus resulting in the temperature of the gas to increase and this consequently reduces the electron temperature [26].

2.5 Breakdown Mechanisms in Gases

A highly conductive channel is required to be formed between two electrodes so that the electrical breakdown of a gas occurs. The breakdown is a result of ionization processes commencing and it causes the generation of many charge carriers in the gas. Both uniform or weakly non-uniform fields require an avalanche process that is above or below the critical amplification for breakdown to occur. This is dependent on conditions such as the electrode shape or the gap distance between the electrodes. The avalanche process described above is the basis for both the Townsend and Streamer mechanism [36].

A discharge process commences when there are charge carriers present in the gas which are influenced by the electric field. These charge carriers are also generated externally by a light flash that has a short wavelength or by cosmic irradiation on the electrode surface. However, this process produces a very small number of charge carriers which is not sufficient for electrical breakdown to occur [36].

The application of a voltage to an electrode system creates a field in an air gap. This results in electrons being created in the gap. These electrons can either originate from the ionization of neutral molecules or atoms, photon irradiation from cosmic rays, or by the ultraviolet illumination of the cathode. If the applied voltage increases in magnitude, electrons are then generated by photons from the avalanche itself. After this process occurs, the electrons accelerate in the direction of the anode whilst gaining kinetic energy due to its movement. Two processes can either occur when the kinetic energy has increased to a sufficient magnitude. The first is an inelastic collision where the electrons

collide with neutral molecules resulting in them being ionized and the second being a collision where the neutral molecule reaches a higher excited state or a vibrational state [36].

As stated previously in section 2.4.4, ionization results in the ejection of a secondary electron from a neutral molecule or atom and leaves a positive ion behind. This secondary electron along with the primary electron continues the process of ionization. Molecules do not play a role in ionization as they are much heavier in comparison to electrons and thus are considered to be stationary. The electric field that is applied accelerates the electrons. This releases more electrons by colliding with gas molecules present on its path. This process occurs systematically causing an electron avalanche. Figure 1 depicts the avalanche of electrons reaching the anode [36].

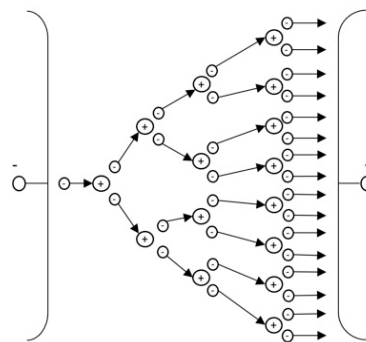


Figure 1 - The development of an electron avalanche that occurs from one free electron when there is an electric field applied [36].

2.5.1 Townsend Mechanism

Referring to Figure 2 below, a parallel plate capacitor is depicted, and the plates of this capacitor are separated by a distance d which is filled with a gas. The absence of an electric field between the plates ensures that there is a state of equilibrium between the state of electron and positive ion generation due to the decay process [12].

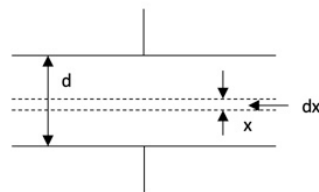


Figure 2 - A parallel plate capacitor that has a gaseous insulating medium and is separated by a distance d [12].

The application of an electrical field results in the state of equilibrium being disturbed. Townsend investigated the variation of current as a function of voltage. His results indicated that the current increased proportionally with an increase in voltage and then the current remained constant at I_0 . This is referred to as the saturation current. Figure 3 shows the variation of current as a function of the applied voltage to the parallel plate capacitor [12].

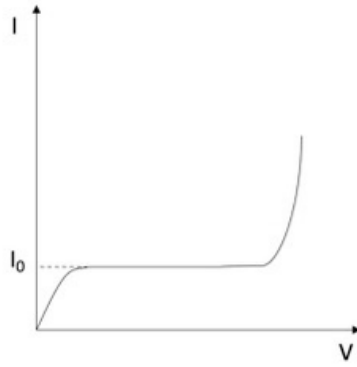


Figure 3 - The change in current that results from an increase in voltage [12].

If a voltage that is greater in magnitude is applied, then the current increases exponentially. This is due to the ionization of gas caused by electron collision as seen in Figure 3. An increase in voltage causes an increase in V/d which subsequently results in electrons being accelerated. As the electrons continuously accelerate and collide, it acquires a higher kinetic energy which results in the knocking out of more electrons [12].

Townsend's first ionization coefficient was introduced by himself to explain the exponential rise in current. It is defined, "as the number of electrons produced by an electron per unit length of path in the direction of field" [12, p. 3]. Equation 14 is used to express the number of electrons that have travelled a distance d [12]:

$$n = n_0 e^{\alpha d} \quad (14)$$

Where:

n_c : The number of electrons that are released from the cathode by ultraviolet radiation.

n_0 : The number of electrons reaching the anode.

The term $e^{\alpha d}$ is referred to as the electron avalanche. It indicates the number of electrons that are produced by one electron when travelling from the cathode to the anode [12].

The exponential increase in current is expressed in equation 15 [12]:

$$I = I_0 e^{\alpha d} \quad (15)$$

2.5.2 Secondary Effects

The cathode is a vital component of a gas discharge as it supplies the required electrons for initiation, sustenance, and the completion of the discharge. Under normal conditions, the electron in a metal is not allowed to leave the surface as it is tied down by the electrostatic force that exists between the electrons and the ions in the lattice [12].

Secondary emission occurs when electrons are emitted by the bombardment of positive ions on the cathode surface. This occurs when the positive ion has more than twice the energy of the work function of the metal as one electron neutralizes the bombarding positive ion, and the other electron is released [12]. As investigated by Hallac et al. [37], it was observed in the numerical simulation performed that the secondary emission process is a mechanism of great importance as it provides secondary electrons for very small gaps and even has the capability to replace photoionization.

2.5.3 Townsends Second Ionization Coefficient

Taking log on both sides of equation 15 results in equation 16 [12]:

$$\ln I = \ln I_0 + \alpha x \quad (16)$$

Results in equation 16 and this represents a straight-line equation with a slope of α and intercept of $\ln(I_0)$ for a given pressure whilst E is kept constant. This is seen in Figure 4.

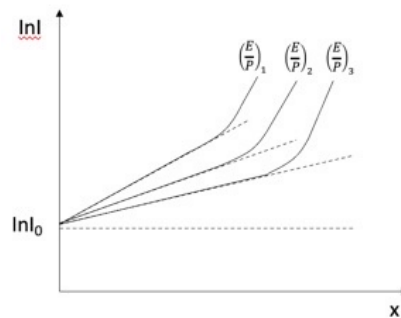


Figure 4 - The change in the gap current with gap length in a uniform E [12].

According to Townsend, the current in a parallel plate gap increased more rapidly with an increase in voltage when compared to equation 15. It was suggested that a second mechanism is affecting the current and theorized that the additional current is a result of the presence of positive ions and photons. These positive ions liberate electrons by both collisions with the gas molecules present and the bombardment of it against the cathode. Photons also release electrons after collision with the gas molecules and also from photon impact with the cathode [12].

The Townsend second ionization coefficient is defined as “*number of electrons released from cathode per incident positive ion*” [12, p. 5]. The current in terms of the second ionization coefficient is expressed in equation 17 as [12]:

$$I = \frac{I_0 e^{\alpha d}}{1 - \nu(e^{\alpha d} - 1)} \quad (17)$$

ν : Townsend second ionization coefficient

It should be noted that there is a possibility of more than one mechanism producing secondary ionization in the gap hence ν is a single coefficient used to represent the sum of these mechanisms.

ν is also dependent on the work function of the material and it only influences breakdown mechanisms in low-pressure systems [12]. An illustration of the Townsend breakdown mechanism is seen in Figure 5.

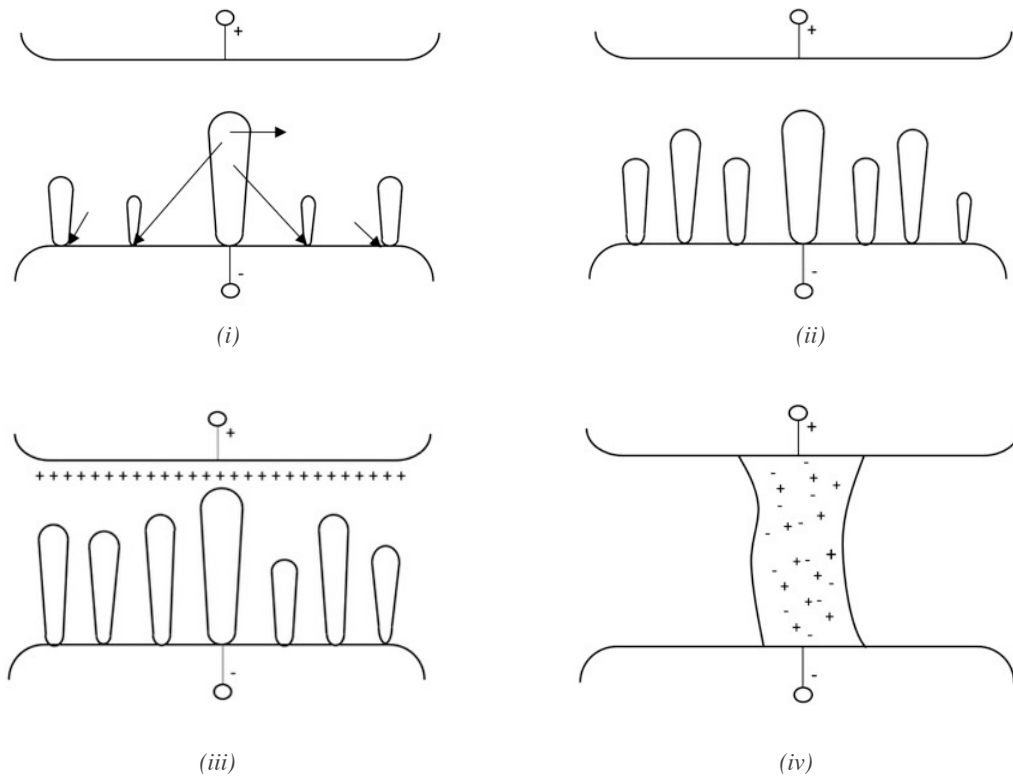


Figure 5 - An illustration of the Townsend breakdown mechanism. (i) – The ejection of the electron from the cathode is seen. (ii) – Multiple avalanches are generated. (iii) – After 4 generations there is a build-up of positive space charge by the anode. (iv) – An electrical breakdown by constriction take places because of this [36].

2.5.4 Streamer Mechanism

The Townsend mechanism develops from the production of a series of successive avalanches. A high voltage that is applied to a uniform field gap results in very short time lags of spark breakdown which is not consistent with the Townsend mechanism. The Townsend generation mechanism states that the drift velocity of the electrons influences the time that is required for breakdown to occur by normal avalanche propagation in a few generations. According to experimental results, the time required for breakdown was shorter in comparison to the estimated time that was obtained theoretically [36]. The Townsend mechanism would also have difficulty elaborating on how sparks branch and have an irregular growth when the gaps are sufficiently longer in size [32].

The streamer theory of the spark was developed by Loeb and Meek for positive streamers. Raether developed the streamer theory of the spark for negative streamers [32]. A streamer is a type of ionization wave that propagates due to the separation of both positive and negative charges with the enhancement of the electric field at the wavefront [38]. Both positive and negative streamer theories

indicate that the spark discharge develops directly from a single avalanche which then transforms into a plasma streamer because of the space charge present. This results in the conductivity growing rapidly and allows for breakdown to occur through the channel. The following features are essential for both positive and negative streamers [32]:

1. The photoionization of gas molecules that happens in the space ahead of the streamer.
2. A local enhancement of the electric field resulting from the space charge at the tip of the streamer.

A distortion of the field occurs in the gap due to the space charge being present in it [32]. This is seen in the Figure 6 below.

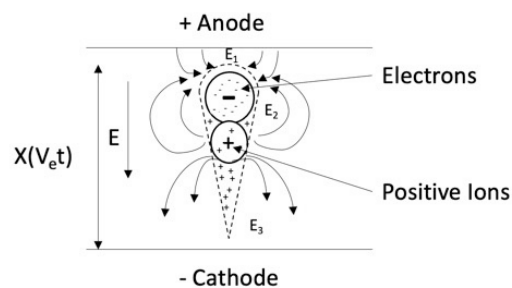


Figure 6 - The distribution of charge carriers in an avalanche and its contribution to the applied uniform electric field. It should be noted that $E_1 > E$, $E_2 < E$ and $E_3 > E$ [32].

According to Raether, the growth of the avalanche is weakened when the charge concentration is greater than 10^6 but is less than 10^8 ($\frac{dn}{dx} < e^{\alpha d}$). The avalanche experiences a steep increase in current and breakdown of the gap occurs when the concentration exceeds 10^8 . This change is dependent on the concentration of carriers for both situations and is attributed to the change in the electric field because of the space charge field [12].

2.5.5 Positive (Cathode Directed) Streamers

Streamers that appear in nature can either be positive or negative in polarity. Positive streamers propagate in the direction of the cathode whilst negative streamers move towards the anode [39]. Both positive and negative streamers are implemented in several applications of plasma technology. Examples of these applications are surface processing, ignition, combustion, flow control, environmental applications, catalysis, sterilization, disinfection and even the production of free radicals. Streamers are also used for wound cleaning in the medical industry but in the form of atmospheric pressure plasma jets [40].

A positive streamer has an excess of positive charge at its head and propagates against the direction of the electron drift with a velocity that is similar in magnitude. Positive streamer coronas are used in industrial applications to produce ozone gas and perform the function of gas cleaning. It is a type of streamer that requires an electron source ahead of the ionization front [41].

Research has been focused on positive streamers as it is easier to create around sharp tips when compared to the alternative [39, 42]. The growth of a positive streamer only occurs where the electric field is high enough to ensure the multiplication of approaching ionization avalanches. The charge layers in a positive streamer are created by excess positive ions that barely move. This results in a stable field enhancement ahead of the positive streamer [41].

The initiation of a streamer from a pointed electrode happens at a lower voltage for a positive streamer when compared to a negative streamer [42]. The velocity of a positive streamer is dependent on the head radius whilst the velocity of the negative streamer is dominated by the enhanced electric field [42]. The experimental results obtained by Luque et al. [42], showed that positive streamers are much faster in speed, longer in length and thinner in appearance. Positive streamers were investigated in this dissertation.

2.5.6 The Positive Streamer Breakdown Mechanism

The streamer breakdown mechanism of a cathode directed streamer in a uniform field is described by Meek and Loeb [36]. This process is as follows.

As the avalanche extends across a gap, it causes the electrons to be swept into the anode. The positive ions that are located at the tail of the avalanche stretches out across the gap [36]. This is seen in Figure 7 below.

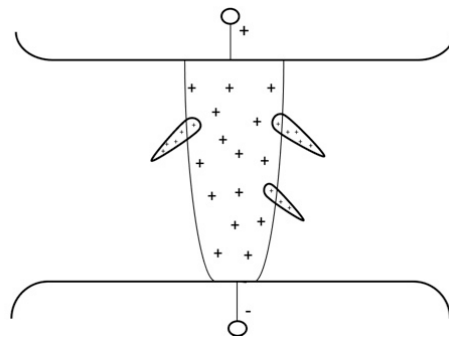


Figure 7 - Primary electrons from the avalanche that are being swept into the anode [36].

The positive ions result in a highly localized space charge field being produced near the anode. The ion density elsewhere is of a low magnitude and because of this a breakdown in the gap does not occur. Secondary electrons are also produced from the gas that surrounds the avalanches because of photons and the photoelectric effect that occurs at the cathode. These secondary electrons then initiate secondary avalanches that are directed toward the stem of the main avalanche. Secondary electrons are also produced by the field enhancement, but this occurs when the space charge field developed by the main avalanche is in the same order of the applied field intensity. The secondary avalanche is then fed into the primary avalanche, and this is seen in both Figure 7 and Figure 8.

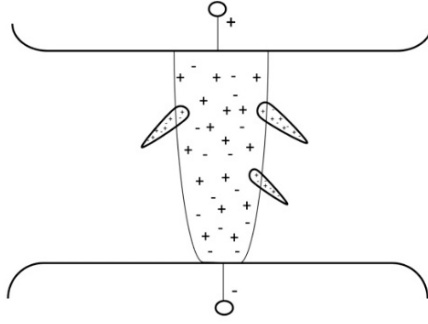


Figure 8 - Secondary avalanche being fed into the primary avalanche [36].

The secondary avalanche results in positive ions being left behind. This performs the function of effectively lengthening and intensifying the space charge of the main avalanche. This occurs in the direction of the cathode and this process develops further into the form of a self-propagating streamer which results in electrical breakdown. This process is seen by referring to Figure 9.

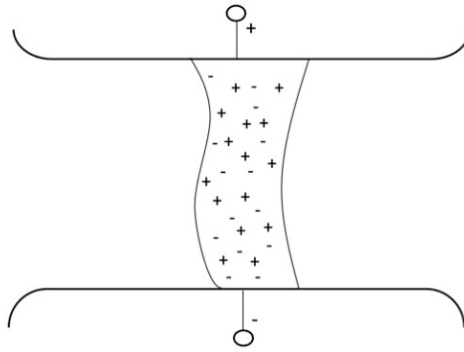


Figure 9 - A self-propagating streamer that causes electrical breakdown [36]

An electron avalanche transitions into a streamer when the radial field that is produced by the positive ions at the head of the avalanche is of the same order as the externally applied field [32]. This is represented using equation 18 [32]:

$$E_r = \kappa E \tag{18}$$

Where:

E_r : Radial field

$$\kappa \approx 1$$

Equation 19 is used to express the criterion of breakdown that was developed by Loeb and Meek [32].

$$E_r = \frac{5.27 \times 10^{-7} \alpha e^{(\alpha x)}}{\left(\frac{13500 x}{p}\right)^{\frac{1}{2}}} \tag{19}$$

Where:

α is represented in m^{-1}

p : Gas pressure (Pa)

The breakdown voltage is the magnitude at which the avalanches grow so that their radial field is equivalent to the externally applied field [32].

2.5.7 Streamer Inception

A streamer occurs at the initial stage of a gas discharge in a long air gap. When a positive DC voltage is applied to a pair of electrodes, the streamer occurs at the point where the ionization coefficient is equal to the attachment coefficient near the electrodes. As the avalanche develops, so does the number of electrons in the head increase until streamer inception [43]. For a streamer to originate, the charge at the head of the electron avalanche is required to satisfy equation 20 [44]:

$$\exp \int_0^l (\alpha - \eta) dz \geq N_{crit} \quad (20)$$

Where:

α : Ionization coefficient

η : Attachment coefficient

l : The length of the critical electron avalanche

N_{crit} : The critical charge number required for streamer formation

Both α and η in equation 20 are required to be functions of the reduced electric field (E/N). A second streamer criterion that must be satisfied; is that the number of electrons present in the secondary avalanche must equal the number of electrons that were present in the first avalanche [43, 44].

2.5.8 Electrode Configuration for Streamer Initiation

An investigation that was performed by Luque et al. [42] on both positive and negative streamers in ambient air implemented a needle-plane geometry. This was done as the use of a needle-plane electrode configuration resulted in streamers emerging from the pointed electrode. It should be noted that needle-plane electrode configurations are used in laboratory experiments and engineering applications as it creates an inhomogeneous field.

A computational analysis performed by Abd Alameer et al. [45], consisted of a model being developed with a rod-plane electrode geometry so that the electrical breakdown of air could be investigated. The model consisted of various rod electrodes that were of different sizes which were connected to the high voltage whilst the plane electrode was grounded. This type of electrode

arrangement results in a non-uniform electric field being created. It was concluded in the investigation that the breakdown voltage of the gap increased when the diameter of the rod increased. This is attributed to the diameter of the hemisphere which subsequently decreases the electric field magnitude causing a greater voltage to initiate breakdown. Hence an electrode with a thinner diameter was preferred for the experiment conducted in this dissertation as it reduced the magnitude of voltage required for breakdown.

Allen and Mikropoulos [46], performed an investigation on the propagation of streamers in air by implementing two plane electrodes that were parallel to each other. This electrode arrangement consisted of streamers being initiated at a sharp point in an earthed anode plane. An electrode arrangement of this type has the advantage of allowing basic properties to be studied and enabled the author to control the amount of energy required to initiate the streamer. This also allowed for the investigation of a wide range of conditions such as the propagation threshold and streamer-induced breakdowns.

2.5.9 The Different Types of Streamer Breakdown

As indicated by Seeger et al. [18], the two processes that are involved in streamer breakdown are the crossing of the gap by the streamer and the heating of the streamer channel. An increase in the electrical conductivity is caused by the heating of the channel and this leads to electrical breakdown. Streamers are classified according to the different mechanisms of channel heating and the 3 types that exist are the arrested streamer mechanism, the stem mechanism, and the secondary streamer mechanism.

2.5.9.1 Arrested Streamer Mechanism

This is a mechanism that is common in strongly electronegative gases and in air where there is a great distance between the electrodes. It is also a mechanism that is dominant where breakdown voltages are of a low magnitude and where lightning impulse waves are applied to the high voltage electrode. When a streamer discharge occurs at the tip of an arrested streamer, it causes the heating of the channel, and this is done by the streamer corona current [18]. This is seen in frame (i) in Figure 10.

2.5.9.2 Stem Mechanism

This mechanism involves the current of several streamers being fed into one common stem as seen in frame (ii) in Figure 10. As observed in [18], the mechanism results in a slow discharge that has a longer formative time lag hence it is vital for voltage applications that are long in duration. It is a mechanism that only occurs for AC and DC waveforms. New discharges may be formed at the tip of the stem as streamer corona can be initialised at that point (arrested streamer mechanism) [18].

2.5.9.3 The Secondary Streamer Mechanism

This mechanism involves the discharge activity of the secondary streamer occurring within the streamer channel and it is also dominant at higher voltages [18]. When this mechanism happens, an electron injection takes place at the cathode into the residual channel. These injected electrons then redistribute the potential in the channel, and this causes the strength of the electric field at the anode tip to be high again thus resulting in a secondary streamer channel being created [47]. The propagation of the secondary streamer is seen in frame (iii) in Figure 10.

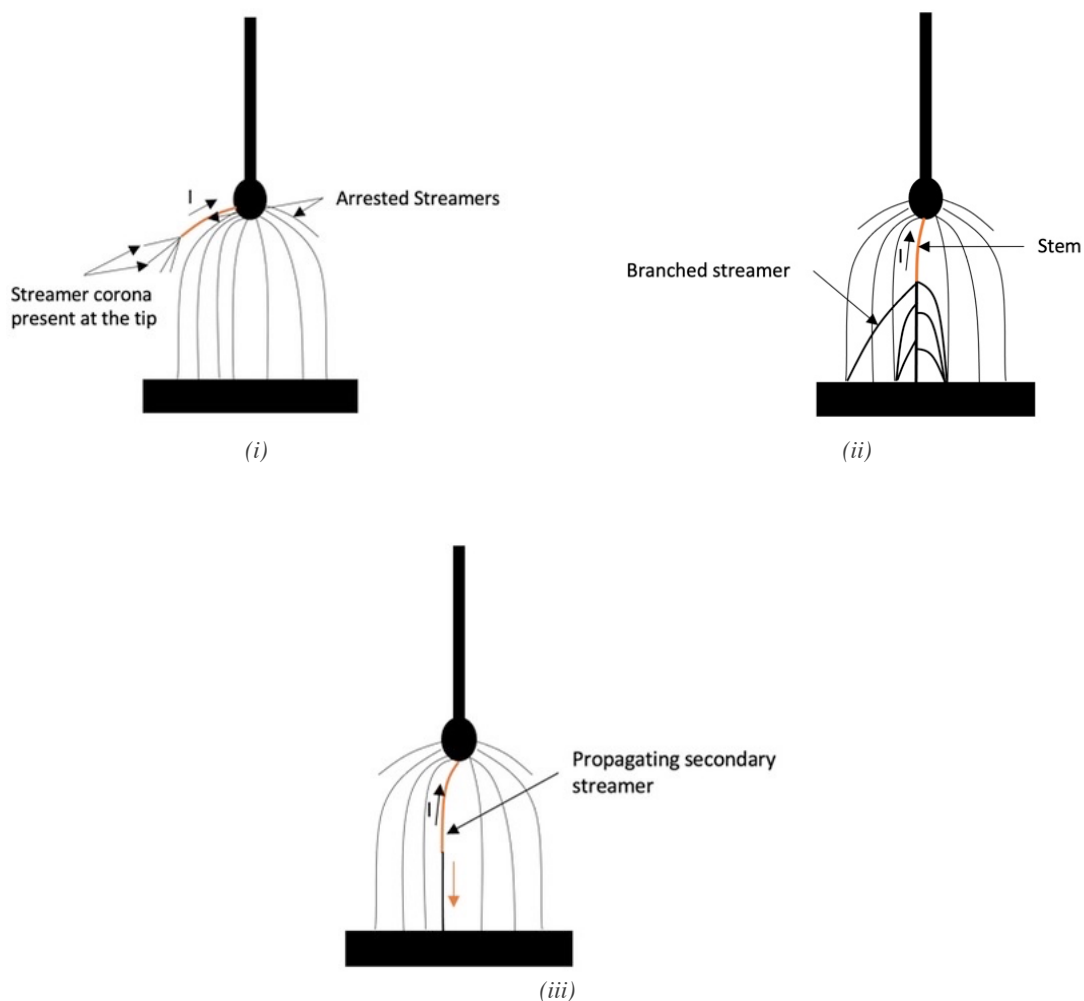


Figure 10 - An illustration of the various streamer breakdown mechanisms that occurs in an air gap [18]. (i) – Arrested streamer mechanism. (ii) – The stem mechanism. (iii) – The secondary streamer mechanism.

2.5.10 The Influence of Atmospheric Conditions on the Breakdown Voltage

2.5.10.1 Humidity

Studies that were conducted by Radmilovic 'Radjenovic ' et al. [48] and Kuffel [9], showed that there was an increase in breakdown voltage when the humidity increased. This is a result of water vapor and air combining. This process increases the breakdown voltage because water vapor has a higher breakdown strength in comparison to air. There is also a reduction in the length of electron avalanches at the area in front of the streamer head. This is a result of the UV radiation being absorbed at a greater rate as there is an increased amount of water molecules present in the atmosphere. This results in a greater electric field being required to facilitate the propagation of the streamer. Therefore, a greater breakdown voltage is required as the humidity increases [1].

As indicated Paul Abraham and Prabhakar [49], there is also a substantial increase in the attachment coefficient in humid air whilst there is no significant increase in the ionization coefficient. Water has the ability recombine at a faster rate after dissociation has occurred. This results in the breakdown strength increasing as it is less likely that there are free ions present to support the creation and continuation of an avalanche [48].

2.5.10.2 Pressure

Investigations performed by Kamarudin et al [50] as well as Govinda Raju and Hackam [51] showed that the breakdown voltage of air is directly proportional to the atmospheric pressure. The mean free path between molecules plays a fundamental role in the breakdown of a gas and it is a function of pressure as seen in equation 21 [52]:

$$\lambda \propto \frac{1}{p} \quad (21)$$

Where:

λ : Mean free path between molecules

p : Pressure the molecules are subjected to

As seen in equation 21, an increase in the pressure results in the reduction of the mean free path between molecules. This results in the molecules not being able to obtain enough energy which prevents ionization and the initiation of the breakdown process [52]. Therefore, the breakdown voltage increases as the pressure increases in an air gap.

2.5.10.3 Temperature

Investigations that were performed by Uhm et al. [53] and Dandaron et al. [54], concluded that the breakdown voltage of an air gap is inversely proportional to the temperature of the gas.

2.5.11 Electrode Influences on the Breakdown Voltage

2.5.11.1 Electrode Geometry

As indicated by Ratnaker and Kamath [55], the breakdown voltage of a gap is dependent on the type of electrodes used. Electrodes may have tips that are either flat ended, pointed, curved or plane tips. The type of tips that are used causes a variation in the breakdown voltage of the gap. These breakdown voltages are influenced by the electric field that is created by the electrode pairings. As seen in the investigation conducted by Ratnaker and Kamath [55], the electrode geometry effects are negligible in small gap lengths but as the gap length increases, the geometry of the electrodes begins to influence the breakdown voltage. In instances where the electric field is widely distributed over the surface area of the electrodes (sphere-plane electrodes), it resulted in a higher voltage being required for the breakdown of the air gap. It was also observed in [55], that the electrode pairings which result in the electric field being concentrated towards the tip of the electrode (pointed-plane combination) required a lower voltage to cause the electrical breakdown of an air gap. A smaller surface area results in the electric field strength at the electrode tip being of a greater magnitude (needle-plane electrodes) [56].

2.5.11.2 Electrode Distance

According to Abdel-kader et al. [57], the voltage required to initiate breakdown between positive and negative electrodes increases as the distance between them increases.

2.5.11.3 Electrode Roughness

An electrode's surface roughness influences the breakdown strength of a gas by reducing it significantly. Surface roughness of an electrode results in the existence of localized microscopic regions with local held intensities that are larger than the average field in the gas near the electrodes. These regions that exist with an enhanced field intensity causes a reduction in the breakdown voltage, but this is also dependent on the gas pressure [58].

2.5.11.4 Electrode Surface Area

According to Shioiri et al. [59], investigations performed in a vacuum confirmed that the breakdown voltage of a gap is inversely proportional to the electrode surface area.

2.5.11.5 Electrode Material

A vital factor that influences the breakdown voltage of an insulating gas is the work function of the electrode material. The work function is defined as the minimum amount of energy that is required to remove an electron from a solid to a point immediately outside the solids surface. The magnitude of the work function is approximately half of the ionization energy of a free atom of the metal [60].

As investigated by Sharifpanah et al. [60], the breakdown voltage of an electrode material is directly proportional to that element's ionization level. This indicates that more energy is required for an

electron to depart the surface of a metal and move to a point outside the solid surface when being compared to elements that have a lower energy level. It should be noted that factors such as the materials thermal conduction, melting point, and the mechanical strength of the material also influence the breakdown voltage.

2.6 Swarm Parameters Implemented for the Numerical Simulation of a Positive Streamer

Swarm parameters is a term that is used to refer to quantities such as the electron drift velocity, diffusion coefficient, mobility, electron attachment coefficient, electron detachment coefficient, recombination coefficient, the mean energy, and Townsends first ionization coefficient. These quantities depend upon the ratio of the electric field to the gas pressure. Investigations that consist of discharges in simple conditions and common gases have their electron transport and rate coefficients measured and tabulated as functions of the reduced electric field. The reduced electric field is defined as the ratio of electric field strength to the gas particle number density [61, 62, 63].

Transport or rate coefficients that include electrons depend on the Electron Energy Distribution Function (EEDF). The EEDF as well as the coefficients required for a discharge is obtained by using collisional cross-section data and solving the Boltzmann Equation. This is performed by solving some approximation of the Boltzmann Equation for a series of reduced electric field values and placing the resulting coefficient in tables against their respective reduced field values or mean electron energy values. This data is then used in the fluid model to determine the transport and rate coefficients by interpolation [61].

2.6.1 Collisional Cross Sections

The cross section is used to indicate the probability of a collisional interaction occurring and is measured in unit area [28].

Considering two particles that have a radius r , which move towards each other and makes contact at the instant of the collision. If it is assumed that the particles are like two hard billiard balls that have equal radii, then the cross section is defined as the area that encompasses both particles. For the two particles that have a radius r mentioned, the cross section is obtained using equation 22 below [64]:

$$Q = 4\pi r^2 \quad (22)$$

Where:

Q : Collisional cross section

r : Radius of particle

Modelling plasma requires the use of scattering cross section data as it dictates the relative velocities of interacting particles. The collisions that occur between incoming particles and stationary molecules result in processes such as ionization, excitation, and attachment [34, 64, 65].

2.6.2 Electron Impact Reactions

Sohbatzadeh and Soltani [66], performed an investigation of a time-dependent, one-dimensional model in atmospheric air on COMSOL Multiphysics. The simulation involved the modelling of a dielectric-barrier discharge in a Nitrogen-Oxygen-water vapor mixture at atmospheric pressure. The ratio of the Nitrogen, Oxygen, and water vapor mixture was 78%, 21% and 1% respectively. It was predicted by Lowke [67], that the presence of 1% of water vapor in air increases the breakdown fields by approximately 11%.

These reactions include effective processes such as the electron attachment, ionization, excitation, and elastic reactions. The electron impact reactions for Nitrogen, Oxygen, and water vapor that were used by Sohbatzadeh and Soltani [66] were used in this dissertation. The electron impact reactions for Nitrogen, Oxygen and water vapor are seen by referring to the Tables 1,2 and 3 respectively.

Table 1 - The electron impact reactions with the active species of Nitrogen used in this dissertation [66].

Reaction	Formula	Type	ΔE (eV)
R₁	$e + N_2 \rightarrow e + N_2$	Elastic Scattering	$\frac{m}{M} = 0.0000195$
R₂	$e + N_2 \rightarrow e + N_{2s}$	Excitation	6.725
R₃	$e + N_2 \rightarrow e + N_{2s}$	Excitation	8.05
R₄	$e + N_2 \rightarrow e + N_{2s}$	Excitation	8.217
R₅	$e + N_2 \rightarrow e + N_{2s}$	Excitation	8.95
R₆	$e + N_2 \rightarrow e + N_{2s}$	Excitation	8.974
R₇	$e + N_2 \rightarrow e + N_{2s}$	Excitation	9.562
R₈	$e + N_2 \rightarrow e + N_{2s}$	Excitation	9.665
R₉	$e + N_2 \rightarrow e + N_{2s}$	Excitation	10.174
R₁₀	$e + N_2 \rightarrow 2e + N_2^+$	Ionization	15.581

Where:

N_2 : Nitrogen molecule

N_{2s} : Metastable Nitrogen

N_2^+ : Ionized Nitrogen molecule

Table 2 - The electron impact reactions with the active species of Oxygen used in this dissertation [57].

Reaction	Formula	Type	ΔE (eV)
R₁	$e + O_2 \rightarrow e + O_2$	Elastic Scattering	$\frac{m}{M} = 0.000017$
R₂	$e + O_2 \rightarrow O + O^-$	Attachment	0
R₃	$e + O_2 \rightarrow e + O_2$	Excitation	0.02
R₄	$e + O_2 \rightarrow e + O_2$	Excitation	0.193
R₅	$e + O_2 \rightarrow e + O_2$	Excitation	0.386
R₆	$e + O_2 \rightarrow e + O_2$	Excitation	0.579
R₇	$e + O_2 \rightarrow e + O_2$	Excitation	0.772
R₈	$e + O_2 \rightarrow e + O_2$	Excitation	0.977
R₉	$e + O_2 \rightarrow e + O_2$	Excitation	1.627
R₁₀	$e + O_2 \rightarrow e + O_2$	Excitation	4.5
R₁₁	$e + O_2 \rightarrow e + O_2$	Excitation	6.1
R₁₂	$e + O_2 \rightarrow e + O_2$	Excitation	8.4
R₁₃	$e + O_2 \rightarrow e + O_2$	Excitation	9.3
R₁₄	$e + O_2 \rightarrow 2e + O_2^+$	Ionization	12.072

Where:

O_2 : Oxygen molecule

O^- : Negative Oxygen ion

O_2^+ : Ionized Oxygen molecule

Table 3 - The electron impact reactions with the active species of Water used in this dissertation [57].

Reaction	Formula	Type	ΔE (eV)
R₁	$e + H_2O \rightarrow e + H_2O$	Elastic Scattering	$\frac{m}{M} = 0.00003043$
R₂	$e + H_2O \rightarrow H_2O^-$	Attachment	0
R₃	$e + H_2O \rightarrow e + H_2O$	Excitation	0.206
R₄	$e + H_2O \rightarrow e + H_2O$	Excitation	0.459
R₅	$e + H_2O \rightarrow e + H_2O$	Excitation	1.058
R₆	$e + H_2O \rightarrow e + H_2O$	Excitation	8.445
R₇	$e + H_2O \rightarrow e + H_2O$	Excitation	14.052
R₈	$e + H_2O \rightarrow 2e + H_2O^+$	Ionization	13.76

Where:

H_2O : Water molecule

H_2O^- : Negative water ion

H_2O^+ : Ionized water molecule

2.6.3 LXCAT Database

The LXCAT website is an open-access site which is used for the collection, displaying, and downloading of electron scattering cross sections, ion-neutral interaction potentials, optical oscillator strengths and swarm parameters. Examples of these swarm parameters are mobility, diffusion coefficients, reaction rates, etc. This information is required for the modelling of low temperature, non-equilibrium plasma [68, 69].

The data that is extracted from the website can either be in the form of compilations of electron-neutral scattering cross sections or tables of swarm parameters as a function of the reduced electric field (E/N) [68]. Electron scattering cross sections is the data type that was used from the LXCAT database. The data type consists of total (angle integrated) cross sections for inelastic, attachment and ionization processes. It also consists of momentum transfer or viscosity cross sections for elastic processes which is mainly used for ground state target species [69].

Both, the Biagi [70, 71] and Hayashi [72] database was used to obtain the necessary scattering cross section data that was implemented in the model. The Biagi database consists of detailed cross section sets for noble gases as well as molecular gases such as H_2 , D_2 , N_2 , O_2 , and SF_6 [69]. The compilation of data was done by giving priority to cross sections that are measured using electron beam techniques. These are supplemented with an analysis from swarm experiments that use either a two-term Boltzmann solver or Monte Carlo simulations which have cross sections as an input [69].

2.6.4 The Cross Section Analysis of Nitrogen, Oxygen and Water

2.6.4.1 Nitrogen

Using the electron impact reactions in Table 1 found in section 2.6.2, the cross-section data for Nitrogen was obtained from the Biagi Database and is represented in Figure 11 [70]. It is a plot of the cross-section vs energy graph for the various excitation, elastic, and ionization electron impact reactions for Nitrogen.

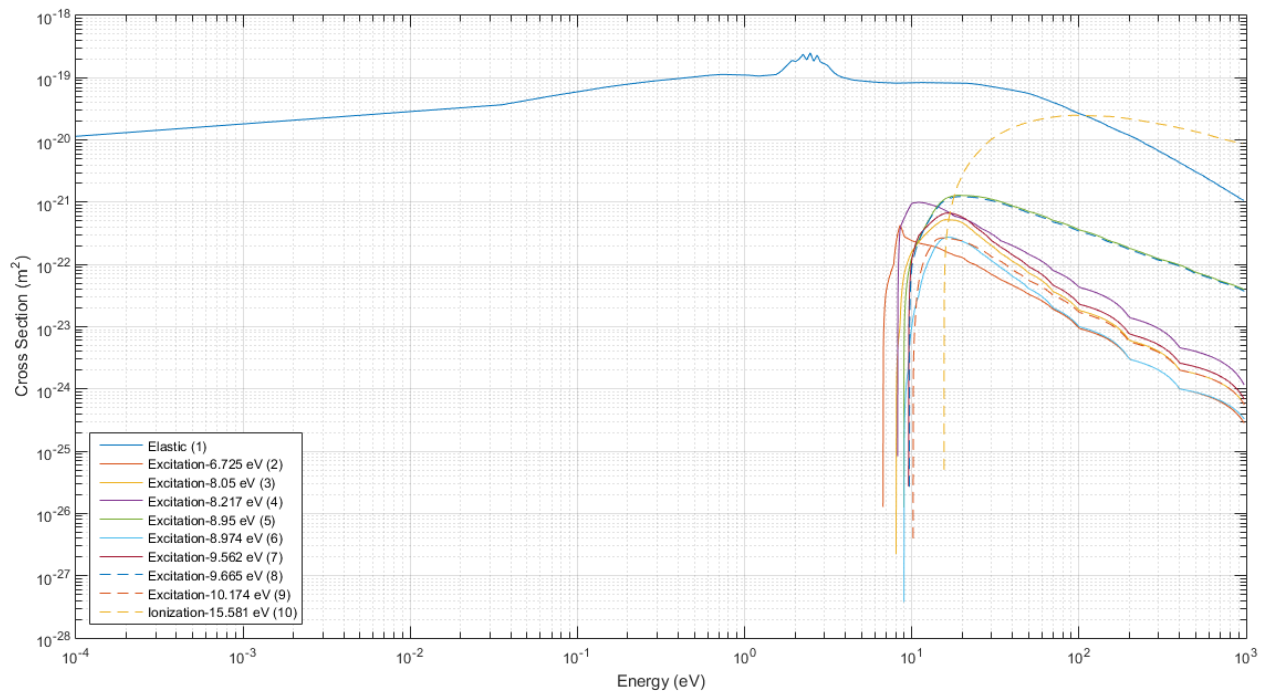


Figure 11 - Plot of the cross sections for electrons interacting with Nitrogen [70]. Take note that both the x-axis and y-axis are on a log scale.

The most common molecule present in the atmosphere on Earth is the Nitrogen molecule [73]. Electron collisions that occur with nitrogen molecules are essential processes in an electrical discharge that involves atmospheric gas [73].

The total cross section graph in Figure 11 was measured in the energy range of 0.0001-1000 eV. The elastic reaction (1) in Figure 11 is caused by electron impact and extends over the entire energy range. The probability of an elastic collision occurring increases as the energy levels increase but starts to decrease after 6 eV.

Excitation reactions (2-8) have the greatest probability occurring around 10-11 eV. This maximum value is generally an order of magnitude or lower than the vibrational cross section. The excitation reaction labelled (9) is an exception to this as it is a single-state excitation reaction which has a higher energy tail that is caused by the relatively large cross section [28].

It was observed that the probability of an ionization collision (10) occurring increases as the energy levels increase to 100 eV. As the energy level increases further there is a decrease in the probability of an ionization reaction occurring.

As indicated by Brown [74], the dielectric strength of Nitrogen is acceptable as the number of excited states that it has acts as a temporary energy sink. This temporary energy sink performs the function of retarding the acceleration of electrons thus keeping the electron energies low.

2.6.4.2 Oxygen

Using the electron impact reactions in Table 2 located in section 2.6.2, the cross-section data for Oxygen was obtained from the Biagi Database and is represented in Figure 12 [71]. It is a plot that represents the cross-section vs energy graph for the various excitation, elastic, attachment, and ionization electron impact reactions for Oxygen.

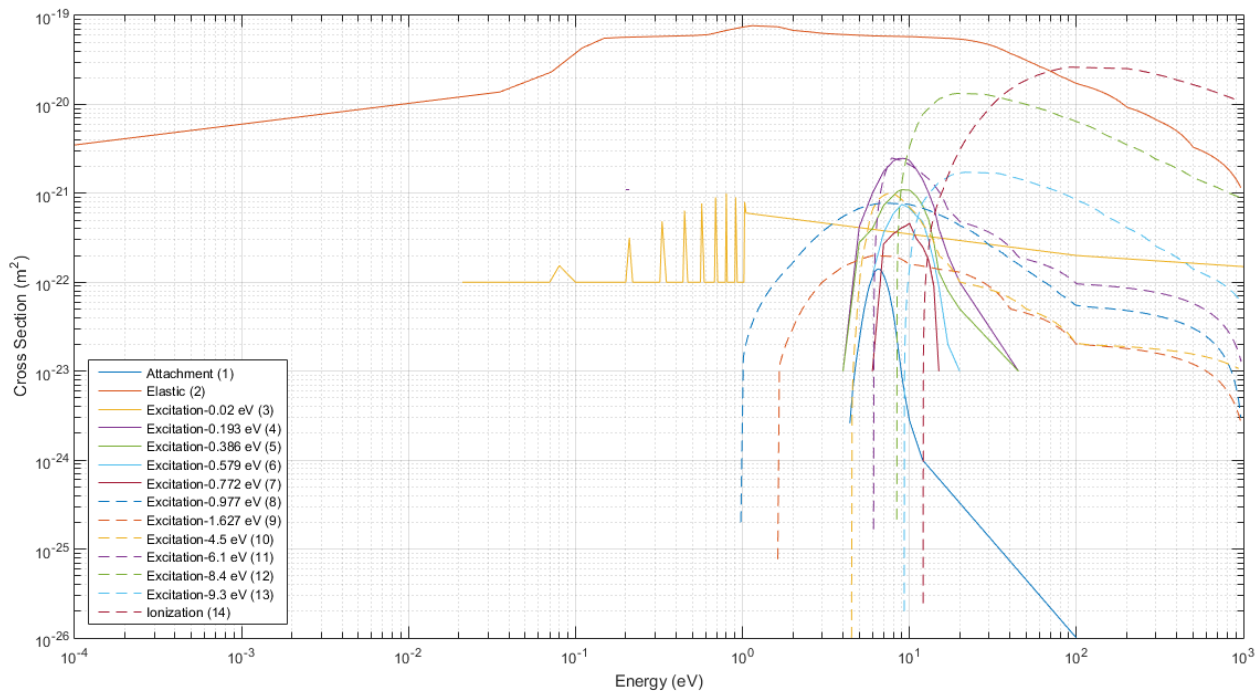


Figure 12 - Plot of the cross sections for electrons interacting with Oxygen [71]. Take note that both the x-axis and y-axis are on a log scale.

An essential component in Earth's atmosphere is the oxygen molecule. The molecule plays a significant role in several processing plasmas [75]. As indicated by Itikawa [75], Oxygen consists of low-lying metastable states and is one of the simplest electronegative gases in the atmosphere.

The total cross section graph in Figure 12 was measured in the energy range of 0.0001-1000 eV. An attachment collision (1) occurring by electron impact for an Oxygen molecule occurs in the region of the 0-100 eV and the probability of the attachment collision occurring reduces when the energy level

is greater than 6.5 eV. It is seen that the elastic collision (2) caused by electron impact extends over the entire energy range.

Majority of the excitation reactions (4-13) that are caused by electron impact may occur in the higher energy regions apart from (3). The ionization reaction (14) has a high-energy tail which corresponds to a relatively large cross section [28]. An ionization collision that happens by electron impact takes place in the energy range of 10 - 1000 eV and the probability of the collision occurring is directly proportional to the energy level when in range of 10 - 100 eV. The probability this reaction taking place then decreases as the energy level increases further.

2.6.4.3 Water

Using the electron impact reactions in Table 3 located in section 2.6.2, the cross-section data for water was obtained using the electron impact reactions from the Hayashi Database and is represented in Figure 13 [72]. It is a plot that represents the cross-section vs energy graph for the various excitation, elastic, attachment, and ionization electron impact reactions for water.

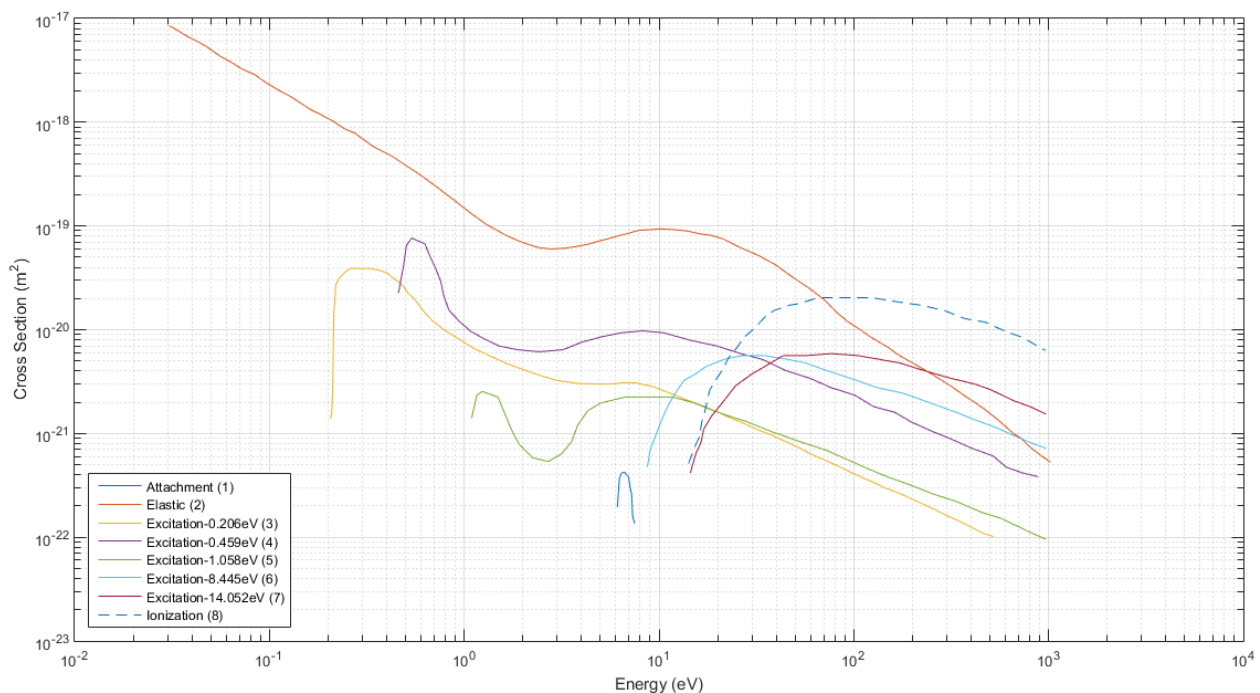


Figure 13 - Plot of the cross sections for electrons interacting with water [72]. Take note that both the x-axis and y-axis are on a log scale.

The total cross section graph in Figure 13 was measured in the energy range of 0.01-1000 eV. An attachment collision (1) that is brought about by electron impact occurs in the energy range of 6.1-7.5 eV and the probability of it occurring for a water molecule decreases when the energy range is greater than 6.73 eV. It is seen that the elastic collisions (2) that are brought on by electron impact may occur in the lower energy regions and the probability of it occurring reduces as the energy level increases.

Water molecules that experience ionization collisions (8) by electron impact may take place in the energy range of 10-1000 eV and the probability of the collision occurring increases as the energy level increases to approximately 100 eV. The probability of an ionization reaction taking place reduces when the energy level is greater than 100 eV. Excitation reactions (3-7) in water molecules occur in the energy range of 0.2-1000 eV and the probability of excitation reactions occurring decreases as the energy level increase.

2.6.5 BOLSIG+

A fluid model of a gas discharge is described by the transport of particles such as electrons, ions, and other reactive particle species by the first few moments of the Boltzmann Equation (BE). The continuity equation, momentum equation and the energy equation consist of transport coefficients or rate coefficients that are used to represent the effect of collisions [61]. This data was used as input data for the fluid model. The Boltzmann Equation for a collection of electrons that are present in an ionized gas is represented by equation 23 [61]:

$$\frac{df}{dt} + v \cdot \nabla f - \frac{e}{m_e} E \cdot \nabla_v f = C[F] \quad (23)$$

Where:

f : The electron distribution in six-dimensional phase space

v : Velocity coordinates

e : Elementary charge

m_e : Electron mass (9.11×10^{-28} g)

∇_v : Velocity-gradient operator

$C[F]$: The rate of change in F due to collisions

The BOLSIG+ program performs the function of solving the Boltzmann equation numerically for electrons that are present in weakly ionized gases that have both uniform electric fields and gas density. These conditions typically occur in collisional plasmas that have a low temperature. The data input of the program considers the cross section sets of the gas. These sets of data include the complete electron energy losses and momentum losses that occur due to collisions. The program outputs the EEDF, transport coefficients as well as the rate coefficients with the swarm parameters verses the reduced electric field from the collision cross section data provided [76].

The principles that BOLSIG+ assumes to perform its function are [76]:

1. The electric field is required to be uniform thus resulting in the collision probabilities being the same.
2. The program utilizes the classical expansion to approximate the angular dependence of the electron distribution.
3. The exponential growth model is considered because of the electron density varying. This is due to ionization and attachment processes.

Once these assumptions are made by the program, it results in the Boltzmann equation minimising to a convection-diffusion continuity-equation [76].

As indicated by Pusateri et al. [28], the ionization rate is expressed in equation 24 as [28]:

$$\frac{C_1(U_e)}{N} = \left(\frac{2\gamma}{m_e}\right)^{\frac{1}{2}} \int_0^{\infty} \varepsilon f(\varepsilon) Q_i(\varepsilon) d\varepsilon \quad (24)$$

Where:

U_e : Characteristic electron temperature (eV)

N : Number density of air molecules (cm⁻³)

γ : 1.6×10^{-12} eV/erg

ε : Electron energy (eV)

$f(\varepsilon)$: EEDF in eV^{3/2}

$Q_i(\varepsilon)$: Energy-dependent ionization cross section (cm²)

The EEDF is normalized and is represented in equation 25 [28]:

$$\int_0^{\infty} \frac{1}{\varepsilon^2} f(\varepsilon) d\varepsilon = 1 \quad (25)$$

2.6.6 Data Requirements for BolSig+ Simulation

To obtain the swarm parameters required for the fluid model, BolSig+ requires additional data which is seen below:

Reduced Electric Field Range (Td)

The reduced electric field range is a vital control parameter which is required for the BolSig+ program to perform its calculations. The calculations can be performed for a single value of E/N or in applications where a series of runs of E/N are required. E/N can be selected to increase either linearly, quadratically or exponentially provided the initial and final values are stated [77].

As indicated by Liu and Raju [63], a large amount of data has been published by various literature on the topic of electron transport coefficients for several gases over a wide range of reduced electric fields. Partial discharges require swarm parameters in the range of 750 to 1200 Td whilst high pressure breakdowns require swarm parameters in the range of 90 to 150 Td. Reduced electric field values in the intermediate range is required to perform a theoretical analysis of leader and streamer propagation that is located ahead of the streamer avalanche.

Ndong and Ndama [78], performed an investigation of the breakdown performance of N_2/O_2 gas mixtures in quasi-homogenous electric fields. The investigation involved the comparison of the reduced ionization coefficient from various sources of literature to the BOLSIG+ data that was obtained from the program. The comparison of the various ionization coefficients was done using a reduced electric field range of 0 to 200 Td.

Serdyuk [79] modelled a cathode directed streamer discharge in air using COMSOL Multiphysics. The swarm parameters were obtained using a reduced electric field in the range of 0 to 800 Td.

A reduced electric field range of 0 to 1000 Td was used for the numerical simulation done in this dissertation.

Gas Temperature (K)

The gas temperature is a parameter that controls the elastic energy transfer at low E/N [80].

The magnitude of the gas temperature used was obtained from Sima et al. [81], therefore the temperature of the plasma was set to 300 K.

Gas composition

The gas composition represents the percentage composition of the different particle species in the gas mixture [77]. A vital parameter of the system as it influences the decay mechanism of the plasma in the streamer channel. The rate of plasma decay of air in the early stages are dependent on the

dissociative recombination of electrons with complex positive ions. The latter stage of this decay is dependent on the three-particle attachment of electrons to Oxygen molecules. Negative ions are a result of these reactions, and these ions can lose electrons when colliding with monatomic Oxygen atoms or other active particles that are produced in the streamer head [82].

The percentage composition used was the same air composition that was also used by Sohbatzadeh and Soltani [66] and is stated in section 2.6.2.

Electron-electron Collisions

Electron-electron collisions are collisions that result in the EEDF tending towards a Maxwellian distribution function. It is dependent on the ionization degree and as the ionization degree increases it causes the EEDF to resemble the Maxwellian distribution function more. The inclusion of electron-electron collisions in fluid models is important as it increases the rate coefficients of inelastic collisions by repopulating the tail end of the EEDF [61].

Electron-electron collisions were included in the BolSig+ simulation performed in this dissertation.

Ionization Degree

The ionization degree is defined by Hagelaar [77], as the ratio of the electron number density to the neutral particle number density. It is a parameter that controls the Coulomb collisions and was set to 1×10^{-5} .

Plasma density ($1/m^3$).

According to Hagelaar [77], the plasma electron number density is required so that the calculation of the Coulomb logarithm can be obtained. This has a weak effect on the actual results hence an estimation of the order of magnitude for the plasma density is sufficient.

The value used for the plasma density was $1 \times 10^{18} 1/m^3$.

2.7 Results of the BolSig+ Simulation

The tabulated values obtained from the BolSig+ simulation for the reduced electric field, electron energy, electron mobility, diffusion, Townsend ionization and attachment coefficients are seen by referring to Table 10 in Appendix A.

The results from the simulation are plotted against the reduced electric field and are analysed.

2.7.1 Mobility

The electron mobility results obtained from simulation is plotted against the reduced electric field and is shown in Figure 14 [61].

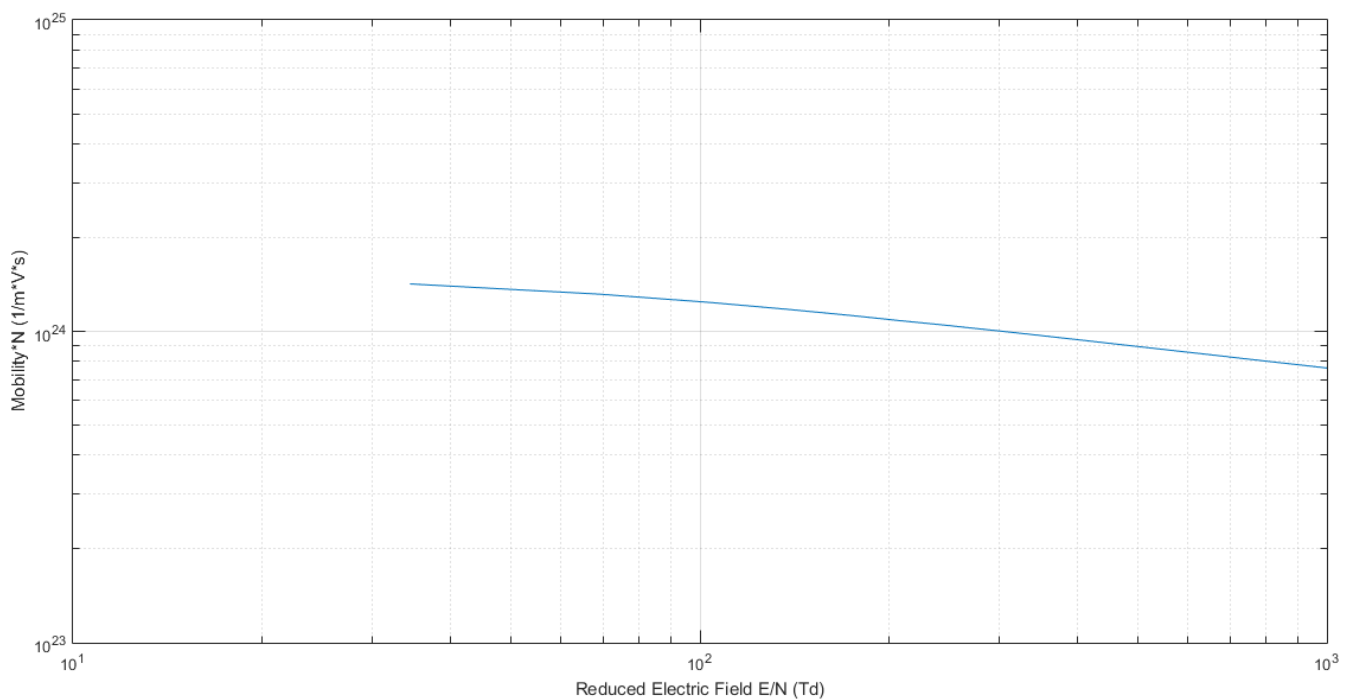


Figure 14 - Plot of the electron mobility as a function of the reduced electric field [61]. Both the x-axis and y-axis are on a log scale.

As seen in the above figure, the reduced electron mobility is indirectly proportional to the reduced electric field. This is expected as the higher reduced electric field causes the electron energy to increase thus resulting in an increase in the probability of electron collisions occurring. The movement of a single electron in the forward direction continuously changes when colliding with other particles thus causing the approximations of the electron mobility to decrease. The inclusion of water in the system results in a reduction in the average electron energy in air at points where the electric field is low. This causes the electron mobility to be slightly higher with a reduction in the probability of electron collisions occurring. This is brought upon by the decrease in electron energy [83].

2.7.2 Diffusion

The diffusion coefficient was obtained by simulation and is plotted against the reduced electric field in Figure 15 [61].

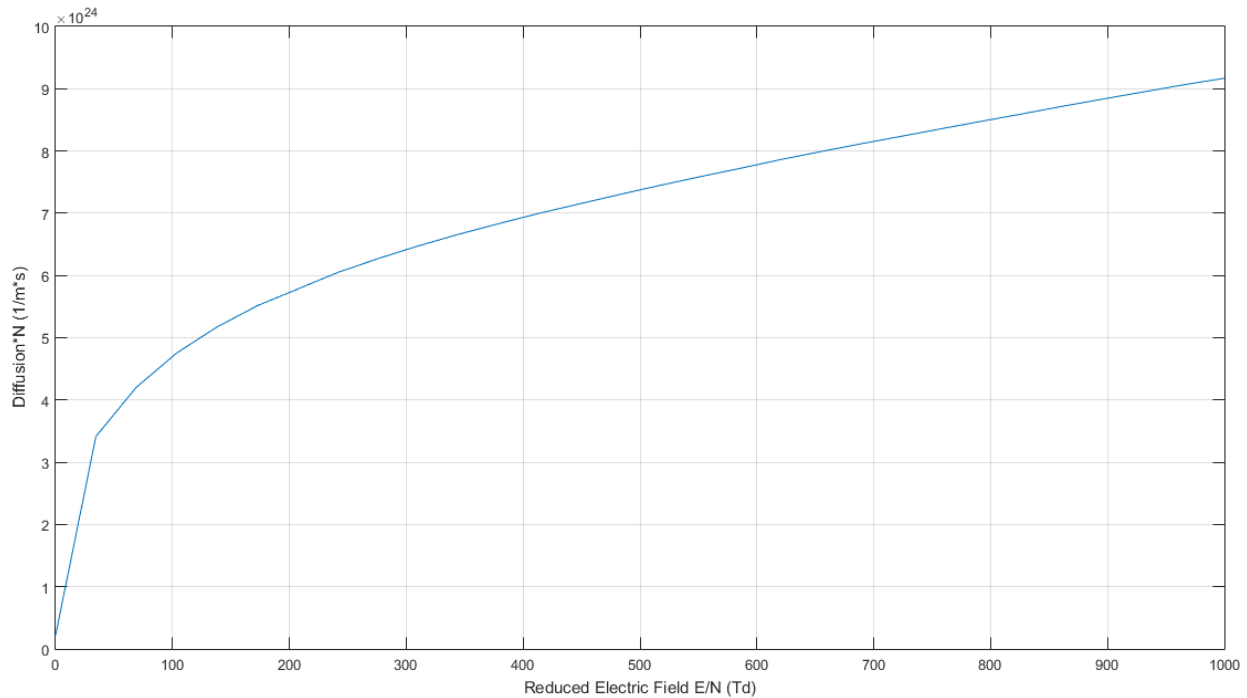


Figure 15 - Plot of the diffusion coefficient as a function of the reduced electric field [61].

As seen in figure above, the electron diffusion is directly proportional to the reduced electric field. The random thermal motion of electrons is linked to the electron energy and is related to the diffusion coefficient in a system. As the electron energy increases so does the intensity of random thermal motion. This consequently impacts the electron diffusion coefficient by increasing in magnitude. The introduction of water in the system causes the average electron energy to decrease under a low electric field and increase under a high electric field as seen in Figure 15 [83].

2.7.3 Townsend Ionization and Attachment Coefficients

It is essential to obtain the ionization and attachment coefficient as it is used to perform an analysis of the growth of the electron number density in the Townsend theory of gas discharge. The Townsend coefficient is obtained using equation 26 below [83]:

$$\alpha_{\kappa} = \frac{\kappa_{\kappa} N_n}{\mu E} \quad (26)$$

Where:

κ_{κ} : Rate coefficients

The Townsend ionization coefficient and Townsend attachment coefficient are obtained using equation 27 and 28 respectively [83].

$$\alpha = \sum_{\text{ionization}} \alpha_{\kappa} \quad (27)$$

$$\eta = \sum_{\text{attachment}} \alpha_{\kappa} \quad (28)$$

Where:

α : Townsend's ionization coefficient

η : Townsend's attachment coefficient

Both Townsend ionization and attachment coefficients were obtained by simulation and are plotted against the reduced electric field in Figure 16 [61].

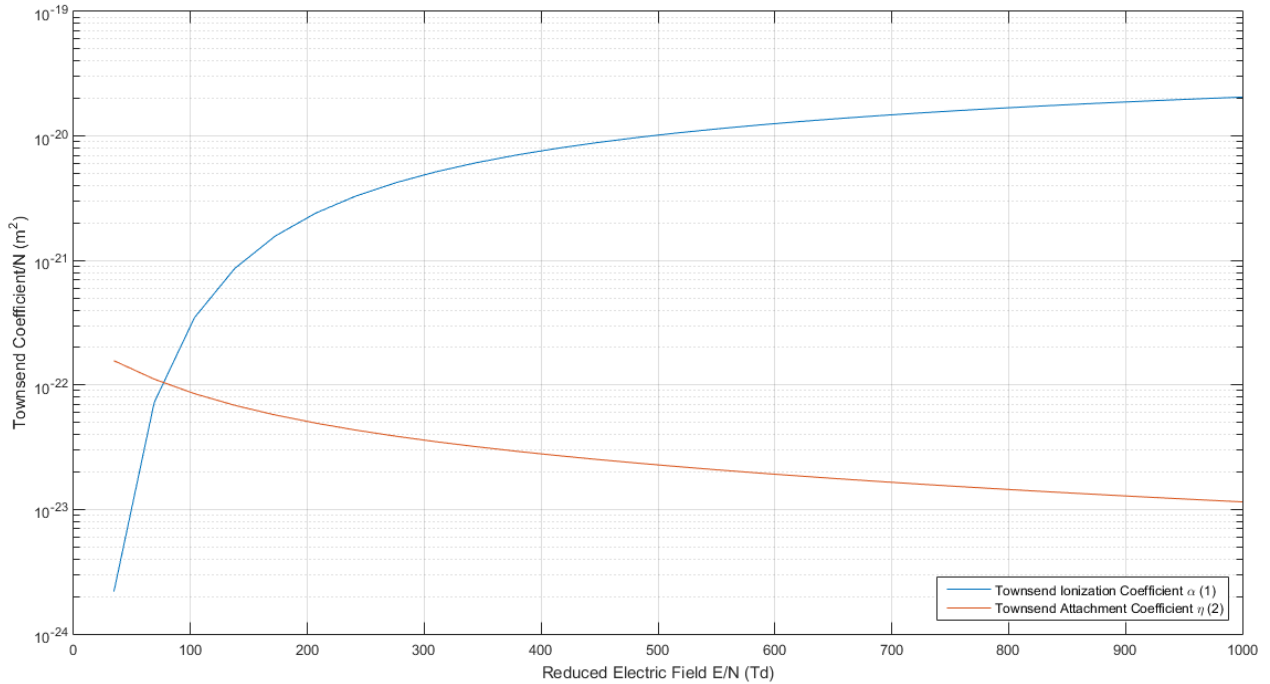


Figure 16 - Plots of the Townsend ionization and Townsend attachment coefficient as a function of the reduced electric field [61]. It should be noted that the y-axis is only on a log scale.

As seen in the figure above, the Townsend ionization rate coefficient increases sharply in the region of 40-120 Td and continues to increase as the reduced electric field increases. The Townsend attachment rate coefficient is at its peak in the lower energy range but as the energy levels continue to increase there is a reduction in the magnitude of the attachment coefficient.

2.7.4 Effective Ionization Coefficient

Pancheshnyi [84, p. 1], defined the effective Townsend's ionization coefficient, "as the number of electrons produced by an electron per unit length of path in the direction of the field". The effective ionization coefficient is obtained by using equation 29 below [84]:

$$\alpha_{eff} = \alpha - \eta \quad (29)$$

Where:

α_{eff} : Effective ionization coefficient

Using equation 29, the effective ionization coefficient was obtained using the Townsend ionization and attachment coefficients from Table 10. The result is plotted against the reduced electric field in Figure 17. The MATLAB code created to calculate the effective ionization coefficient is seen by referring to Appendix A.

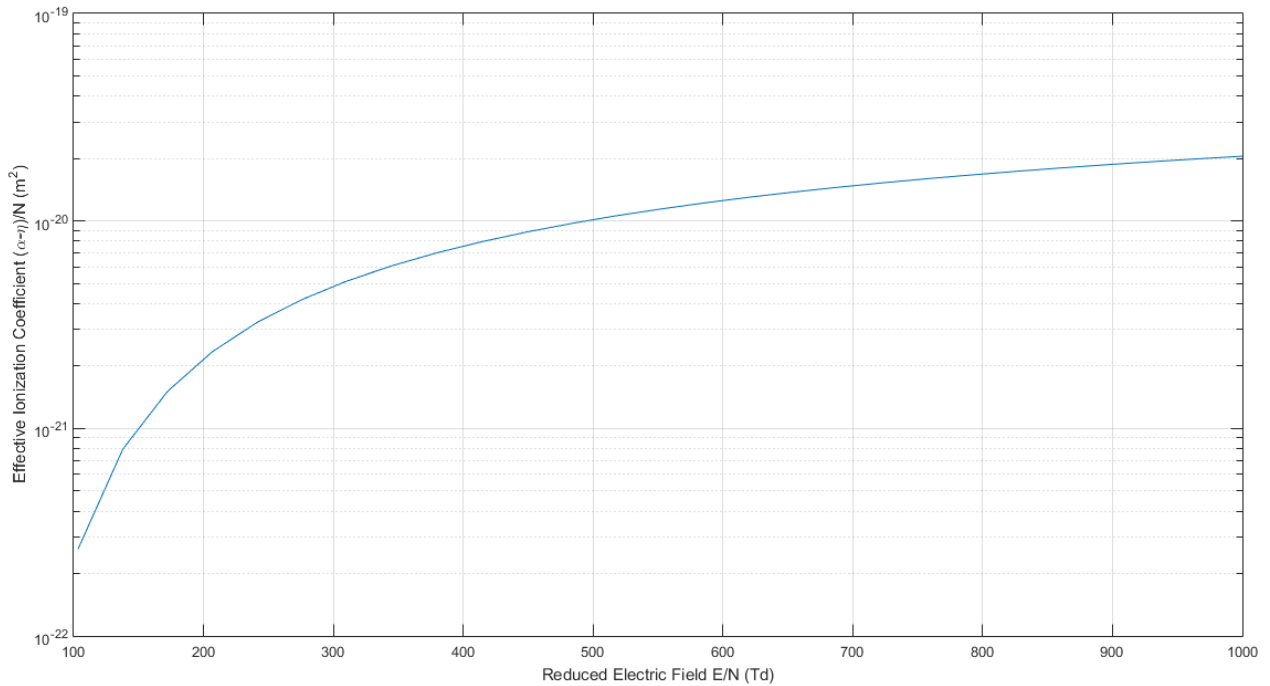


Figure 17 - Plot of the effective ionization coefficient as a function of the reduced electric field [61]. It should be noted that the y axis is on a log scale.

As seen in the figure above, the effective ionization coefficient is low when the reduced electric field magnitude is low and as the magnitude of the electric field increases, so does the magnitude of the effective ionization coefficient.

The inclusion of water in the gas composition causes an enhancement of the attachment and ionization reactions. This results in the effective ionization coefficient being reduced in the lower regions of the reduced electric field and increases in the greater regions of the reduced electric field. This is due to the attachment coefficient being dominant when the electron energy is low. As the electron energy increases, the ionization coefficient becomes dominant [83]. The swarm parameters obtained are used in the numerical modelling of a cathode directed streamer in Chapter 4.

3 Streamer Breakdown of Air Experiment

A significant amount of high voltage equipment and power apparatus implement atmospheric air as an electrical insulator and most of this equipment play an important role in the electrical power system [85, 48, 86]. Therefore, it is essential that the insulation be of an acceptable standard whilst maintaining its high electrical insulation properties to ensure continuity and reliability of the electrical network [85, 86]. Experiments are still required to be performed as certain physical phenomena cannot be fully explained by only using theoretical means. Therefore, experiments are essential and are still regarded as the basis for scientific research [86].

The investigation of streamer development is important as it determines the breakdown characteristics of multiple electrode arrangements especially when a lightning impulse voltage or direct voltage is applied [87]. As indicated by Luque et al. [88], a positive streamer emerges from an electrode with a pointed tip at voltages lower in magnitude when compared to negative voltages. This makes it an important component to consider for electrical system design hence investigations performed in the past focused on positive streamers.

Both Radmilovic - Radjenovic et al. [48], and Mikropoulos et al. [87], performed an investigation to determine the influence of humidity on the breakdown voltage of a uniform air gap when HVDC is applied. The results obtained from both [48] and [87] indicated that the breakdown voltage is directly proportional to the humidity. Hussian et al. [5], also performed the same investigation but used a sphere - sphere air gap and a rod - plane air gap. The results obtained concluded that humidity did not influence the breakdown voltage significantly in a sphere - sphere electrode arrangement but there was a linear relationship that existed between the humidity and the breakdown voltage in a rod - plane air gap.

As stated previously, the experiment conducted by Rodriguez et al [10], investigated the influence of humidity on the breakdown voltage of various gaps using AC voltage that had frequencies of 30 kHz and 60 kHz. The results obtained from the experiment concluded that the breakdown voltage for short hemispherical rod - plane gaps (8–45 mm) was independent of humidity and electrical corona was absent prior to breakdown for both frequencies. It was also seen that electrical corona depended on the gap spacing for rod – rod and conical rod -plane gaps and if it occurred then the breakdown voltage would decrease when the humidity increased. The breakdown voltage was also independent of humidity despite their being corona streamers present prior to breakdown for all electrode arrangements that were in the range of 125–1000 mm.

Tarasenko et al. [89], conducted an experiment that investigated the breakdown of atmospheric air in a non-uniform electric field using an ICCD camera. The use of that type of camera allowed for the research into the dynamics that are involved in the formation of a streamer. It was observed from the

results that the streamer elongates and reduces in diameter after it crossed half the distance of the gap when approaching the plane electrode. The results also concluded that single streamers develop from needle electrodes as it causes a maximum local electric-field enhancement.

Seeger et al. [18] investigated both streamer and leader breakdown mechanisms for air gaps less than a metre. The experiment involved observing pre-breakdown discharges and breakdown paths using a high-speed camera and an image intensifier. A spherical tipped electrode was used and separated from the grounded electrode by 50 mm. Results showed that there was a formation of high luminosity stems which occurred when the voltage applied to the electrode was for a short period of time. This indicated that the leader inception occurred by the stem mechanism. When the voltage applied to the electrodes was in the time of 10 to several 100 μ s, then the breakdown voltage would be the lowest in magnitude provided the stem mechanism occurred.

This chapter features the setup of the experiment that was performed as well as the procedures that were followed to conduct the investigation. The experiment involved the investigation of the streamer breakdown when HVDC was applied to a needle-plane air gap. High-speed photography was also conducted to record the initiation and propagation of streamers for various gap lengths. The experiment consisted of determining the breakdown voltage for 5 different gap lengths and this was performed over 4 days that varied in atmospheric conditions. This chapter includes the results as well as the images of the streamers that were obtained from the experiment. These results were then used to determine whether atmospheric conditions such as humidity or pressure influence the breakdown voltage. The results were atmospherically corrected according to IEEE standards for high-voltage testing techniques [90]. An analysis of the results obtained was performed and is included in this chapter.

3.1 Experimental Setup

The experimental procedure was conducted in the High Voltage DC (HVDC) laboratory located in the Westville Campus, UKZN. The experiment was performed to investigate the streamer breakdown for air gaps less than 15 cm in length. It also included an investigation which determined the influence humidity and pressure has on the breakdown voltage. High-speed photography was implemented to capture the streamer breakdown mechanism that occurred in these short gap lengths and allowed for the observation of the paths a streamer would take when propagating. The implementation of this process assisted in determining whether space charge influences the path a streamer takes when propagating.

3.1.1 Experimental Procedure Layout

The experimental setup consisted of a 2 stage Cockcroft-Walton DC generator that is rated at 500 kV but is operated at a maximum voltage of 250 kV due to clearance limitations in the laboratory. A Phantom high-speed camera was used to capture the streamer breakdown at the required frame rates. Figure 18 below indicates the setup that was implemented for the investigation of the streamer breakdown for various air gaps. The circuit diagram for the high voltage DC generator is seen by referring to Figure 56 in Appendix B.

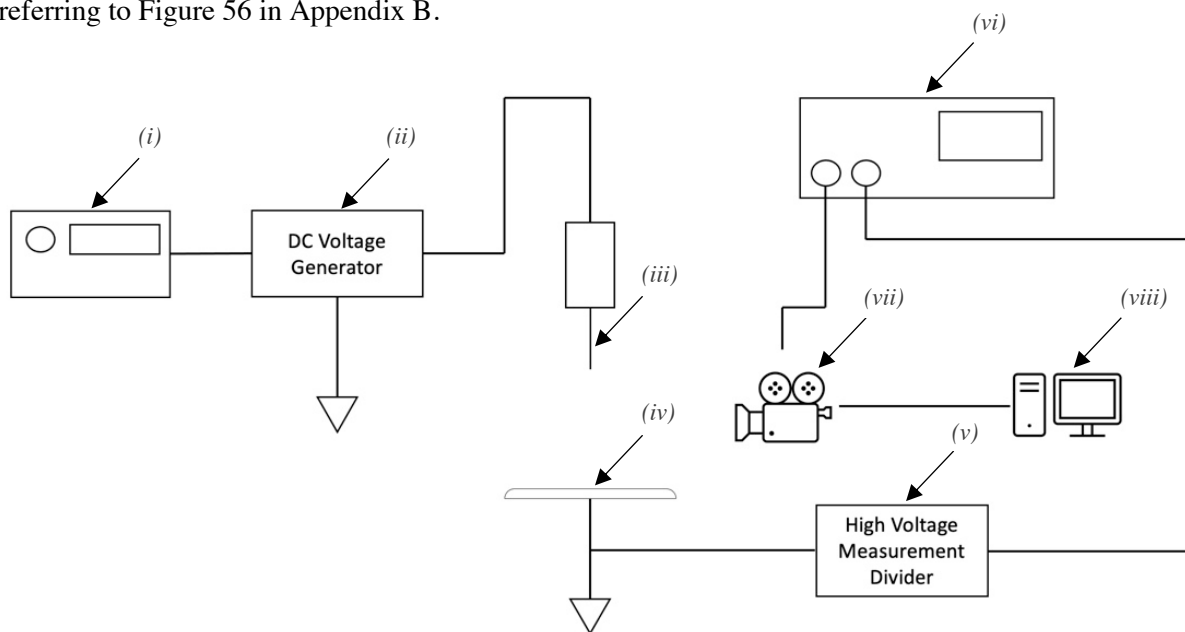


Figure 18 - The layout for the experimental procedure: (i) – HVDC control unit, (ii) – HVDC generator, (iii) – High voltage needle electrode, (iv) – Grounded plane electrode, (v) – High voltage measurement system, (vi) – Oscilloscope, (vii) – High speed camera (viii) – Computer

A needle-plane configuration was used to conduct the experiment as seen in Figure 19. The needle which was connected to the high voltage was made of iron and had a cylindrical body that was 12 cm in length whilst the diameter of the body was 0.1 cm. The plane electrode has a diameter of 16 cm and is connected to ground. The experiment was conducted for gap distances of 2 cm, 5 cm, 10 cm, 12 cm, and 15 cm.

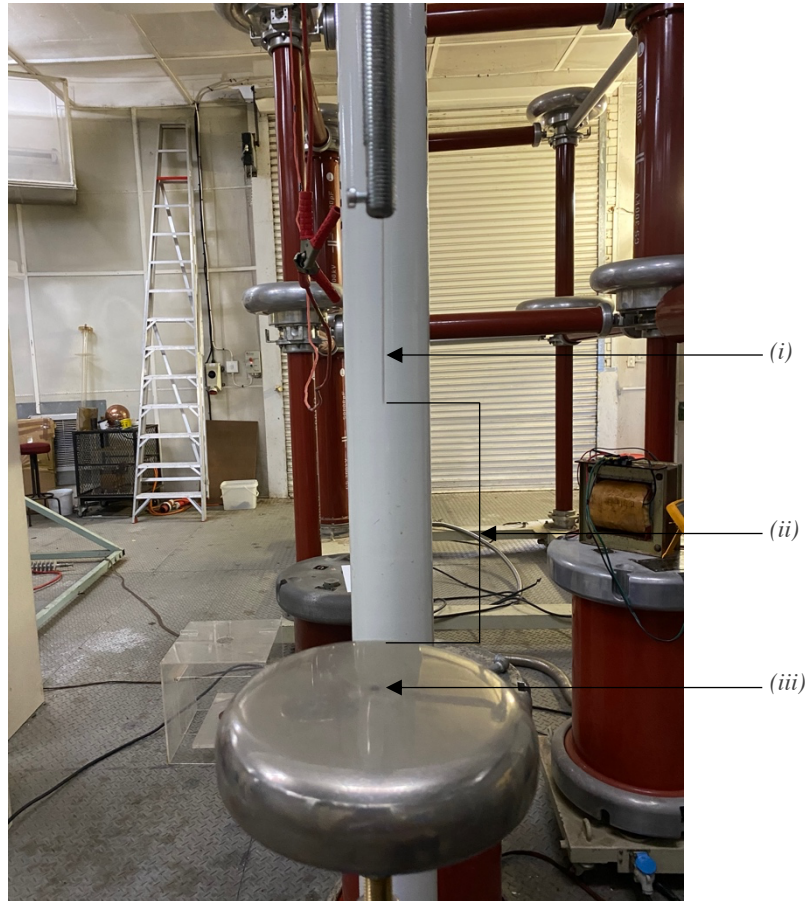


Figure 19 - The needle-plane electrode configuration implemented in the experimental procedure: (i) – High voltage needle electrode, (ii) – Varied gap distance, (iii) – Grounded plane electrode

An autonomous system was utilized to set the gap length between the two electrodes as it was continuously changed throughout the experiment. This ensured that the distances between the electrodes were accurate as well as the gap length between the electrodes were kept constant whilst the experiment was being conducted. This was done by using the Haefely Hipotronics vertical sphere gap system as seen in Figure 20.

The system consisted of a stationary rod to which the high voltage lead was connected to. The needle electrode was held in position using this rod whilst the grounded plane electrode was mounted on a mechanical shaft. This mechanical shaft moved in a vertical direction thus enabling the user to set the gap length when required to. The control unit is also seen in Figure 20 and was used to control the mechanical shaft thus allowing the autonomous setting of the gap distance. The calibration procedure for the Haefely Hipotronics vertical sphere gap system is explained in Appendix B.

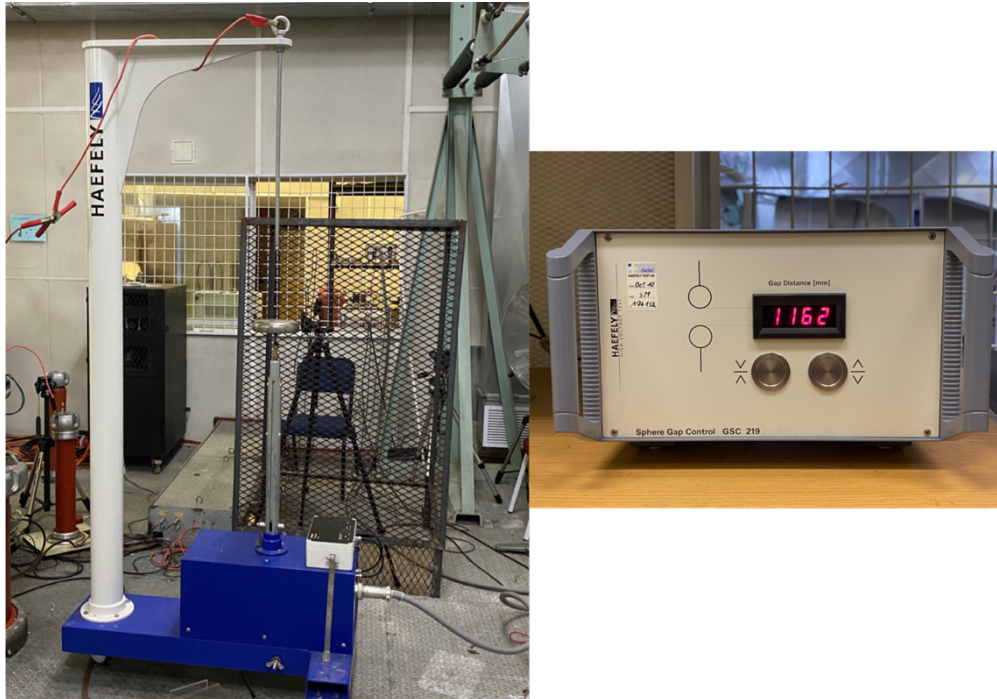


Figure 20 - The Haefely Hipotronics vertical sphere gap system with its control unit for autonomous operation. The control unit is set to 1 162 mm which represents a gap length of 15 cm between the high voltage and grounded electrode.

3.1.2 Oscilloscope

A Yokogawa DL9140 digital oscilloscope was used in the experimental procedure to measure the voltage when the breakdown occurred in the gap. The device was also used to trigger the high-speed camera to stop recording the instant when breakdown occurred. Figure 21 below is a picture of the oscilloscope used and the collapse of the applied voltage can also be seen, which happens when an electrical breakdown occurs.

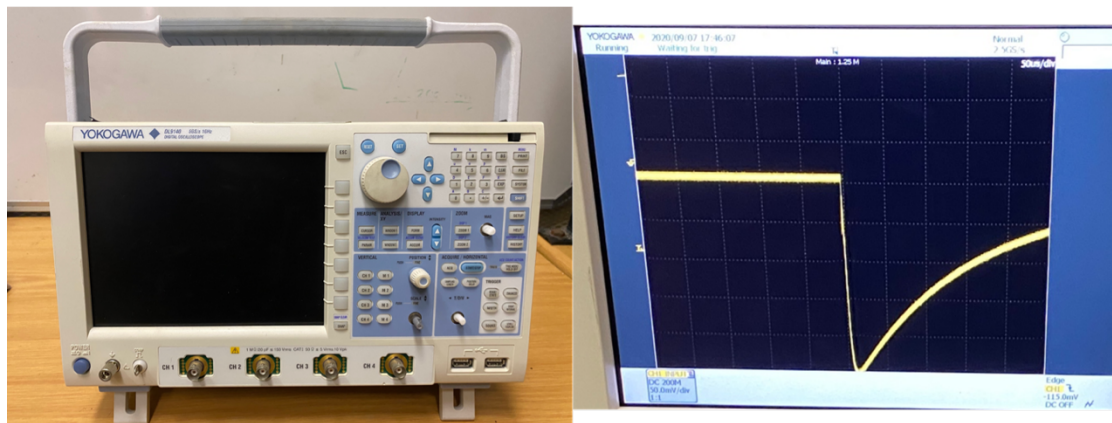


Figure 21 - A Yokogawa DL9140 digital oscilloscope. The image on the right indicates that electrical breakdown has occurred in the air gap as the applied voltage has collapsed.

3.1.3 Phantom Miro M110 High Speed Camera

Streamers were observed using a Phantom Miro M110 high speed monochrome camera which had a Nikon AF NIKKOR 50 mm 1:1.8 D lens attached. The camera was positioned 1 m away from the electrodes in a direction that allowed it to be perpendicular to the axis of the air gap. The camera was set to record at 300 000 frames per second with an exposure time of 2.94 ms using a resolution of 64x8 pixels. The aperture is an adjustable opening in the lens which allows for a certain amount of light to pass through and enter the camera [91]. It was required to set the aperture on the lens to f/1.8 to allow for maximum light to pass through when recording the experiment.

The experimental setup with the inclusion of the high-speed camera is seen by referring to Figure 22. A cage was designed and fabricated as seen in the figure below. It was electrically grounded in the laboratory when conducting the experiment. This was done to prevent any damage to the high-speed camera that may result from an electrical arc discharge.

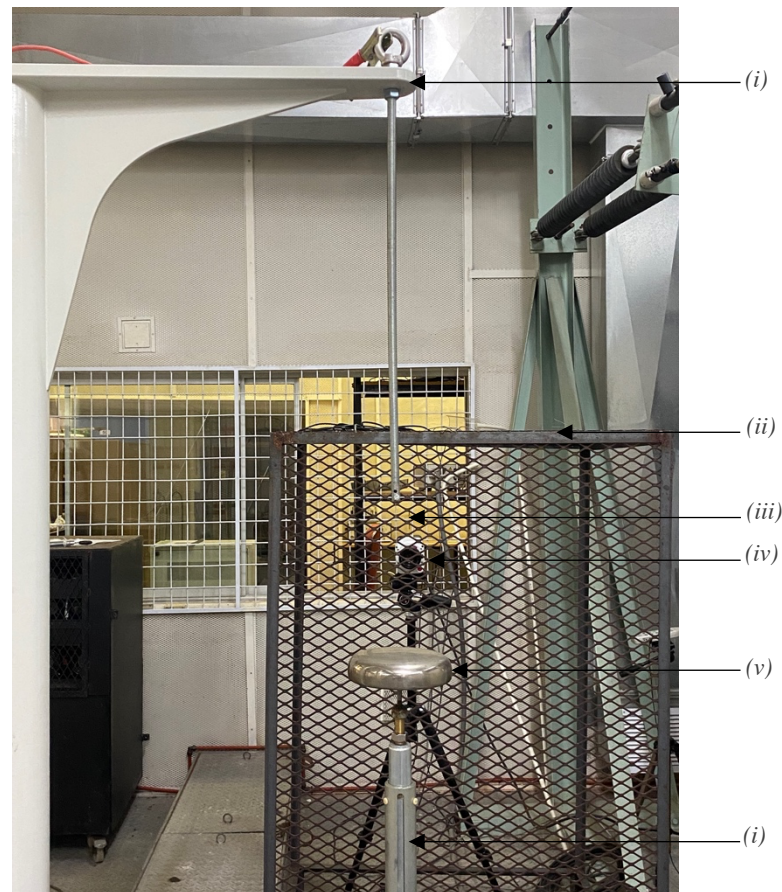


Figure 22 - The experimental setup that was implemented with the inclusion of a high-speed camera for recording the streamer breakdown of various air gaps. The cage that was designed and fabricated to protect the camera from an arc discharge is also seen. (i) - Haefely Hipotronics vertical sphere gap system. (ii) - Grounded steel cage. (iii) - High voltage needle electrode. (iv) - Phantom Miro M110 high speed camera. (v) - Grounded plane electrode.

3.1.4 Experimental Test Procedure

The experimental test that was conducted was done according to the procedure and standards that were set out in the IEEE standards for high-voltage testing techniques [90]. The test performed was a disruptive discharge voltage test which consisted of a HVDC voltage being applied to a needle electrode. The procedure for the test is stated below.

As stated previously, the experiment was conducted for various electrode distances hence it was first required to set the gap length between the electrodes to 2 cm. The high-speed camera was then turned on and recording of the experiment started.

The voltage applied to the high voltage electrode at the beginning of the test was required to either be a voltage of low magnitude or 0 V. This was done to prevent any effect of an overvoltage that may be caused by switching transients. In the experiment conducted, the starting voltage for the experiment was 0 V [90].

The magnitude of the voltage was increased at a certain rate to allow accurate measurement but also to prevent any prolonged stress on the electrodes. To ensure this was done accurately, the voltage was increased at a rate of 2% per second of the breakdown voltage [90]. For example, the breakdown voltage of air for a 2 cm gap length was 16.28 kV and 2% of this value was equal to 0.3256 kV. Therefore, the voltage was increased at a rate of 0.3256 kV per second.

Once breakdown of the air gap had occurred, the magnitude of the voltage that had just been reached before the breakdown would be recorded as the breakdown voltage [90]. The high-speed camera also stopped recording the instant breakdown took place as it would have been triggered to stop by the oscilloscope.

The disruptive discharge voltage test was repeated 5 times for each gap length for accuracy and the average of these results was obtained and used as the breakdown voltage.

The gap length was then increased using the autonomous system mention in section 3.1.1, and the entire process was repeated.

3.2 Results

The breakdown voltage of an external insulator is dependent on atmospheric conditions. Humidity as well as air density are factors that influence the dielectric strength of air. Hence, it is required that these factors are considered when performing the design as well as testing of external insulation. The use of correction factors on the results causes these voltages to be converted to an equivalent value that would be obtained under test conditions [92].

The results were then corrected to obtain the equivalent value using method 2 of the standard atmospheric correction procedure that was set out by the IEEE standards for high voltage testing techniques [90]. This method was used as it is ideal for air gaps less than a meter [90]. The procedure for atmospheric correction that was performed on the experimental results is seen in Appendix B. Henceforth, the corrected voltage was used when doing the necessary comparisons and analysis in this dissertation.

3.2.1 Comparisons of Breakdown Voltage to the Gap Length Between Electrodes

Figure 23 depicts the effect that the electrode spacing has on the breakdown voltage of an air gap.

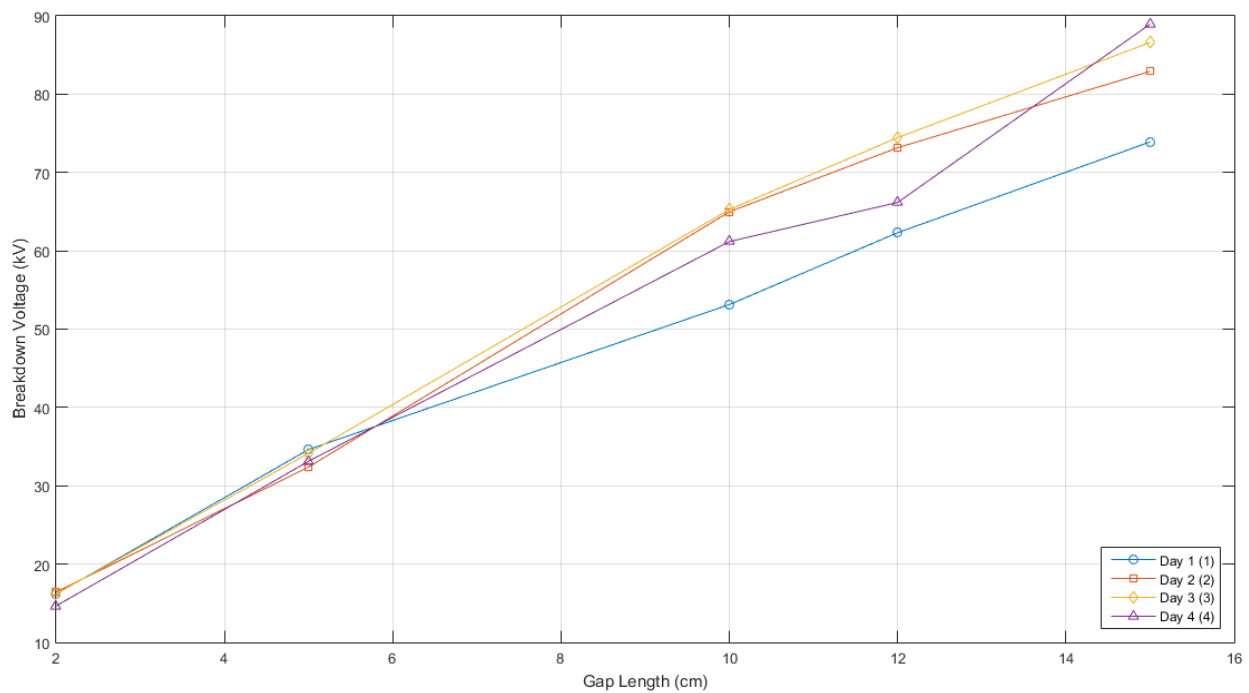


Figure 23 - The results obtained from the experimental procedure indicating the different breakdown voltages of various air gap lengths obtained over the course of 4 days.

The breakdown voltage for a gap length of 2 cm is in the range of 14.66-16.43 kV whilst the breakdown voltage is in the range of 33.35-38.40 kV for a gap length of 5 cm. When the gap length is set to 10 cm and 12 cm the breakdown voltages are in the range of 53.14-65.28 kV and 62.31-74.45 kV respectively. Lastly, the breakdown voltage is in the range of 73.90-88.94 kV for the largest gap length in the experiment which is 15 cm.

As observed in Figure 23 and seen in the results tabulated in Appendix B, the breakdown voltage of the air gap is directly proportional to the distance between the electrodes. As indicated by Fan et al. [56], an inversely proportional relationship exists between the strength of the electric field and the electrode distance. This results in a greater voltage being required for a larger gap to produce an electric field that has a magnitude which is sufficient to overcome the dielectric strength of the insulator.

It can also be seen that there is a slow increase in the breakdown voltage. There is not a completely linear increase in the breakdown voltage as the distance between the electrodes increase. The creation of a non-uniform electric field between the high voltage and grounded electrodes results in the relationship between the breakdown voltage and gap length not being completely linear [86].

These relationships align with the investigation performed by Menesy et al [86].

3.2.2 Electric Field Strength

As indicated in [93], the electric field strength that is required to initiate ionization processes and corona discharges in atmospheric air is approximately 3×10^6 V/m. This suggests that electrical breakdown voltage of air is approximately 3×10^6 V/m for a uniform or a weakly non-uniform electric field. As the applied voltage increases, it results in a gas discharge developing at a rapid rate thus turning into a streamer that leads to the breakdown of the gaseous gap. Figure 24 below, represents the results of a simulation obtained from FEMM v4.2 that depicts the distribution and strength of an electric field that is created when a high voltage is applied to a needle electrode.

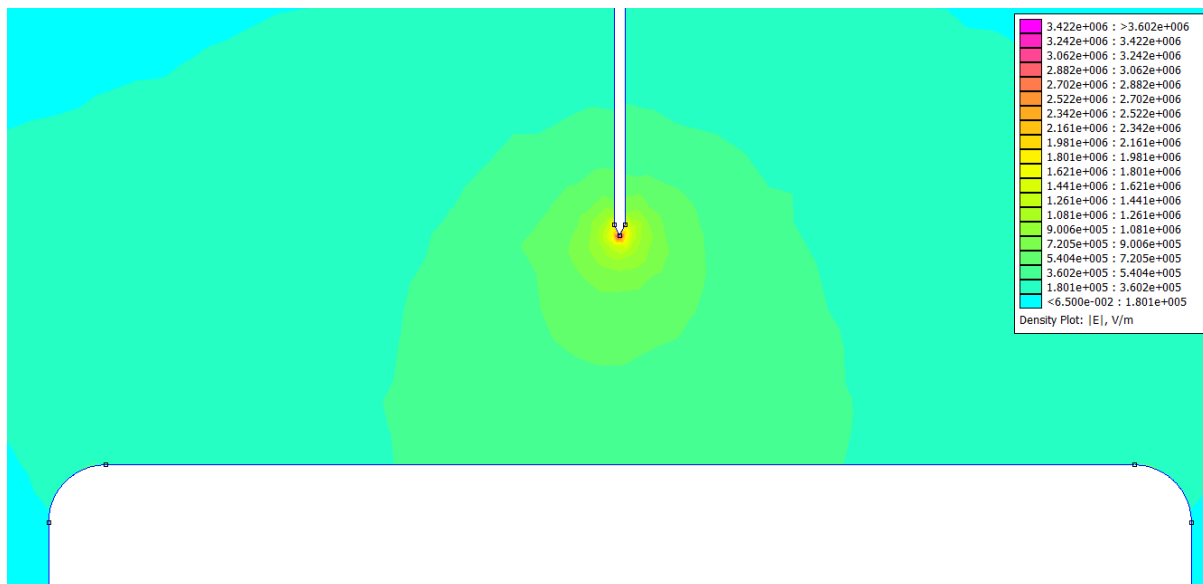


Figure 24 - A FEMM model showing the electric field created between a needle and plane electrode in air. The electrodes are separated by a distance of 2 cm and a voltage of 14.66 kV is applied to the needle electrode.

The needle and plane electrode are surrounded by air and these electrodes are separated by 2 cm. The plane electrode is grounded, and this electrode configuration creates an extremely non-uniform electric field [93].

Using the results obtained from the experiment, a breakdown voltage of 14.66 kV was applied to the needle electrode in the model. It is seen in the figure that the electric field is more concentrated towards the tip of the anode. The strength of the electric field is low in magnitude on the surface of the plane electrode as it is grounded. It can also be seen that the maximum electric field strength located around the anode is 4.0373×10^6 V/m and this magnitude is greater than the dielectric strength of air. Therefore, the electric field strength is sufficient to initiate ionization processes, and this led to the electrical breakdown of the air gap.

3.2.3 Comparisons of Breakdown Voltage to the Absolute Humidity

Figure 25 represents the breakdown voltage plotted against the absolute humidity for 2 cm (blue circles), 5 cm (red squares), 10 cm (yellow diamonds), 12 cm (purple triangles) and 15 cm (green hexagons) gap lengths.

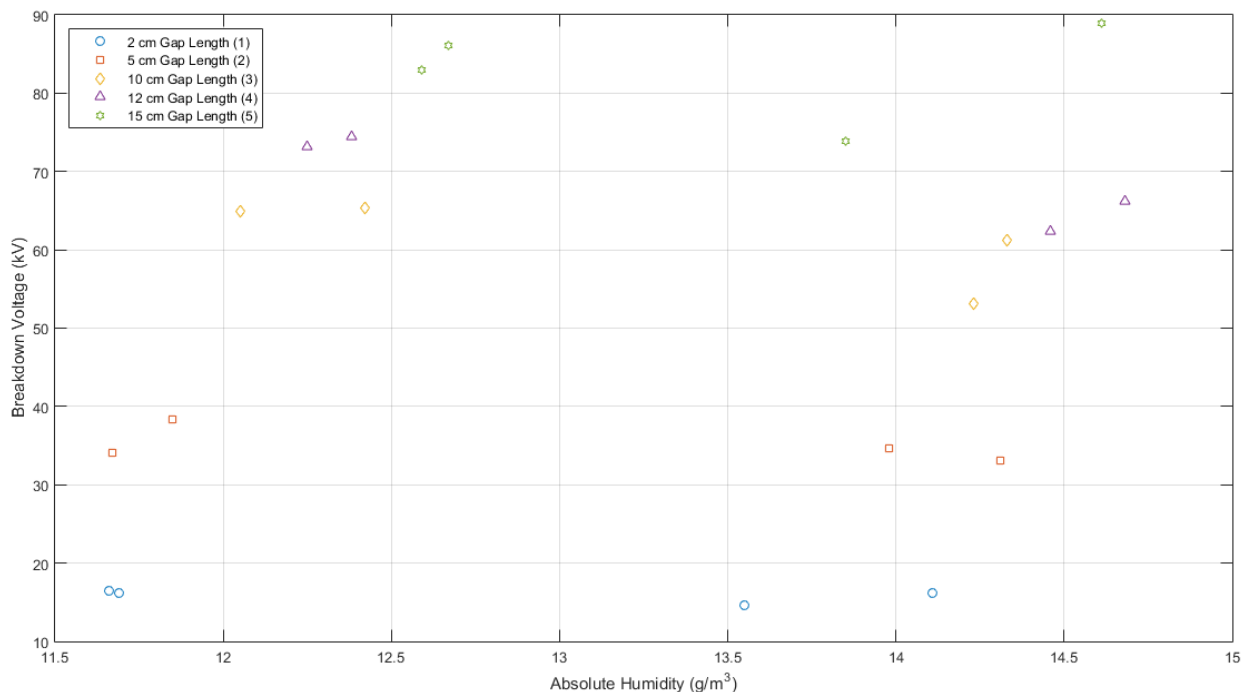


Figure 25 - The variation of breakdown voltage as a function of absolute humidity (g/m³) for electrode gap lengths of 2 cm, 5cm, 10 cm, 12 cm and 15 cm.

For the gap length of 2 cm, it is observed that there is no significant trend between the absolute humidity and breakdown voltage. This could also be a result of atmospheric pressure or temperature influencing the results.

Observing the results obtained for the gaps of 5 cm, 10 cm, and 12 cm gap, it is seen that there is an increase in the breakdown voltage when the absolute humidity is in the range of 12-12.5 g/m³ but as the absolute humidity increased to values greater than 13.8 g/m³, a reduction in the breakdown voltage was experienced. This could be a result of the breakdown developing out of the glow discharge without impulses when a DC voltage was applied as indicated by Fischer [94].

It is seen for the 15 cm gap length that there is an increasing trend in breakdown voltage as the absolute humidity increases. Although there was a reduction in the breakdown voltage when the absolute humidity was 13.85 g/cm³, this could be a result of the atmospheric pressure influencing the result as it was the lowest on that day when compared to the other days the tests were performed. As the atmospheric pressure was less it resulted in the voltage required for breakdown to reduced.

3.2.4 Comparisons of Breakdown Voltage to Pressure

Figure 26 represents the breakdown voltage plotted against the pressure for 2 cm (blue circles), 5 cm (red squares), 10 cm (yellow diamonds), 12 cm (purple triangles) and 15 cm (green hexagons) gap lengths.

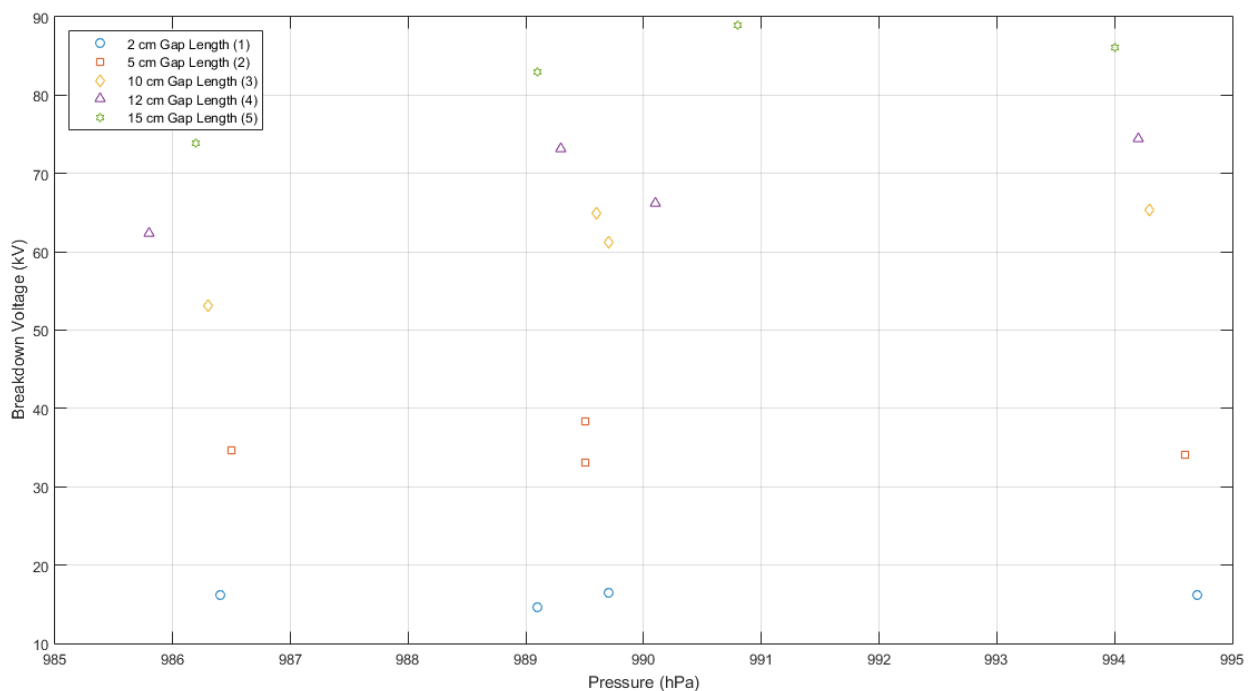


Figure 26 - The variation of breakdown voltage as a function of pressure (hPa) for electrode gap lengths of 2 cm, 5 cm, 10 cm, 12 cm, and 15 cm.

It is observed for the 2 cm and 5 cm air gap that there is no significant trend with the breakdown voltage of the air gap and the pressure. As both 2 cm and 5 cm gap lengths are relatively small gaps, the atmospheric pressure could have been a factor that did not influence the breakdown voltage, or the influence of humidity and temperature could have affected the results more than pressure for these gap lengths.

For the larger gap lengths that are the 10 cm, 12 cm and 15 cm gap lengths, a trend does exist between the breakdown voltage and pressure which is expected. This trend depicts that the breakdown voltage does increase with an increase in pressure. There are deviations from this trend which can be seen in the figure and these deviations are a result of both humidity and temperature having an influence on breakdown voltages.

3.2.5 Comparisons of Breakdown Voltage to Temperature

Figure 27 represents the breakdown voltage plotted against the temperature for 2 cm (blue circles), 5 cm (red squares), 10 cm (yellow diamonds), 12 cm (purple triangles) and 15 cm (green hexagons) gap lengths.

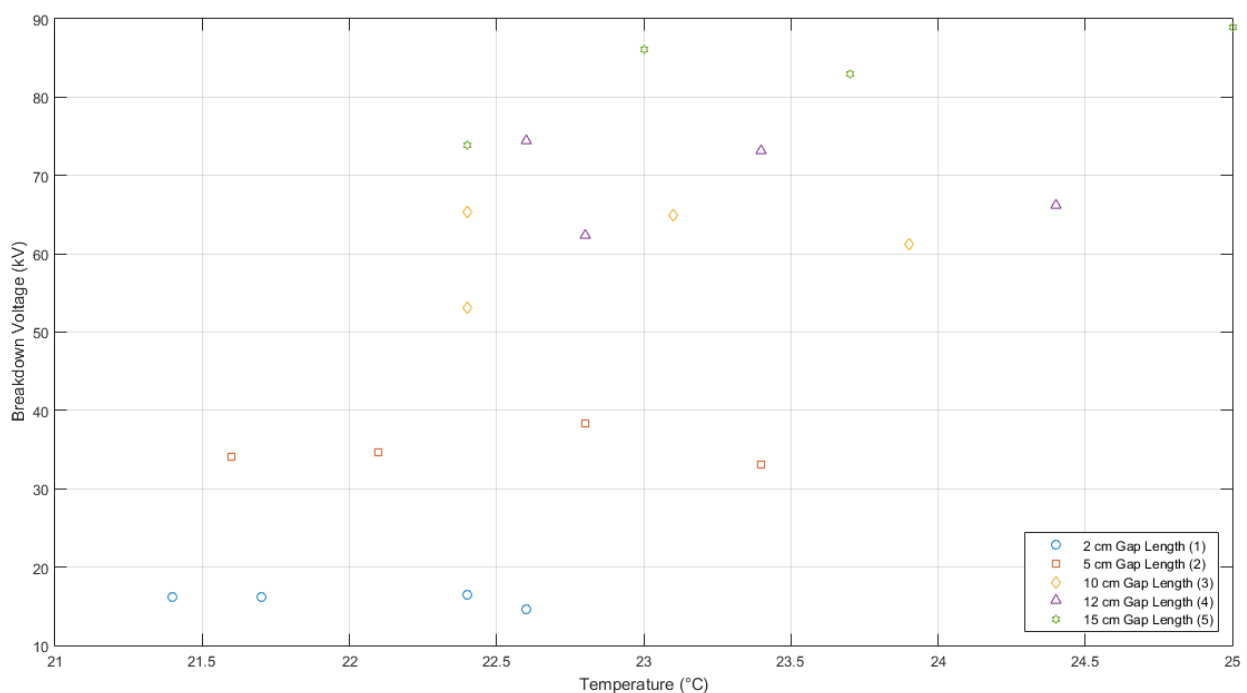


Figure 27 - The variation of breakdown voltage as a function of temperature ($^{\circ}\text{C}$) for electrode gap lengths of 2 cm, 5 cm, 10 cm, 12 cm and 15 cm.

By observing Figure 27, the 2 cm and 5 cm gap lengths does not have a significant trend in breakdown voltage with temperature, but the results obtained from the 10 cm and 12 cm gap lengths showed a decrease in breakdown voltage as the temperature increased. This was expected for the 10 cm and 12 cm gap length. There are slight deviations from the trend, and this may be a result of either humidity or pressure or even both having an influence on the breakdown voltage.

The breakdown voltage can be seen increasing for the 15 cm gap length when plotted against temperature. This could be a result of the distance between the electrodes having a more significant effect on the breakdown voltage than temperature. Once again, humidity and pressure may have also influenced the breakdown voltage of this long air gap.

3.2.6 The Formation of a Positive Streamer Using High Speed Photography

The images captured by the high-speed camera depicting the progress of the streamer in an air gap of length 12 cm is seen by referring to Figure 28. A voltage of 58.74 kV was applied to the needle electrode. The anode is located at the top of the frame and is represented by (a) whilst the cathode is located at the bottom of the frame and is represented by (c).

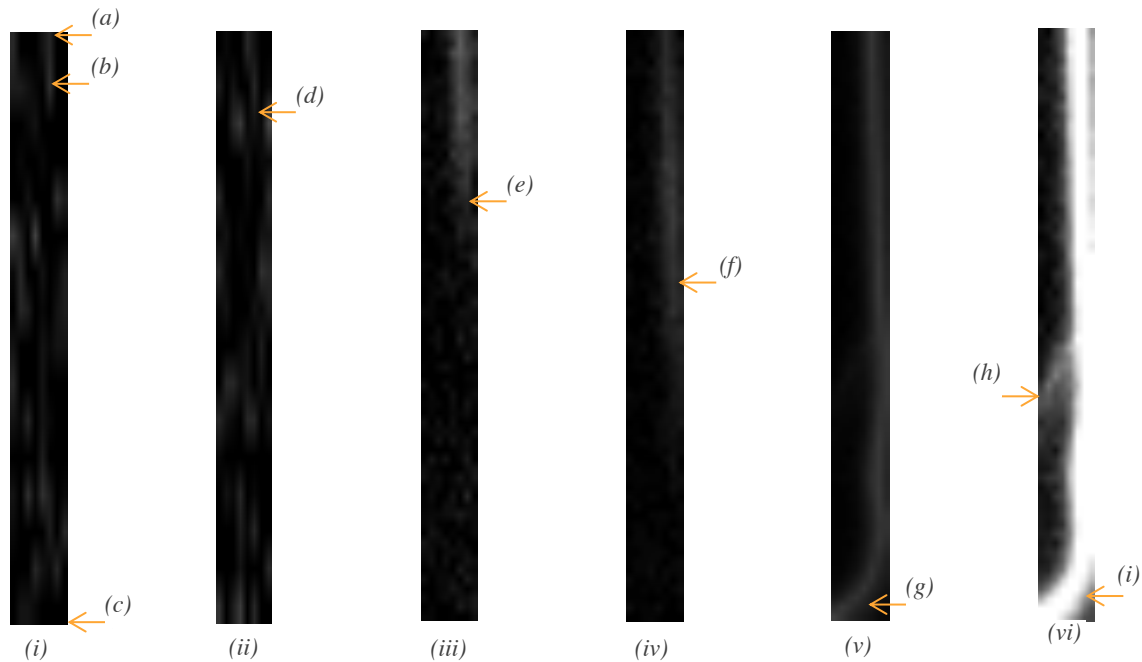


Figure 28 - The initiation and propagation of a cathode directed streamer for a gap length of 12 cm when a voltage of 58.74 kV was applied to the anode. Note that a single streamer occurred. (i) – The initiation of the streamer is seen. (ii) – The extension of streamer. (iii) – A further extension of the streamer from the anode. (iv) – The streamer has extended halfway across the gap. (v) – The primary streamer has progressed and completely crossed the gap. (vi) – Electrical breakdown of the gap had occurred as a bright light had been emitted. A branch from the streamer is seen.

Electrons that are present in a gas at any radial distance from the avalanche axis performs the function of creating more avalanches when in the presence of an externally applied electric field. The avalanches that are created can either be short or long. Photoelectrons are created in the vicinity of the positive ion space charge channel. These positive ions were left behind by the initial avalanche. The electrons located at the anode end are in the presence of an enhanced field that exerts a directive action drawing the electrons into the anode [95].

A conducting plasma that originates from the anode is formed due to the electrons that were created, from the ionization process, being drawn into the positive space charge field. Positive ions that are left behind perform the function of extending the space charge towards the cathode [95]. The creation of streamer corona is seen at (b) in (i) with the streamer stem extending slightly at point (d) in (ii). The electrons that are present are also responsible for the creation of photons that continue this process. This results in the positive space charge developing towards the cathode as a positive space charge streamer. This is represented at (e) in (iii) and (f) in (iv) as the stem is seen extending towards the cathode [95].

The propagation of the streamer towards the cathode results in the production of a filamentary region of intense space charge that is distorted along a line that is parallel to the field. A very steep gradient is produced at the cathode end of the streamer tip by the plasma. The photoelectron avalanches that are produced by radiation occurs at the cathode and it produces an intense ionization near it. The positive ions that are created by this process can influence secondary emission by increasing it. This results in branching from the stem as seen clearly in (h). The fifth frame (v) indicates that the streamer has crossed the gap as seen at (g). A source of visible light occurs because of a cathode spot that was formed by the space charge streamer when it approached the cathode. A conducting filament bridges the gap when the streamer reaches the cathode. Once an efficient cathode spot has occurred, a return electron current proceeds up the streamer channel resulting in electrical breakdown [95]. This is seen in (vi) and is represented at point (i) as a bright source of visible light can be seen and electrical breakdown has occurred in the gap.

The collapse of the applied voltage is seen in Figure 29 at point (a), and this represents that electrical breakdown had occurred in the 12 cm air gap when a voltage of 58.74 kV was applied. The pulses observed before electrical breakdown represent streamers.

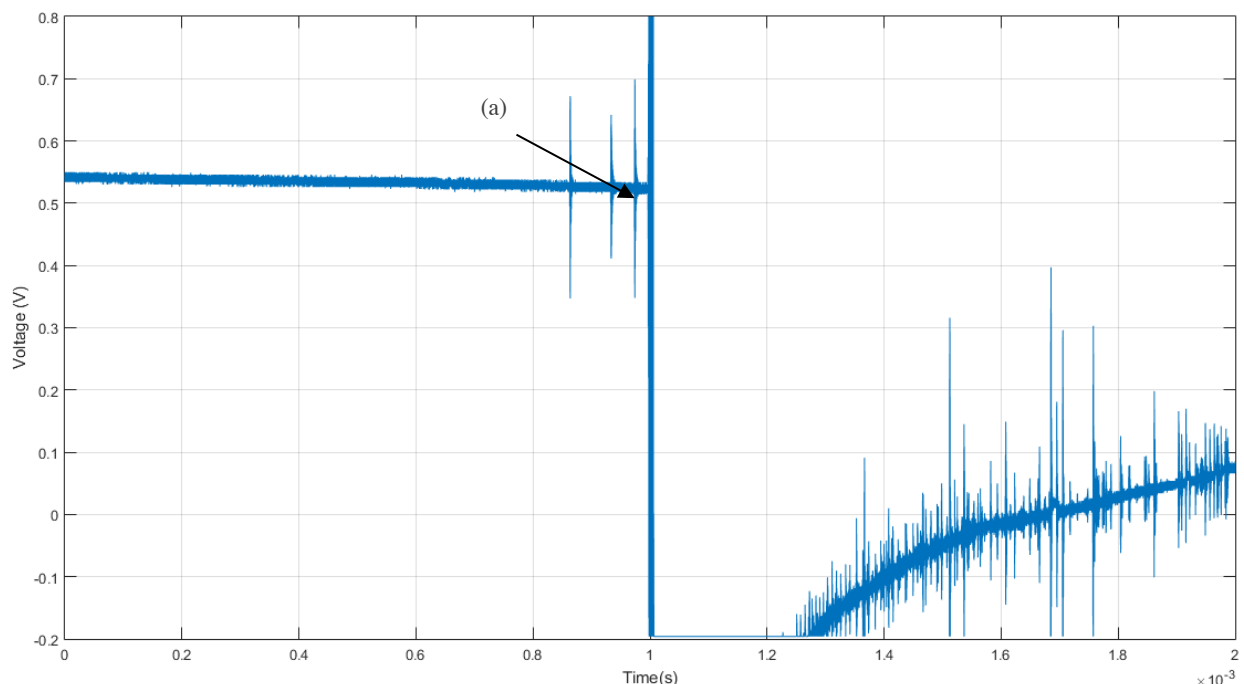


Figure 29 - Electrical breakdown of the 12 cm air gap is seen at point (a). A breakdown voltage of 58.74 kV was applied to anode.

3.2.7 The Influence of Gap Length on the Appearance of Streamers

High-speed photography was conducted for gap lengths greater than 5 cm when the experiment was performed. It was attempted to record the initiation and propagation of the streamer for a 2 cm gap length, but it was not possible as the streamer did not give off enough light that could be recorded by the camera. This also occurred when the electrode distance was set to 5 cm as the initiation of the

streamer from the anode tip could not be seen but streamers that crossed the gap and emitted enough light was able to be recorded by the camera as seen in Figure 30.

3.2.7.1 5 cm Gap Length

Figure 30 below represents the propagation of a streamer in a 5 cm air gap.

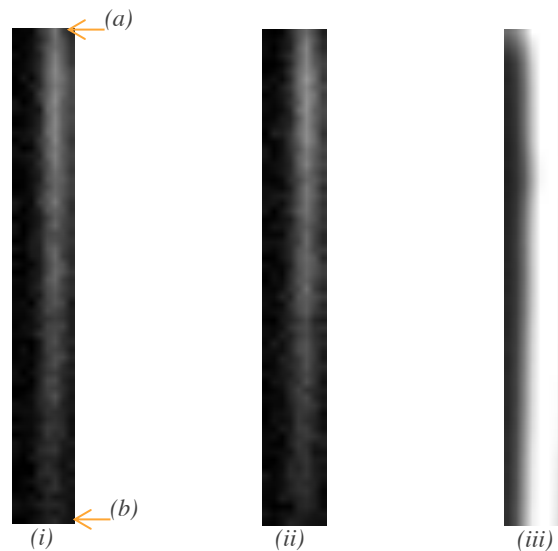


Figure 30 - The propagation of the streamer for a gap length of 5 cm. (i) – The streamer has propagated from the anode towards the cathode. (ii) – The streamer has extended further towards the cathode. (iii) – Electrical breakdown of the air gap.

3.2.7.2 10 cm Gap Length

Figure 31 below represents the initiation and propagation of a streamer in a 10 cm air gap.

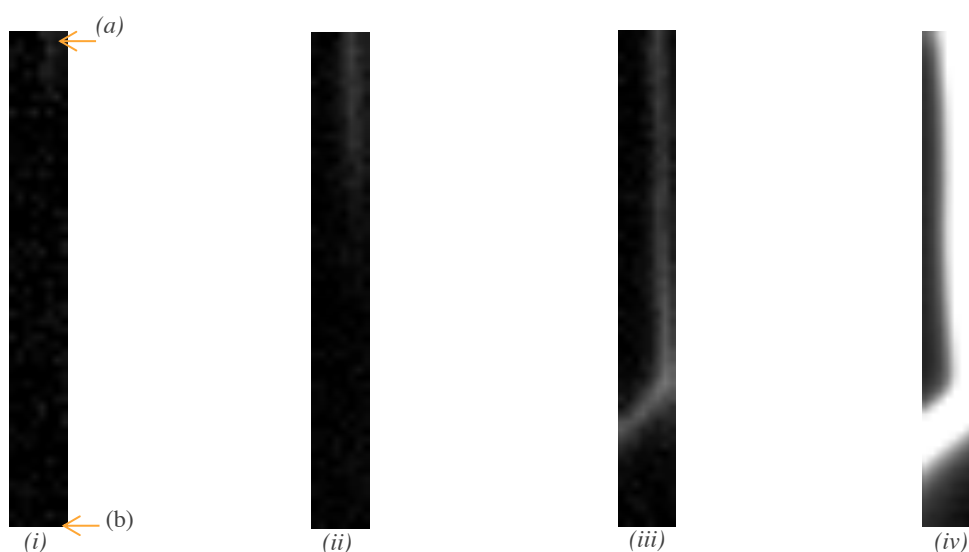


Figure 31 - The propagation of the streamer for a gap length of 10 cm (i) – The initiation of the streamer is seen. (ii) – The extension of streamer from the anode. (iii) – The primary streamer has progressed and completely crossed the gap. (vi) – Electrical breakdown of the gap has occurred as a bright light has been emitted.

3.2.7.3 15 cm Gap Length

Figure 32 below represents the initiation and propagation of a streamer in a 15 cm air gap.

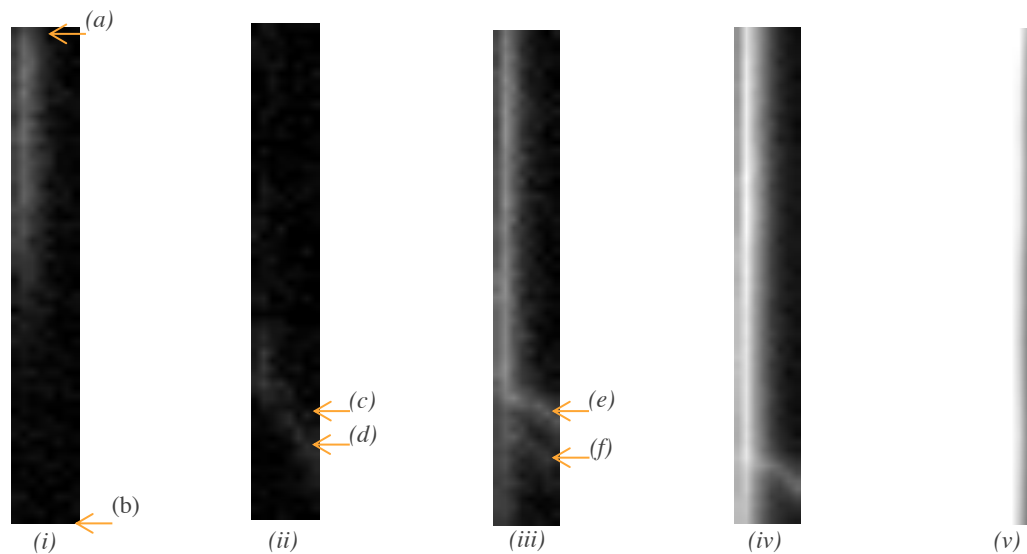


Figure 32 - The initiation and the propagation of a streamer for a gap length of 15 cm. (i) – The extension of the streamer from the anode is seen. (ii) – A further extension of the streamer as well as branches is seen from the streamer. (iii) – The primary streamer has crossed the gap as well as multiple branches is seen. (iv) – An increase in the amount of light emitted by the streamer and the presence of a single branch near the cathode. (v) Electrical breakdown of the gap has occurred as a bright light has been emitted.

Referring to Figures 30, 31, and 32, the anode and cathode are represented by (a) and (b) respectively in these figures. Figure 13 represents the frames that could be captured for a 5 cm gap length. A voltage of 30.94 kV was applied to the anode. The streamer had already crossed the gap and breakdown occurred in frame (iii). A straight streamer occurred for the 5 cm gap length with the absence of any branches when propagating towards the cathode.

Figure 31 represents frames that depict the initiation and propagation of a streamer for a 10 cm gap length. The voltage applied to the anode was 55.03 kV. It is seen in frame (iii) that the stem of the streamer had elongated when compared to Figure 30. It was also observed that the streamer bent its path when it approached the cathode. An explanation is performed in section 3.2.9 to explain the cause of the streamer bending its path when propagating. Frame (iv) depicts the electrical breakdown of the air gap.

Referring to Figure 28 in section 3.2.6, the streamer initiation and progression of it for a 12 cm gap length can be seen. When comparing Figure 28 to Figure 30 and 31, it is seen that as the gap length increased there was an increase in the elongation of the stem. A single branch also appeared at point (h) in the sixth frame of Figure 28 and these branches were not present for the smaller gaps.

Figure 32 represents the propagation of the streamer and the electrical breakdown of an air gap that has a length of 15 cm. The voltage that was applied to the anode was 88.95 kV. Apart from the

increase in the elongation of the stem when the gap length increased, it was also observed that the number of branches that were present had also increased. These branches are seen at points (c) and (d) in frame (ii) as well as in points (e) and (f) in frame (iii).

The secondary streamer mechanism was the breakdown mechanism that was present for all the discharges that occurred in the experiment. The primary streamer crossing the gap is seen in Figures 28, 30, 31, and 32.

For all the gap lengths investigated, it was seen that single streamers occurred, and this is due to the quasiuniform electric field that was created by the needle-plane electrode configuration. This type of electric field results in narrower and direct streamer structures being formed [8, 89]. This type of streamer was expected as indicated by the results obtained by Tarasenko et al. [89].

It was seen that as the gap length increased there was a resulting increase in the length of the stem.

Branches appeared for gap lengths that were equal to or greater than 12 cm with the number of branches increasing as the gap length increased. When analysing the high-speed photographs of air gaps greater than 10 cm, it was observed that streamers would occasionally take a bent path when propagating towards the cathode.

3.2.8 The Influence of Pressure on the Appearance of Streamers

Figure 33 below displays the initiation of a cathode directed streamer from the anode on a day that atmospheric pressure was 994.0 hPa. The distance between the electrodes in the frame below was 15 cm.

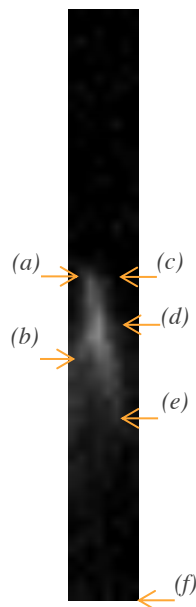


Figure 33 - The initiation of a streamer from the anode when the atmospheric pressure was 994.0 hPa in the laboratory. A voltage of 77.50 kV is applied to the anode and the resulting branches is seen at the anode tip.

Points (a) and (f) in Figure 33 represent the tip of the anode and cathode respectively. A voltage of 77.501 kV is applied to the anode. Referring to point (b), (c), (d) and (e) in the frame, it is seen that a branching structure is observed at the anode tip. Figure 34 represents an illustration of the results obtained by Pancheshnyi et al. [96].

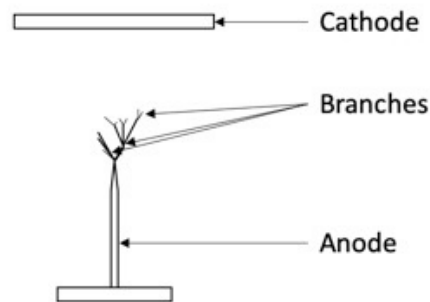


Figure 34 - An illustration of the branching that occurred at the anode tip for a pressure of 906.59 hPa in [96].

It was observed in [96], that the branching of streamers at the anode tip was only observed at pressures greater than 906.59 hPa (680 torr) as seen in Figure 34. This was also observed in Figure 33, as branching occurred at the streamer tip at a pressure that was greater than 906.59 hPa.

3.2.9 The Bent Path a Cathode Directed Streamer Takes

It was observed that streamers would take a bent path when propagating towards the cathode for electrode distances greater or equal to 10 cm. This is seen in Figure 35 below where the electrodes are separated by 15 cm. The high-speed video camera recorded the frame in Figure 35 at a rate of 140 000 frames per second with an exposure time of 6.6 μ s.



Figure 35 - The bent path a streamer takes for a gap length of 15 cm when approaching the cathode.

The bent path a positive streamer takes, when propagating, could be a result of the electron density being increased non simultaneously with different rates in different regions of the discharge volume when it is formed. As a result of this, an electron density gradient at the ionization wavefront is created. This causes the direction of the electric field component to be different from the background electric field resulting in the positive streamer bending when propagating towards the streamer [97].

Streamers choose to follow paths that have increased levels of electron density when propagating but they are also unable to propagate through regions that consist of very high amounts of space charge [97]. It is seen in Figure 36 at point (b) that the streamer is bending its path when approaching the cathode at point (d). This could be a result of excess space charge being present at point (c).

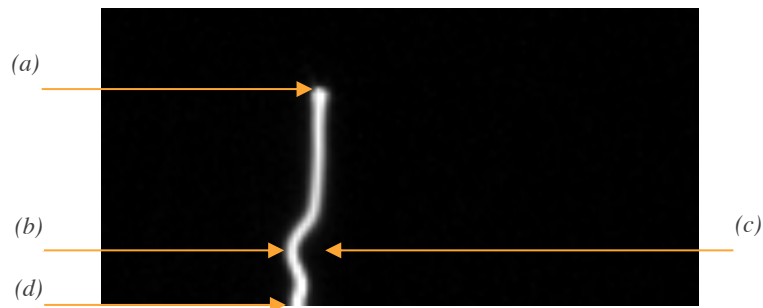


Figure 36 - The bent path a streamer takes when approaching the cathode for a 15 cm gap length. The location of an increased region of space charge is assumed in the frame.

This was apparent in an investigation performed by West [98], as the experiment consisted of applying an impulse voltage (1.2/50 μ s) to a Rogowski profile spark gap. A laser beam that entered the spark gap at 90° was included in the experiment which supplied space charge at a specific point in the gap. It was observed that the HV arc produced bent around the laser-induced plasma when approaching the cathode as seen in Figure 37.

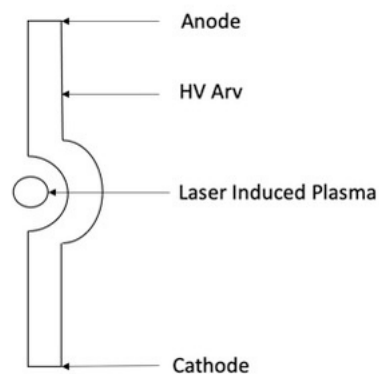


Figure 37 - An illustration of the bent path the HV arc took in the presence of a laser induced plasma in [98].

3.2.9.1 The Analysis of the Electric Field for a Streamer that Takes a Bent Path

Figure 38 represents the results obtained from a FEMM simulation showing the electric field distribution of an air gap. A high voltage was applied to the needle electrode and excess space charge was present in the form of spheres in the air gap. The cathode was grounded in the simulation.

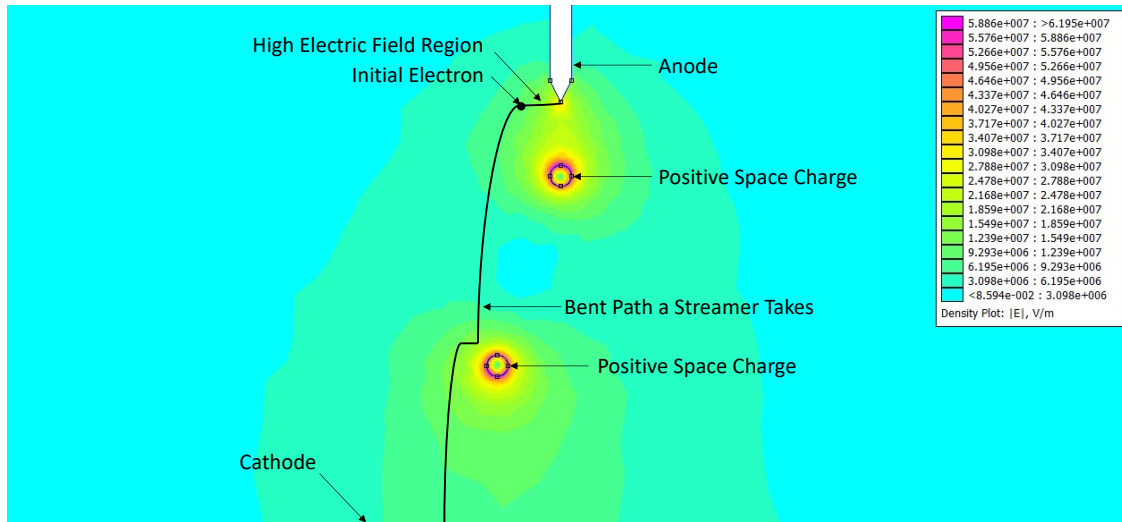


Figure 38 - A FEMM model showing the electric field distribution in an air gap when there is a presence of excess space charge in the form of spheres. The path a streamer may take as a result of space charge being present in the air gap is seen.

As seen in Figure 38, the application of a voltage that is near the breakdown magnitude results in the positive ions that are left behind by previous streamer discharges to be distributed [99]. This is found at points where there are positive space charge spheres present in the figure. It is seen from the FEMM model created that the electric field around the positive space charge sphere is much higher when compared to the magnitude of the electric field that is present at the tip of the anode. Electrons that are present in the gap attach to these positive space charge spheres. Thus, resulting in the positively charged spheres becoming negatively charged.

If there is an initial electron and a high electric field region present near the anode, then a streamer would be initiated, and it would begin to propagate. As seen in the figure, the streamer takes a path that goes around the now negatively charged sphere as it is not able to propagate through regions that have a high concentration of electrons. The streamer is then obligated to propagate through areas that consist of an electric field that is strong enough to continue the collisional ionization and attachment processes. Therefore, it was seen that the presence of space charge influences the path a streamer takes when propagating by bending around it.

3.3 Chapter Summary

The experiment conducted in the laboratory was performed to investigate the streamer breakdown of air gaps that varied in length. The following deductions were made using the results obtained from the experimental procedure:

1. The breakdown voltage of an air gap is directly proportional to the gap length when HVDC was applied to the high voltage electrode.
2. It was observed that the breakdown voltage did not have a significant trend with the absolute humidity for small air gaps and this could have been a result of atmospheric pressure or temperature influencing the results. The breakdown voltage was directly proportional to the absolute humidity for the larger air gaps on days that had similar atmospheric pressure. The results obtained from the experiment showed that the breakdown voltage decreased when the humidity increased. This could have been a result of the breakdown developing out of the glow discharge without impulses when a DC voltage was applied as indicated by Fischer [94].
3. It was observed that the breakdown voltage did not have a significant trend with the atmospheric pressure for small air gaps. This could have been a result of humidity or temperature influencing the results. A significant trend occurred between the atmospheric pressure and the breakdown voltage of air gaps that were greater than or equal to 10 cm as the breakdown voltage shared a directly proportional relationship with the atmospheric pressure.
4. The breakdown voltage shared an indirectly proportional relationship with the atmospheric temperature for all the air gaps except for the 15 cm gap length. This could have been a result of the gap length between the electrodes having a more significant effect on the breakdown voltage than temperature. Humidity or pressure could have also influenced the breakdown voltage.
5. The needle-plane electrode configuration resulted in single, straight streamers being created.
6. The breakdown mechanism that was present for all discharges that occurred in the experiment was the secondary streamer mechanism.
7. The stem of the streamers would increase in length as the gap distance between the electrodes increased.
8. Branches would appear from streamers when the gap length was equal to or greater than 12 cm.
9. It was observed that the streamers branched out at the anode tip when the atmospheric pressure was 994.0 hPa.

10. It was seen that streamers would take a bent path when propagating towards the cathode for gap lengths greater than or equal to 10 cm. This is a result of excess space charge being present in the air gap along its path. As investigated in this dissertation, streamers do not propagate through regions that have a high concentration of space charge therefore causing it to go around the region of excess space charge when propagating towards the cathode.

4 Numerical Simulation of a Cathode Directed Streamer in Air

The numerical simulation of streamers in air has gained a substantial amount of attention in recent times because of its practical uses. For example, the continuous development of insulation technologies that are above 1 MV for both AC and DC power transmission systems. Streamers are precursors of sparks, arcs, and lightning leaders [40]. Therefore, it is used in several applications that involve plasma technology such as surface processing, flow control, environmental applications, sterilization, and disinfection [40].

The simulation of a streamer can be computationally and numerically challenging as it involves steep density gradients and strongly nonlinear coupling with the electric field. Therefore, gaining a significant amount of knowledge and understanding of the physical mechanisms involved in electrical breakdown are essential. It should be noted that the use of computer simulations can be considered a powerful tool for the analysis and prediction of streamer properties [40, 79].

Serdyuk [79], implemented a numerical simulation of a cathode directed streamer in air using COMSOL Multiphysics. Photoionization was implemented in the model to support the propagation of positive streamers in air. Photons that are emitted by the quenching of the excited Nitrogen molecules cause the photoionization of Oxygen molecules at the streamer front. The model performed in [79] did not include the adaptive mesh refinement feature hence mesh refinement was done manually. Although the simulation consisted of acceptable results, it was seen that proper meshing techniques and numerical stability are essential as it ensures that steep gradients are captured at the propagating plasma fronts. A moving frame with a fine mesh and techniques that consist of flux corrections should be implemented to enhance stability.

Ducasse et al. [100], used two methods to model an electro-hydrodynamic streamer. The first method was one that used the Finite-Element Method (FEM) coupled with a Flux-Corrected Transport (FCT) technique. The second was a model that included the Finite-Volume-Method (FVM) with the use of a Monotonic Upwind-Centred Scheme for Conservation-Law (MUSCL) algorithm. A model was implemented with a hyperbolic point-plane electrode configuration, and it had background ionization implemented as a secondary source of electrons instead of using photoionization. It was also stated in [100], that the model which implemented FEM and an unstructured grid approach was computationally expensive and time consuming which required further optimization.

Pancheshnyi et al. [96], performed an experimental and numerical simulation that investigated the characteristics of streamers under various pressures. A 2D hydrodynamic approach was taken with the implementation of photoionization as a source of secondary electrons. The numerical model did not include the emission of electrons from the electrode surface which resulted in the model not adequately describing the discharge when the voltage magnitude decreased in the gap. It was seen in

the experimental results that branching at the anode tip occurred at greater pressures, but the model was only developed for single-channel streamers. The model also underestimated the characteristics of the streamers at lower pressures.

The numerical simulation of a cathode-directed streamer in a 0.1 cm air gap is modelled using COMSOL Multiphysics in this dissertation. This is a software package that is ideal for problems that involve the coupling of Partial Differential Equations (PDE's) that are required to be solved. The version used of the software was COMSOL Multiphysics 5.5 and it uses a time-dependent parallel sparse direct solver (PARDISO). This chapter serves as an introduction to the Plasma interface in COMSOL Multiphysics and highlights the necessary steps that were taken for the implementation and simulation of the numerical model. The results that were obtained from the numerical simulation is included and analysed in this chapter. The numerical model was then used to assist in determining whether humidity and pressure influence the breakdown voltage in an air gap.

It was initially attempted to perform the numerical simulation of a cathode directed streamer for a 2 cm air gap as investigated in the experiment. The cathode directed streamer would initiate but not propagate as the numerical model did not have photoionization included. The geometric model created as well as an elaboration on how the absence of photoionization prevented the propagation of the streamer can be seen in Appendix C.

4.1 Plasma Interface in COMSOL Multiphysics

As stated previously, the Plasma module in COMSOL Multiphysics was used to model the cathode directed streamer. Information on the Plasma module used can be found in [101], [102] and [103]. It performs the function of coupling the Drift Diffusion, Heavy Species Transport and Electrostatics physics into an integrated Multiphysics interface to model plasma discharges.

4.1.1 Drift Diffusion Equations Used for Plasma Modelling

The drift-diffusion/hydrodynamic approach was used to simulate the initiation and propagation of a cathode directed streamer in air. This approach involves the change in densities of electrons as well as both positive and negative ions which are controlled by electrostatic forces in space and time [79, 104]. The electric field influences the convective fluxes of the charged species which is linked to their drift velocities. Diffusive fluxes also occur due to the gradients of carrier densities (∇n) [104].

Three PDE's of a convection-diffusion type are implemented to account for the change in concentrations of these charged particles. This is caused by different mechanisms that affect the generation and reduction rates of the concentration of these particles [79, 104]. The PDE's are expressed in equation 30, 31 and 32. Subscripts e , p and n in the equations below represent electrons, positive ions, and negative ions respectively.

$$\frac{\partial n_e}{\partial t} + \nabla \cdot (-n_e \mu_e \mathbf{E} - D_e \nabla n_e) = R_e \quad (30)$$

$$\frac{\partial n_p}{\partial t} + \nabla \cdot (-n_p \mu_p \mathbf{E} - D_p \nabla n_p) = R_p \quad (31)$$

$$\frac{\partial n_n}{\partial t} + \nabla \cdot (-n_n \mu_n \mathbf{E} - D_n \nabla n_n) = R_n \quad (32)$$

Where:

n : Density of species (m^{-3})

t : Time

μ : Mobility of species ($\text{m}^2/\text{V}\cdot\text{s}$)

\mathbf{E} : The vector of the electric field strength (V/m)

D : Diffusion coefficient of species (m^2/s)

R : The net rate of the generation and loss processes

The set of reactions in equation 30, 31 and 32 includes electron impact ionization, electron impact attachment, the recombination of charge carriers.

Equation 33 is used to express the electron impact ionization rate [79]:

$$R_{ion} = \alpha n_e \mu_e \mathbf{E} \quad (33)$$

Where:

α : Townsend's ionization coefficient (m^{-1})

The rate of attachment of electrons to electronegative molecules such as CO_2 , H_2O and O_2 in air is expressed in equation 34 as [79]:

$$R_{att} = \eta n_e \mu_e \mathbf{E} \quad (34)$$

Where:

η : The attachment coefficient (m^{-1})

The electron-ion recombination rate is expressed in equation 35 as [79]:

$$R_{ep} = \beta_{ep} n_e n_p \quad (35)$$

Where:

β_{ep} : Electron-ion recombination coefficient

Equation 36 is used to express the rate of recombination of positive and negative ions [79]:

$$R_{pn} = \beta_{pn} n_p n_n \quad (36)$$

Where:

β_{pn} : Ion-ion recombination coefficient

Therefore, the net rates for the electrons, positive ions and negative ions in air is expressed in equation 37, 38 and 39 respectively as [79]:

$$R_e = R_{ion} + R_0 - R_{att} - R_{ep} \quad (37)$$

$$R_p = R_{ion} + R_0 - R_{ep} - R_{pn} \quad (38)$$

$$R_n = R_{att} - R_{pn} \quad (39)$$

Where:

R_0 : Natural background ionization rate

As stated previously, the PDE's in equation 30, 31 and 32 are dependent on the electric field. Hence, it is required that the drift diffusion equations implemented are coupled with Poisson's equation. This provides a solution where the distribution of the electric field is influenced by the space charge, and

this is important as it allows for the kinetic coefficients and the rates of these individual processes to be obtained [79]. Poisson's equation is expressed in equation 40 [79, 104]:

$$\nabla(-\epsilon_0\epsilon_r\nabla V) = e(n_p - n_e - n_n) \quad (40)$$

Where:

ϵ_0 : Permittivity of a vacuum

ϵ_r : Relative permittivity

V : Electric potential (V)

e : Electron charge

The electric field is calculated by the software using equation 41.

$$\mathbf{E} = -\nabla V \quad (41)$$

Where:

\mathbf{E} : Vector of the electric field strength (V/m)

Poisson's equation consists of the volume charge density and this changes in space when occupied by a discharge. This may either result in a local field enhancement or the weakening of it which influences the various volumetric sources or sinks of the charged species and their fluxes [104].

Numerical instabilities that occur in a simulation impact the results by causing negative concentrations of charged particles to be obtained. This is prevented by converting the drift diffusion equations (30, 31 and 32) into an equivalent logarithmic form. The advantage of using this function is that the concentration of the species remains positive without the need for additional sources or density capping. The disadvantage of using this approach is that the non-linearity of the problem becomes much greater [104].

The drift-diffusion equations were converted into the logarithmic form for the numerical simulation that was performed in this dissertation. The modified drift-diffusion equations for electrons and both positive and negative ion concentrations can be seen by referring to equations 42, 43, and 44 respectively.

$$\exp(nelog) \frac{\partial nelog}{\partial t} + \nabla \cdot (-\exp(nelog)\mu_e \mathbf{E} - D_e \exp(nelog) \nabla nelog) = R_e \quad (42)$$

$$\exp(nplog) \frac{\partial nplog}{\partial t} + \nabla \cdot (-\exp(nplog)\mu_p \mathbf{E} - D_p \exp(nplog) \nabla nplog) = R_p \quad (43)$$

$$\exp(nnlog) \frac{\partial nnlog}{\partial t} + \nabla \cdot (-\exp(nnlog)\mu_n \mathbf{E} - D_n \exp(nnlog) \nabla nnlog) = R_n \quad (44)$$

Where:

$$nelog = \ln(n_e)$$

$$nplog = \ln(n_p)$$

$$nnlog = \ln(n_n)$$

As indicated by Serdyuk [79], including the process of photoionization in a model is computationally expensive as the rate of the process is calculated using the integral radiation transfer model. Hence, it should be noted that photoionization was excluded from the modelling of the streamer for simplification purposes and background ionization was used as a secondary source of electrons in this dissertation.

4.1.2 Transport Settings

[105] implemented a streamer model of Nitrogen using COMSOL Multiphysics and it used a Mixture Averaged Diffusion Model. This selection allows for the mixture averaged diffusion coefficients to be automatically computed by the software based on data input for each species [101]. This type of diffusion model was selected in the model created in this dissertation.

4.1.3 Transport Mechanisms and Plasma Properties

The transport mechanism that was used in [105] was the migration in the electric field therefore this was selected in the streamer model created in this dissertation.

“Use reduced electron transport properties” was selected in [105], and this is used to specify the electron mobility and diffusivity of the model. This option also requires the neutral number density to be indicated and electron transport properties are calculated from the reduced transport properties using equation 45 [101]:

$$\mu_e = \frac{\mu_{red}}{N_n} \quad (45)$$

Where:

N_n : Neutral number density

The “use reduced electron transport properties” was selected in the modelling of the streamer for this dissertation.

When the “local field approximation” setting is selected, the software assumes that the transport and source coefficients are well parameterized through the reduced electric field. This selection reduces the complexity of the numerical simulation substantially as the mean electron energy is not required to be solved by the software. Therefore, the data involving the relationship between the reduced electric field and the mean electron energy must be included in the model [101]. The “local field approximation” setting was selected in [105], hence it was used in the model created in this dissertation.

4.2 Geometry

Serdyuk [79], Ducasse et al. [100] and Benziada et al. [106] implemented a two-dimensional axisymmetric model to perform their numerical simulation of their various streamers. Two-dimensional axisymmetric models are used to represent a segment of a three-dimensional model and if revolved around a particular axis, it results in the original 3D model being obtained. The use of an axisymmetric model reduces the computation and modelling time required. Hence, a 2D axisymmetric model was created and used for the modelling of the streamer and is seen in Figure 39.

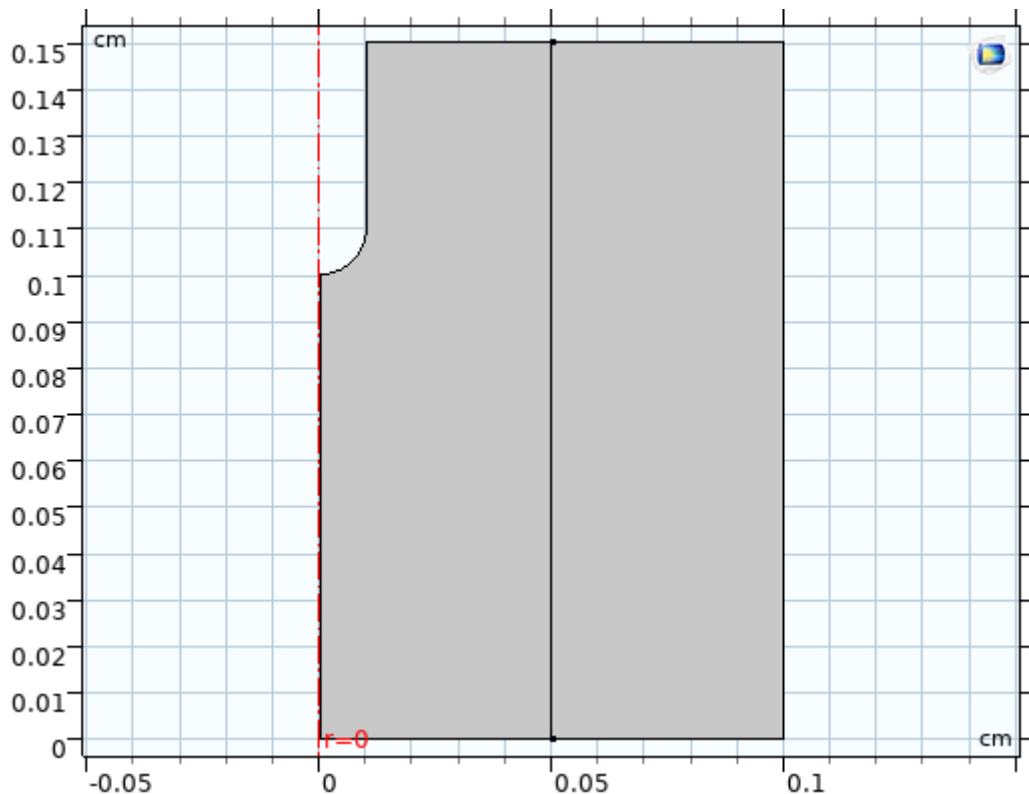


Figure 39 - The geometry of the streamer domain that was implemented in COMSOL Multiphysics.

As seen in the figure, the broken red line that runs vertically from the top to the bottom represents the axis of symmetry. The high voltage electrode (anode) is seen at the leftmost point at the top. The length of the anode in the model is 0.05 cm and the radius of the needle at the tip is 0.01 cm. A grounded electrode (cathode) is placed at the bottom of the model where $r = 0$, and is represented by a single straight line of length 0.1 cm. The length of the gap between the high voltage electrode and the grounded electrode is 0.1 cm. The propagation of the streamer is examined along the axis of symmetry, z -plane, and this is in the direction of the applied electric field.

4.3 Plasma Chemistry

The Heavy Species Transport Interface in the Plasma Module was used to allow for the addition of electron impact reactions, reactions, and surface reactions to the model. Three different types of species are used in the Heavy Species Transport Interface, and these are electrons, anions, and cations. It should be noted that “N₂” is used to represent air molecules in the model created for this dissertation. The reactions that are implemented in this model are used to describe the production and loss processes of the various species that are involved in the electrical discharge.

The letter “e” is used to represent an electron, “N₂” is used to represent a neutral molecule, “N₂⁺” is used to represent a positive ion and “N₂⁻” represents a negative ion in this model.

4.3.1 Electron Impact Reactions

The electron impact reaction node was used to set up the reaction rate for reactions that involve an electron and a specific species. This node requires the user to input the name of the reaction, the collision type, the energy loss if required and the cross-section data or reaction rate [101].

Table 4 below represents the electron impact reactions that were used in model implemented in this dissertation.

Table 4 - The electron impact reactions used in the modelling of the streamer in air on COMSOL Multiphysics.

Reaction	Formula	Type	ΔE (eV)	Townsend Cross Section Data
R₁	$e + N_2 \rightarrow e + e + N_2^+$	Ionization	15.581	Refer to Table 10 in Appendix A
R₂	$e + N_2 \rightarrow N_2^-$	Attachment	0	Refer to Table 10 in Appendix A

The Townsend cross section data for both ionization and attachment coefficients were obtained from the BOLSIG+ simulation results in section 2.7.3. The tabulated values can be seen by referring to Table 10 in Appendix A and the plotted values is seen in Figure 16 in section 2.7.3.

A three-body attachment reaction is included in the modelling of the streamer in this dissertation and the reaction can be seen by referring to Table 5. The reaction rate for the three-body attachment reaction was obtained from [107] which implemented a model on electrical corona in atmospheric air.

Table 5 - The three-body reaction used in the modelling of the streamer in air on COMSOL Multiphysics.

Reaction	Formula	Type	ΔE (eV)	Reaction Rate
R₁	$N_2 + N_2 + e \rightarrow N_2^- + e$	Attachment	0	[107]

4.3.2 Reactions

The reaction node is used so that either a reversible or irreversible reaction is implemented in the model and does not necessarily have to include electrons. The node requires the reaction formula, the reaction type as well as the forward rate constant [101]. The reactions implemented in the model created in this dissertation is seen in Table 6. The forward rate constants were obtained from [107].

Table 6 - The reactions used in the modelling of the streamer in air on COMSOL Multiphysics.

Reaction	Formula	Reaction Type	Forward Rate Constant
R₁	$e + N_2^+ \rightarrow N_2$	Irreversible	[107]
R₂	$N_2^+ + N_2^- \rightarrow N_2 + N_2$	Irreversible	[107]

The surface reaction is used to implement reactions that involve gas phase, surface, and bulk species on surfaces. These reactions are essential when it comes to modelling a discharge as it plays a role in determining the characteristics of it. The reactions involve species that transition from an excited or ionic state to a grounded state [101]. The surface reactions implemented in the model are seen in Table 7.

Table 7 - The surface reactions used in the modelling of the streamer in air on COMSOL Multiphysics.

Reaction	Formula	Electrode	γ_i	Reference	ϵ_i	Reference
R₁	$N_2^+ \rightarrow N_2$	Anode	0	[107]	0	[107]
R₂	$N_2^+ \rightarrow N_2$	Cathode	0.005	[37]	6.581	[101]
R₃	$N_2^- \rightarrow N_2$	Anode and Cathode	0	[107]	0	[107]

Where:

γ_i : Secondary emission coefficient

ϵ_i : Mean energy of secondary electron (V)

As indicated in [101], the mean energy of the secondary electron can be obtained using equation 46:

$$e_i = DE - 2 \times W_f \quad (46)$$

Where:

DE : Ionization energy of the reactant.

W_f : Work function of the cathode surface.

As stated in [108], the work function of iron is 4.5 eV. Therefore, using equation 46, the mean energy of the secondary electron is calculated by using the ionization energy of air (Nitrogen) that was stated in Table 4 and the work function of iron. The mean energy of the secondary electron was calculated and equalled to 6.581 V.

In this model, it is assumed that both anions and cations change back to neutral atoms when interacting with the walls [107].

4.3.3 Electron Mobility and Diffusivity

As explained in the section 4.1.3, the selection of the “Use reduced electron transport properties” requires the electron mobility and diffusivity to be specified. This data was obtained from the BOLSIG+ simulation that was performed in section 2.7.1 and 2.7.2. The tabulated values are seen in Table 10 in Appendix A and the values of both mobility and diffusion are plotted in Figures 14 and 15 respectively in section 2.7.

4.3.4 Reduced Electric Field vs Mean Electron Energy

As explained in section 4.1.3, the selection of the “local field approximation” required the data specifying the relationship between the mean electron energy and the reduced electric field. The data used for the reduced electric and mean electron energy was obtained from the BOLSIG+ simulation performed in section 2.7 and can be seen by referring to Table 10 in Appendix A.

4.4 Initial Conditions

4.4.1 Plasma Cloud

Literature suggests different physical mechanisms of a streamer’s origin [109, 110]. Li et al. [109], performed the initiation of a streamer from an electron avalanche which is present in an overvolted gap. Due to the ionization expanding in the avalanche, it causes shielding charges and streamer formation to commence in the gap [109]. Both Won and Williams [110] and Hallac et al. [37] initiated a streamer from a point of space charge that is located near an electrode with a small curvature radius. As indicated by Yi and Williams [110], this mechanism of initiation fully explains the formation and the growth of single polarity streamers. The placement of space charge, near the anode, increases the speed of the calculation without having an impact on the propagation of the streamer [37, 111]. The second mechanism which used space charge/plasma cloud was implemented in the model created in this dissertation.

An initial plasma cloud is placed 0.001 cm from the tip of the high voltage electrode. This consists of electrons as well as both positive and negative ions. The cloud is of a Gaussian shape and is used to avoid the long formation stage [79]. The initial plasma cloud is represented by equation 47 [81]:

$$\sum_j n_n^-(r, z)|_{t=0} + n_e^-(r, z)|_{t=0} = \sum_i n_p^-(r, z)|_{t=0} = N_{e|t=0} = n_0 \exp \left[-\left(\frac{r}{\sigma}\right)^2 - \left(\frac{(z-z_0)}{\sigma}\right)^2 \right] \quad (47)$$

Where:

$n_n^-(r, z)$: Negative ion density

$n_e^-(r, z)$: Electron ion density

$n_p^-(r, z)$: Positive ion density

z_0 : 0.099 (cm)

Ducasse et al. [100], used an initial density of $n_0 = 1 \times 10^{14} \text{ 1/m}^3$ and $\sigma = 25 \times 10^{-6} \text{ m}$. Both these values were used for the creation of the initial plasma cloud. The initial plasma cloud which includes electrons, positive ions, and negative ions at $t=0 \text{ s}$, is seen by referring to Figure 40.

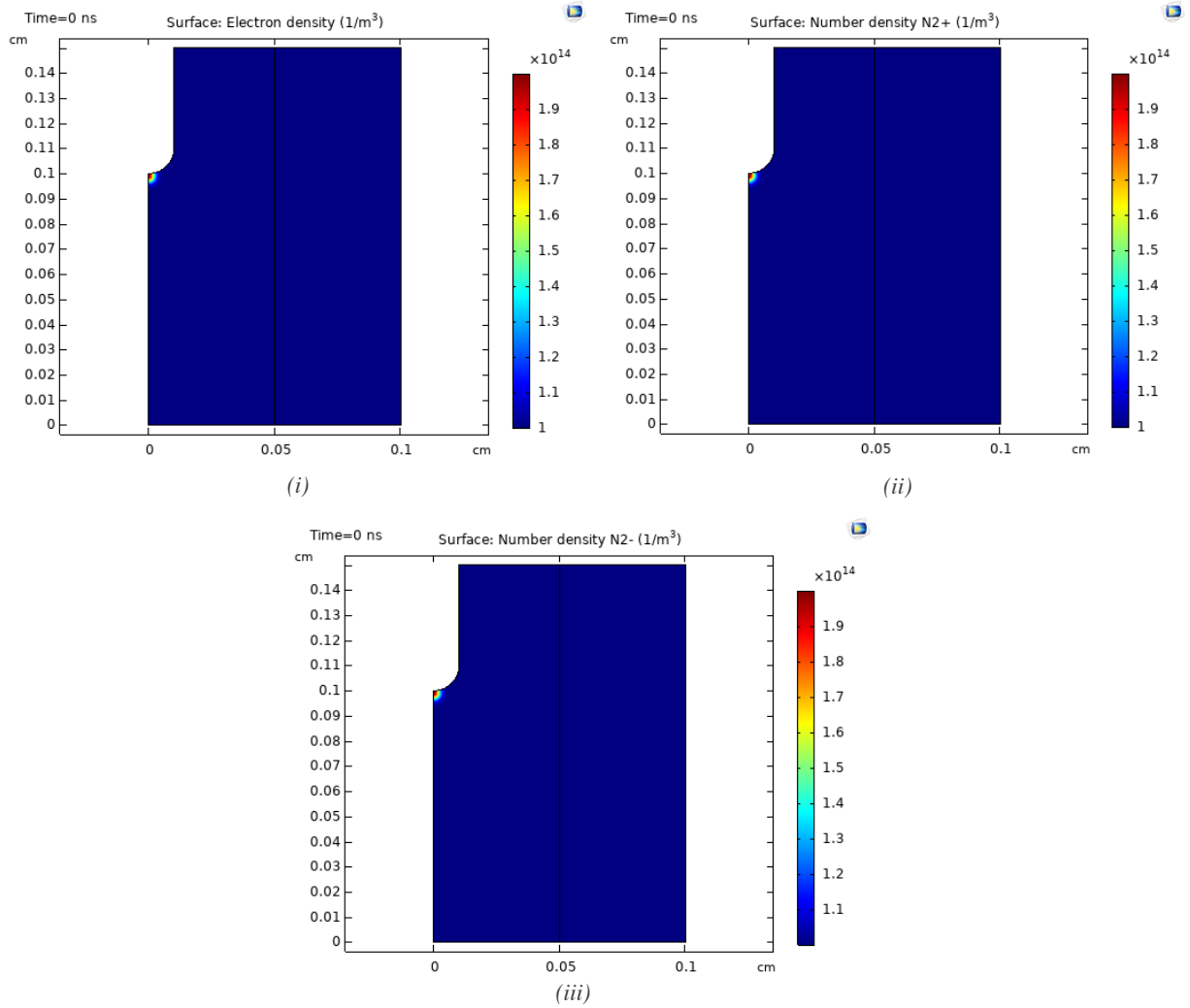


Figure 40 - The initial plasma cloud at $t=0 \text{ s}$ that was implemented in this dissertation for the initiation of the streamer. The Gaussian seed of electrons, positive ions and negative ions is located 0.001 cm from the high voltage electrode. (i) – The initial seed of electrons is seen. (ii) – The initial seed of positive ions is seen. (iii) – The initial seed of negative ions is seen.

The red dots in Figure 40 that are located at $z = 0.099$ cm, represents the seed of electrons, positive ions, and negative ions of Gaussian shape in frame (i), (ii) and (iii) respectively. These seeds have an approximate density of 1.9×10^{14} $1/m^3$. As the plasma cloud consisted of a Gaussian seed of positive ions, it causes a field enhancement to occur at the initial stages of the plasma simulation [40].

4.4.2 Electric Potential

The initial electric potential value is set to 0 V in the model created in this dissertation as it was required to be consistent with the boundary conditions.

4.5 Voltage

Serdyuk [79] and Boakye-Mensah et al. [112] applied a positive DC voltage to their respective electrode when conducting the numerical simulation of the streamer whilst Luque et al. [88], applied both positive and negative DC voltages to the high voltage electrode for conducting their required simulations.

Serdyuk [79], applied a DC positive step voltage that had a rise time of 0.1 ns, and this was implemented in the model created for this dissertation. The step voltage wave is obtained through the step voltage function located under the *Definitions* node. It is a function that is implemented when there is a quick change from 0 to a specific amplitude at any instant of time. It was required that the step function occur at the time of 1×10^{-30} s from the value of 0 which transitions to an amplitude of 1. Both Hallac et al. [37] and Boakye-Mensah et al. [112] investigated the propagation of a streamer in an air with a gap length of 0.1 cm. The voltage that was applied to the anode in both investigations conducted was 3 kV. Therefore, the voltage that was applied to the anode was 3 kV in this model and this was done using the Metal contact option. Figure 41 represents a plot of the voltage vs time showing the magnitude of 3 kV that was applied to the anode in the numerical simulation.

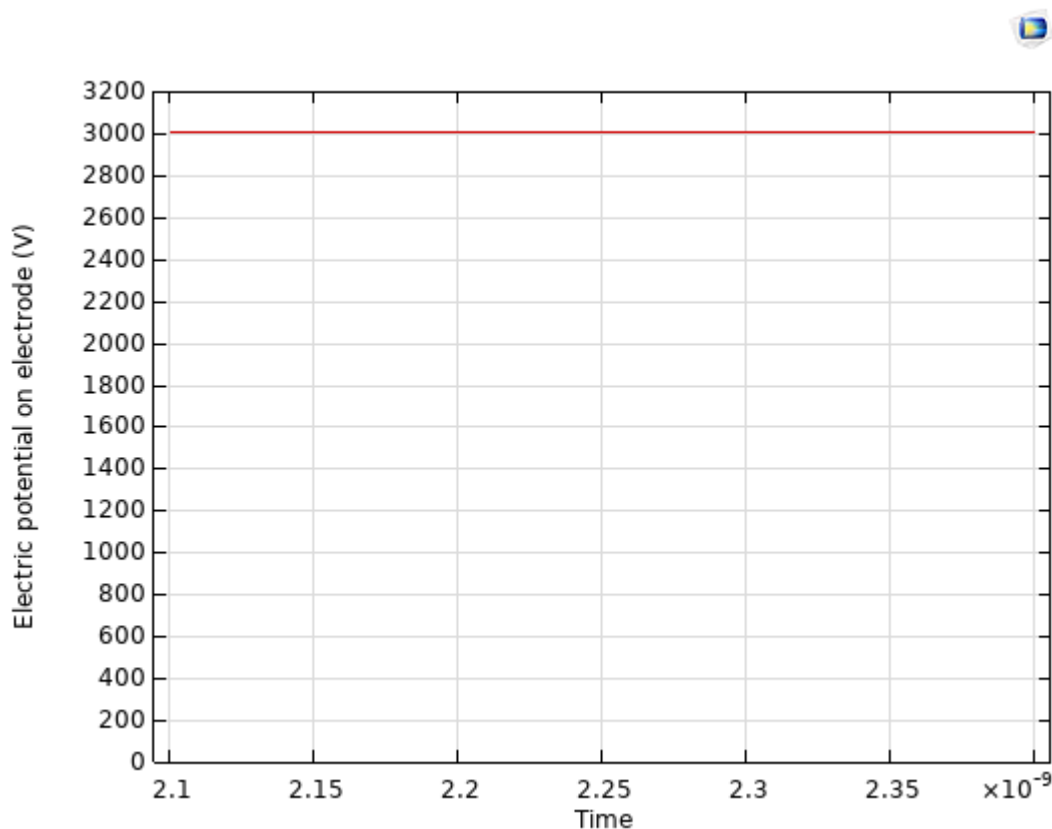


Figure 41 - The step voltage that has a magnitude of 3 kV which is applied to the anode.

4.6 Background Ionization

The Electron Production node located in the Drift Diffusion interface was used to introduce background ionization to the model. The process of background ionization is explained in section 2.4.6. It allows for the addition of sources or sinks to the number density of electrons.

As indicated by Bagheri et al. [40], a positive streamer requires free electrons in the front of it to ensure it propagates. Hallac et al. [37] investigated the effects of a varied background ionization rate and its influence on the streamer propagation. It was seen that when the background ionization rate was too low, it resulted in there being an insufficient number of electrons which prevented the propagation of the streamer. This was a result of the current decaying to a low magnitude and the number of electrons being of a low magnitude once the first avalanche was absorbed by the anode. It was seen that when the background ionization was increased to a magnitude of $10^6 \text{ cm}^{-3}\cdot\text{s}^{-1}$ then the current would increase exponentially, and the streamer would propagate. Further increases in the ionization rate to $10^7 \text{ cm}^{-3}\cdot\text{s}^{-1}$ or $10^8 \text{ cm}^{-3}\cdot\text{s}^{-1}$ resulted in the reduction of the time delay and eliminated the numerical instabilities that occurred when the ionization rate was too low. Bagheri et al. [40], implemented two models that consisted of a constant initial background density of electrons and ions without photoionization. The first and second case in [40] had background ionization rates of $10^{13} \text{ m}^{-3}\cdot\text{s}^{-1}$ and $10^9 \text{ m}^{-3}\cdot\text{s}^{-1}$ respectively. It was seen from the results that a lower background ionization rate in the second case, caused the creation of much steeper gradients in the ionization front thus making it computationally challenging.

The use of a high background field electron density results in the creation of smooth gradients for the electron and ion density as well as allows for the reduction of the electric field at the streamer tip. This ultimately results in a reduction in the number of numerical computations done by the software and machine [40]. For the modelling of the streamer in air in this dissertation, a background ionization rate of $10^8 \text{ cm}^{-3}\cdot\text{s}^{-1}$ was used for the initiation and propagation of the streamer as used in [37].

4.7 Meshing

As indicated by Serdyuk [79], an important part of streamer modelling is the implementation of meshing in the computational domain. The separation of charges that occur in a streamer head has a very thin layer of thickness which is in the order of tens of micrometres [79]. Thus, an extremely fine mesh was required to compute this thin layer and the mesh must have the ability to follow the propagating front. The software divides the CAD geometry into several elements which then makes it possible for equations to be written describing the solution to the governing equation. Another function of the mesh is that it is used to represent the solution field of the physics that is being solved [113].

The use of an Adaptive Mesh Refinement (AMR) tool with the time dependent solver is essential to perform such a function. Bagheri et al. [40], Boakye-Mensah et al. [112] and Pancheshnyi et al. [114] implemented AMR in their respective models for the propagation of their streamers hence it was included in the model created for this dissertation. According to Bagheri et al. [40], the advantage of using AMR is that it allows for the thin space charge layer around the streamer head and in regions where the electric field is high to be resolved whilst keeping the computational cost of the numerical simulation low.

COMSOL Multiphysics uses AMR by first solving an initial mesh and then it continuously inserts elements into regions of the model where the error estimation is high and then resolve the model. This process is done continuously for as many iterations required. Triangular elements are used for 2D models [113]. There is a reduction in the overall error experienced as the software continuously improves the mesh [115].

The use of a fine mesh causes a substantial increase in the number of elements. It results in a finer resolution in the results graphs but also increases the duration of the simulation [116]. Numerical instabilities were observed in the results when the element sizes were set to values that are too large for modelling plasma physics as seen in Appendix C. Both minimum and maximum element sizes were obtained from [40]. The curvature factor was set to 0.05 as there is a curved boundary by the high voltage electrode and this created a smaller mesh element around the curved boundary [117]. A summary of the grid settings used to create the mesh in the domain for this model is seen by referring to Table 8.

Table 8 - The settings used to create the ideally sized mesh that is used for the numerical modelling of a streamer.

	Domain	Reference
Adaptive Mesh Refinement	Included	
Minimum Element Size	2 μm	[40]
Maximum Element Size	8 μm	[40]
Maximum Element Growth Rate	1.1	
Curvature factor	0.05	
Run Time	125 minutes	

The complete mesh when built consisted of 57 723 domain elements and 825 boundary elements. The mesh that was used in the modelling of the streamer breakdown in air is seen by referring to Figure 42. Frame (i) in Figure 42 shows the extremely fine mesh that was created in COMSOL Multiphysics whilst frame (ii) is a magnified frame of the mesh showing the triangles that were created.

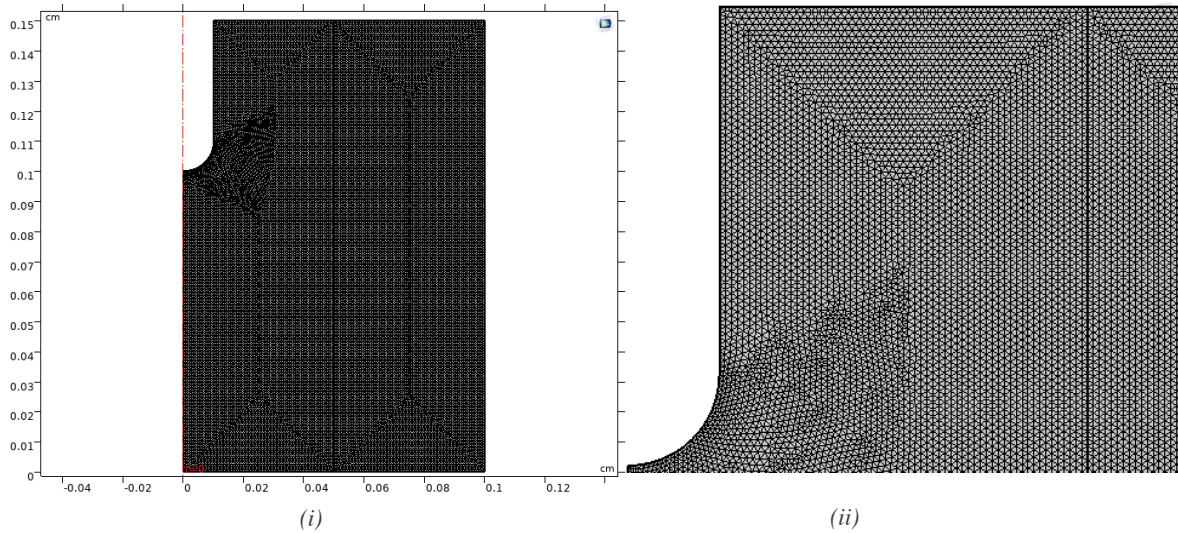


Figure 42 - The mesh created on COMSOL Multiphysics which consists of triangular elements sized between $2 \mu\text{m}$ and $8 \mu\text{m}$. (i) – The extremely fine mesh created throughout the entire domain. (ii) – A magnified portion of the domain showing the triangular elements.

4.8 Study Settings

The inclusion of the *Study node* in the model on COMSOL Multiphysics allows for a solution to be computed and it performs this by implementing study steps in the model. The node allows for the customization of the solver. A time-dependent study step was implemented for the numerical simulation of the cathode-directed streamer. The study step performs the function of controlling the form of equations, selecting the physics that are included in the computation, and selecting the mesh that is used [118].

The *Time-Dependent sub node* allows for the specification of the time unit, time range and the relative tolerance. The relative tolerance is used to control the error in each integration step. As stated by Nijdam et al. [41], streamers that are propagating in atmospheric conditions occur in either a nanosecond or microsecond time scale. Hence, a nanosecond time unit was selected for the model created in this dissertation. The time range for the streamer propagation was set 0-2.4 ns with increments of 0.3 ns. Bagheri et al. [40], performed the numerical simulation of the streamer using a relative tolerance of 0.001 and this was also implemented in the model created in this dissertation. The sub node also included the option of implementing AMR in the model and this was enabled.

Backward Differentiation Formulas (BDF) are implemented with different orders of accuracy for the time stepping method. BDF's are implemented as they are noted for being stable, but it is also commonly used for introducing damping into the solution for lower-order methods. Damping effects are beneficial as it introduces smoothness where sharp gradients occur [116]. Boakye-Mensah et al. [112], implemented a BDF formula of order 1 – 5 and this was also implemented in the model created in this dissertation.

4.9 Results of Simulation

The results of the numerical simulation of a cathode-directed streamer in a 0.1 cm air gap are presented in this section. An analysis was performed on the results obtained. The simulation was conducted on a machine that had a 2.4 GHz Intel Core i9 processor with 32 GB Random Access Memory (RAM) using Microsoft Windows 10. The input parameters and variables which were implemented are elaborated on in section 4.9.1.

4.9.1 Parameters and Variables Implemented

Parameters and variables were both required in the model. Initializing and setting the parameters were done in the Parameters sub-node and they are either specified by the user or the software. Variables were initialised in the variables sub-node and are quantities that are specified by the user. Both the parameters and variables that are implemented in the model are seen in Table 9.

Parameters T and p are used to represent the temperature and pressure of the system respectively.

The geometric parameter d is used to define the distance separating the anode and cathode.

The initial electron, positive and negative ion density concentrations as discussed in section 4.4.1 was created using variables. z0 was the geometric variable that was used to represent the z co-ordinate used for the placement of the initial plasma cloud whilst sigma was the used to define the curvature radius of the cloud. ne0max was used to define the initial density for the plasma cloud.

The parameters that were used for the reactions in the model were rei and rnp. The term rei was used to define the electron-ion recombination rate whilst rnp was implemented to set the ion-ion recombination rate.

The secondary emission coefficient and the mean energy of the secondary electron parameters that were used for the surface reactions were represented using γ_1 and ϵ_1 respectively.

minElem was the parameter used to set the minimum triangular element size whilst maxElem was implemented to set the maximum triangular element size for the mesh. The magnitude of the growth rates for the elements was defined by elemGR and curvFact was used to represent the curvature factor for the mesh.

stepVolt is the variable that was implemented to call the step function used for applying the voltage to the electrode. V0 is the parameter used to define the magnitude of voltage that is applied to the anode.

Re is introduced to represent the background ionization rate as discussed in section 4.6.

Table 9 - List of parameters and variables used to model the cathode directed streamer for this dissertation.

Symbol	Value	Parameter	Reference
T	300 K	Gas temperature	[81]
p	1 atm	Absolute pressure	[81]
d	0.1 cm	Electrode spacing	
z0	0.099 m	Co-ordinates of initial charge distribution	[100]
sigma	25×10^{-6} m	Curvature radius of cloud	[100]
ne0max	1×10^{14} 1/m ³	Initial density	[100]
rei	5×10^{-14} m ³ /s	Electron-ion recombination	[107]
rnp	2×10^{-12} m ³ /s	Ion-ion recombination	[107]
γ_i	0.005	Secondary emission coefficient	[37]
ε_i	6.581	Mean energy of secondary electron	[101]
minElem	2 mm	Minimum element size	[40]
maxElem	8 mm	Maximum element size	[40]
elemGR	1.1	Maximum element growth rate	
curvFact	0.05	Curvature factor	
stepVolt	step1(t)	Step voltage function	
V0	3 kV	Applied voltage	[37]
Re	10^8 cm ⁻³ ·s ⁻¹	Electron production rate	[37]

4.9.2 Electron Density

Figure 43 is used to show the development of a streamer that is propagating in air. It is seen from the 2D surface plots of the electron density that there are concentrations of electrons moving towards the cathode.

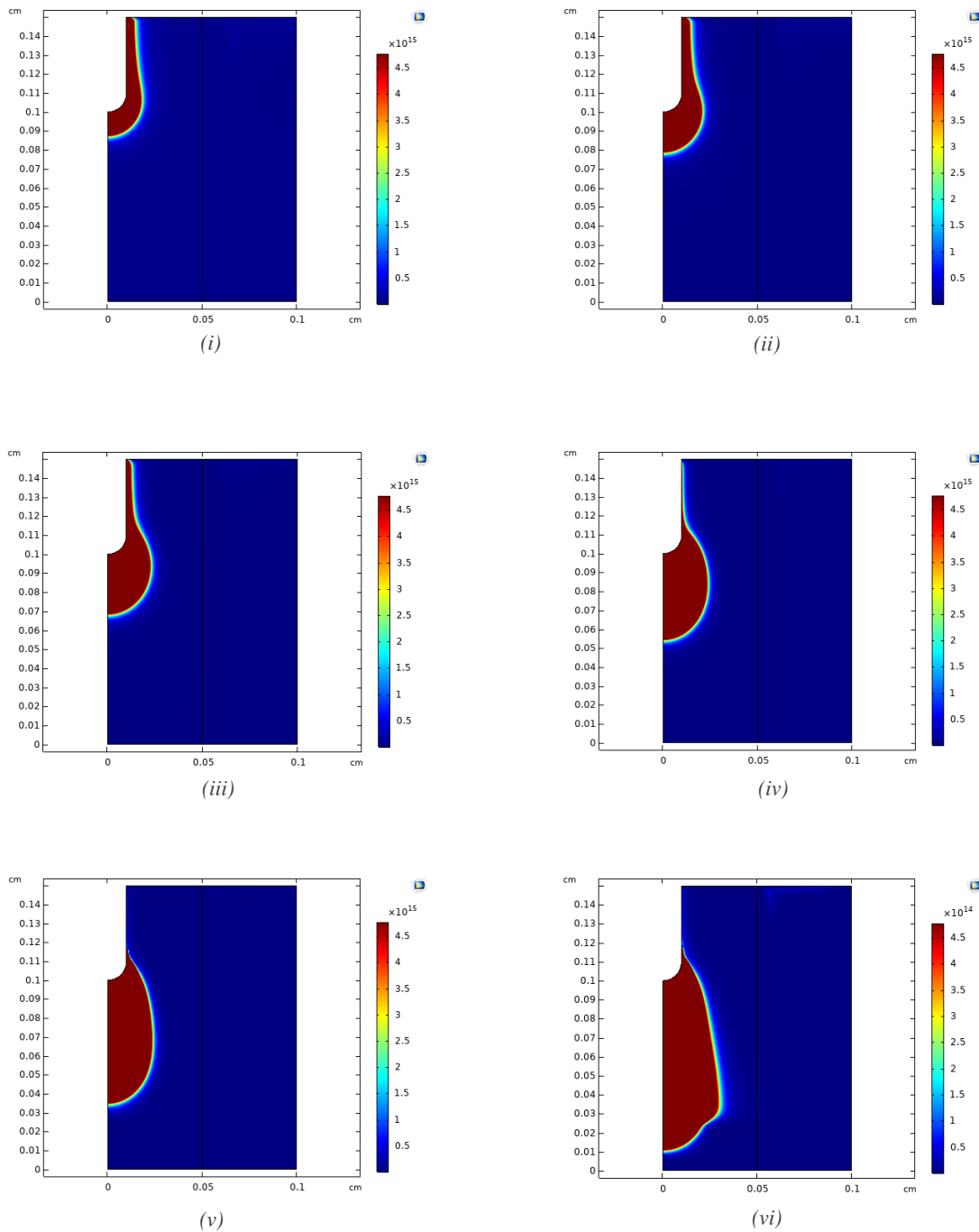


Figure 43 - The 2D surface plots of the electron density for the initiation and the propagation of a streamer in a 1 mm air gap. (i) - $t = 0.3$ ns. (ii) - $t = 0.6$ ns. (iii) - $t = 1$ ns. (iv) - $t = 1.5$ ns. (v) - $t = 2$ ns. (vi) - $t = 2.4$ ns.

Figure 43 shows the time variations of the electron density that was calculated by the software. The electron density is plotted for 0.3 ns (i), 0.6 ns (ii), 1 ns (iii), 1.5 ns (iv), 2 (v), and 2.4 ns (vi). As seen in the figure, the two main stages of the streamer initiation and propagation mechanism are present. These stages are the initiation and radial expansion phase as well as the propagation phase [112].

The applied voltage produced an electric field that resulted in the seed of electrons being absorbed into the anode thus leaving positive charge behind which initiated the streamer. There is an increase in the electron density which is seen in frame (ii) due to the ionization of species when the electrons moved to the anode. The time taken for the initiation of the streamer to take place was 0.3 ns. As seen in frame (ii) and (iii), the electron density grew into a sphere around the tip of the anode and as time progresses the electronic cloud expanded and propagated towards the cathode. This is seen in frames (iv) and (v). The expansion of the streamer and propagation of it, is caused by the generation of electrons at the head of the streamer.

It seen that in frame (vi), the electron density does not meet the cathode, as electrical breakdown had occurred. This is seen by observing the electric field in frame (vi) in Figure 45 and resulted in the streamer increasing in width. The time taken for the propagation of the streamer was 2.1 ns therefore the time that was required for the streamer to initiate and propagate through the entire air gap was 2.4 ns. The time taken for the streamer to initiate and propagate in [112] was 5 ns for the 1 mm air gap. Comparing it to the streamer modelled in this dissertation, the time duration of the model created in this dissertation is shorter, and this could be attributed to the increased strength of the enhanced electric field in this model when compared to the results in [112]. The estimated average front velocity of the streamer was calculated and equalled ~ 0.42 mm/ns. As stated in [112], the propagation velocity of short streamers is in the range of 10^5 and 10^7 m·s⁻¹. The streamer that was modelled in this dissertation had a velocity of 4.17×10^5 m·s⁻¹. Therefore, the velocity of the streamer is in the required range.

The line diagram in Figure 44 shows the distribution of the electron density along the axis of symmetry.

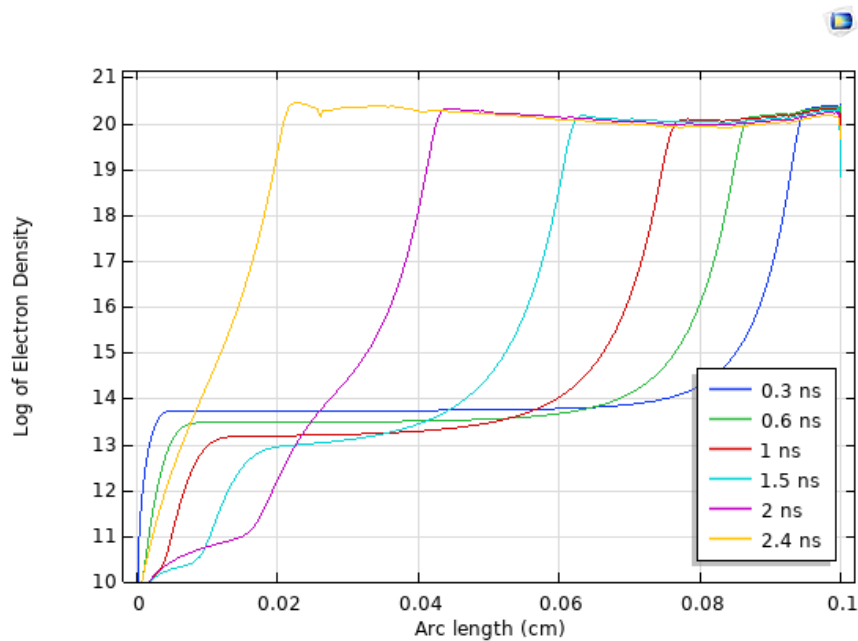


Figure 44 - A line graph showing the variation of the log of the electron density on the streamer axis for different time steps.

It is seen in the line graph in Figure 44 that the density of electrons remains almost constant throughout the streamer channel which is expected. As the streamer approaches the cathode, there is a subtle increase in the density of electrons. It can also be seen in the line diagram that the magnitude of the electron density concentrations is in the range of 10^{19} - 10^{20} m^{-3} which corresponds to an ionization degree of 10^{-5} - 10^{-4} . This is expected for streamer discharges [79, 112].

4.9.3 Electric Field Distribution

Figure 45 is used to show the distribution of the electric field for the streamer propagating in air for time intervals of 0.3 ns (i), 0.6 ns (ii), 1 ns (iii), 1.5 ns (iv), 2 ns (v) and 2.4 ns (vi). The 2D surface plots of the electric field correspond to the 2D surface plots of the electron densities in Figure 43.

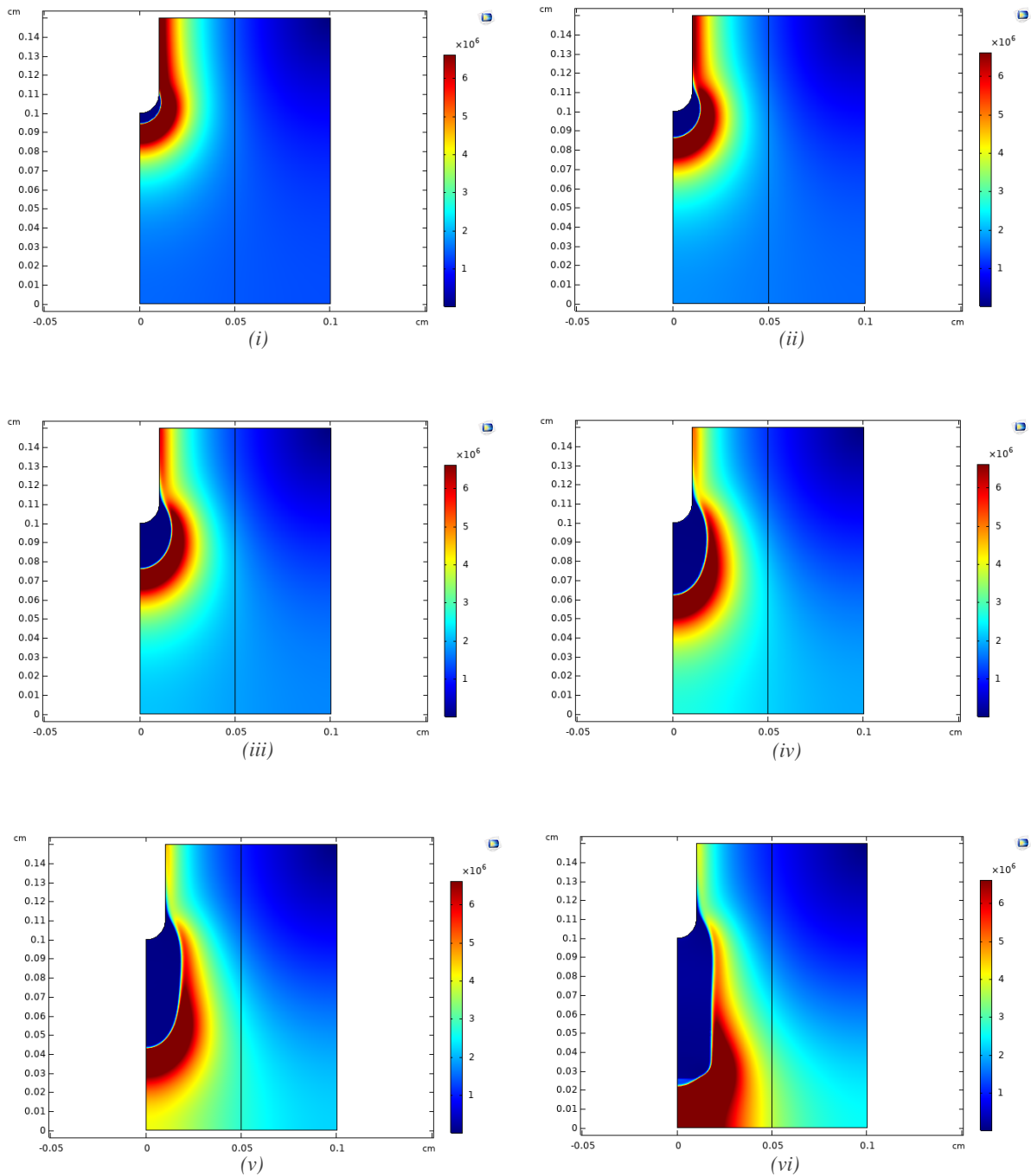


Figure 45 - The 2D surface plots of the electric field for the cathode directed streamer that propagates in a 1 mm air gap. (i) - $t = 0.3$ ns. (ii) - $t = 0.6$ ns. (iii) - $t = 1$ ns. (iv) - $t = 1.5$ ns. (v) - $t = 2$ ns. (vi) - $t = 2.5$ ns.

The evolution of the cathode directed streamer is seen in Figure 45 and it is observed that the enhanced field region is propagating at the streamer tip. The dark blue region in the streamer channel consists of an electric field that has an approximate magnitude of 1×10^6 V/m whilst the streamer channel is shielded by the enhanced electric field that has a maximum magnitude of 6×10^6 V/m. The electron density in the red region of the streamer channel in Figure 43 has an electron density concentration that is in the region of 10^{19} m^{-3} , and this corresponds to the dark blue region in Figure 45. Referring to Figure 45, the initiation of the streamer is seen in frame (i) and the propagation of it is seen in frames (ii), (iii), (iv) and (v). It is also seen in frame (vi) that breakdown has occurred as the enhanced region of the electric field reaches the cathode.

Figure 46 represents the line diagram which shows the distribution of the electric field, and it corresponds to the electron density profiles which is seen by referring to Figure 43.

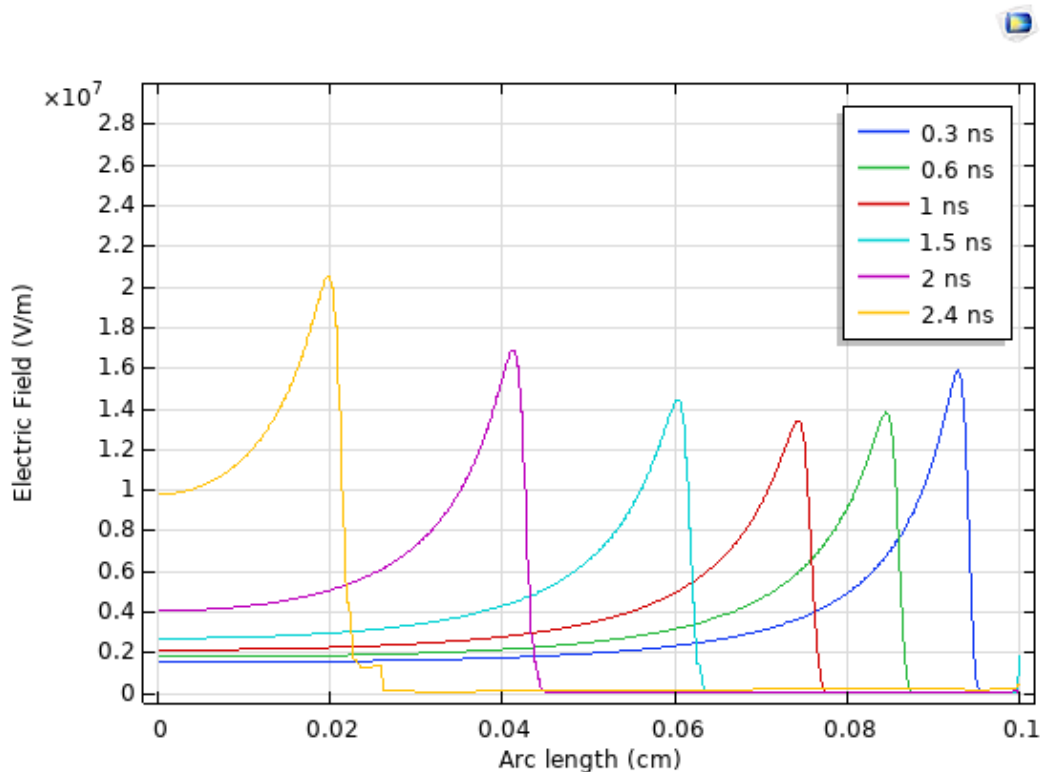


Figure 46 - The variation of the electric field on the streamer axis for different time steps.

Observing the results, the magnitude of the electric field at the head of the streamer ranges between 1.35×10^7 V/m and 1.7×10^7 V/m. It is seen that at 2.4 ns there was an increase in the magnitude of the electric field, and this is attributed to the interaction between the streamer channel, which has a specific potential, and the grounded plane [79, 112].

4.9.4 Electric Potential

Figure 47 shows the 2D surface plots of the electric potential for the cathode directed streamer for time intervals of 0.3 ns (i), 0.6 ns (ii), 1 ns (iii), 1.5 ns (iv), 2 ns (v) and 2.4 ns (vi). The dark blue regions in all 6 frames represent an electric potential of 0 kV whilst the red regions represent an electric potential of 3 kV. It is seen that the electric potential is moving away from the anode in frame (i) and as time progressed it propagated further away from the anode. This is seen in frames (ii), (iii), (iv) and (v). The collapse of the applied voltage occurs in frame (vi), and this corresponds to the enhanced electric field region reaching the cathode as seen in Figure 45.

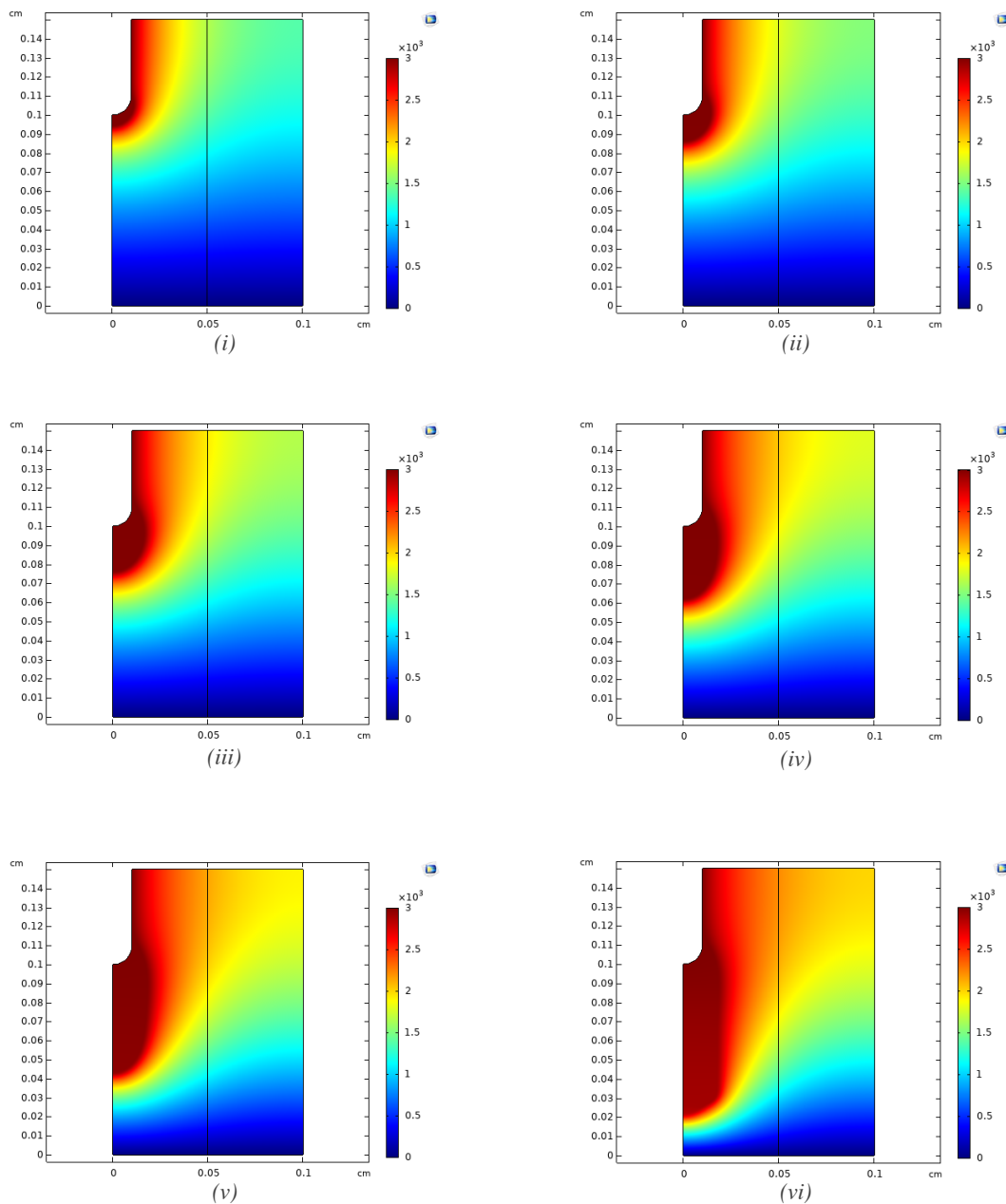


Figure 47 - The 2D surface plots of the electric potential for the cathode directed streamer that propagates in a 1 mm air gap. (i) - $t = 0.3$ ns. (ii) - $t = 0.6$ ns. (iii) - $t = 1$ ns. (iv) - $t = 1.5$ ns. (v) - $t = 2$ ns. (vi) - $t = 2.5$ ns.

4.9.5 Electric Current

Figure 48 is a plot that represents the magnitude of electric current at the anode when the streamer propagated in air for time intervals of 0 ns, 0.3 ns, 0.6 ns, 1 ns, 1.5 ns, 2 ns and 2.4 ns.

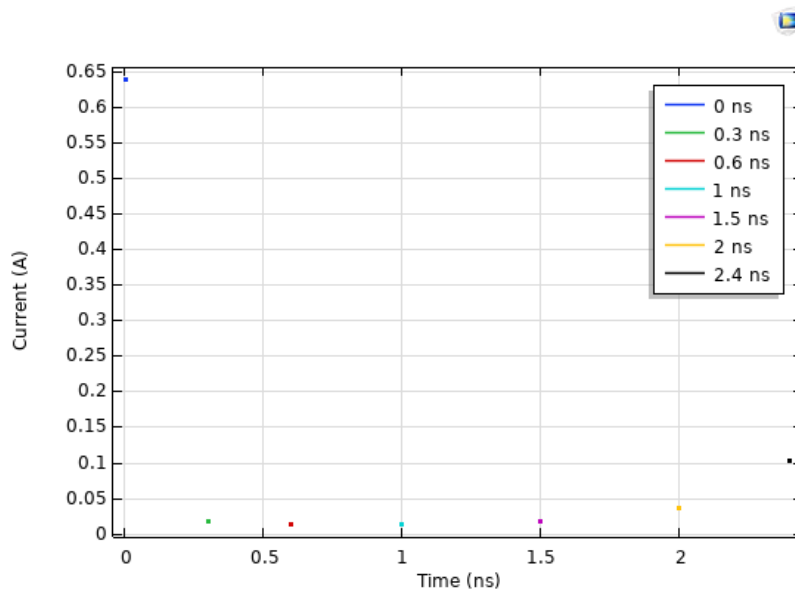


Figure 48 - Plot indicating the magnitude of electric current at the anode tip at different times.

As seen in Figure 48, the magnitude of the current at 0 ns is approximately 0.64 A and drops to a magnitude of 0.03 A at 0.3 ns. The current then remains in the range of 0.01 A and 0.1 A as time progresses. As stated in [41], typical streamer currents are in the order of 1 A or less and this is evident in the model created in this dissertation.

4.9.6 Mean Electron Energy

Streamer discharges are crucially influenced by electron impact reactions. The rate of these reactions is dependent on the mean electron energy [81]. Figure 49 shows the results of the electron mean energy profile of the streamer propagating in air for time intervals of 0.3 ns (i), 0.6 ns (ii), 1 ns (iii), 1.5 ns (iv), 2 ns (v) and 2.4 ns (vi).

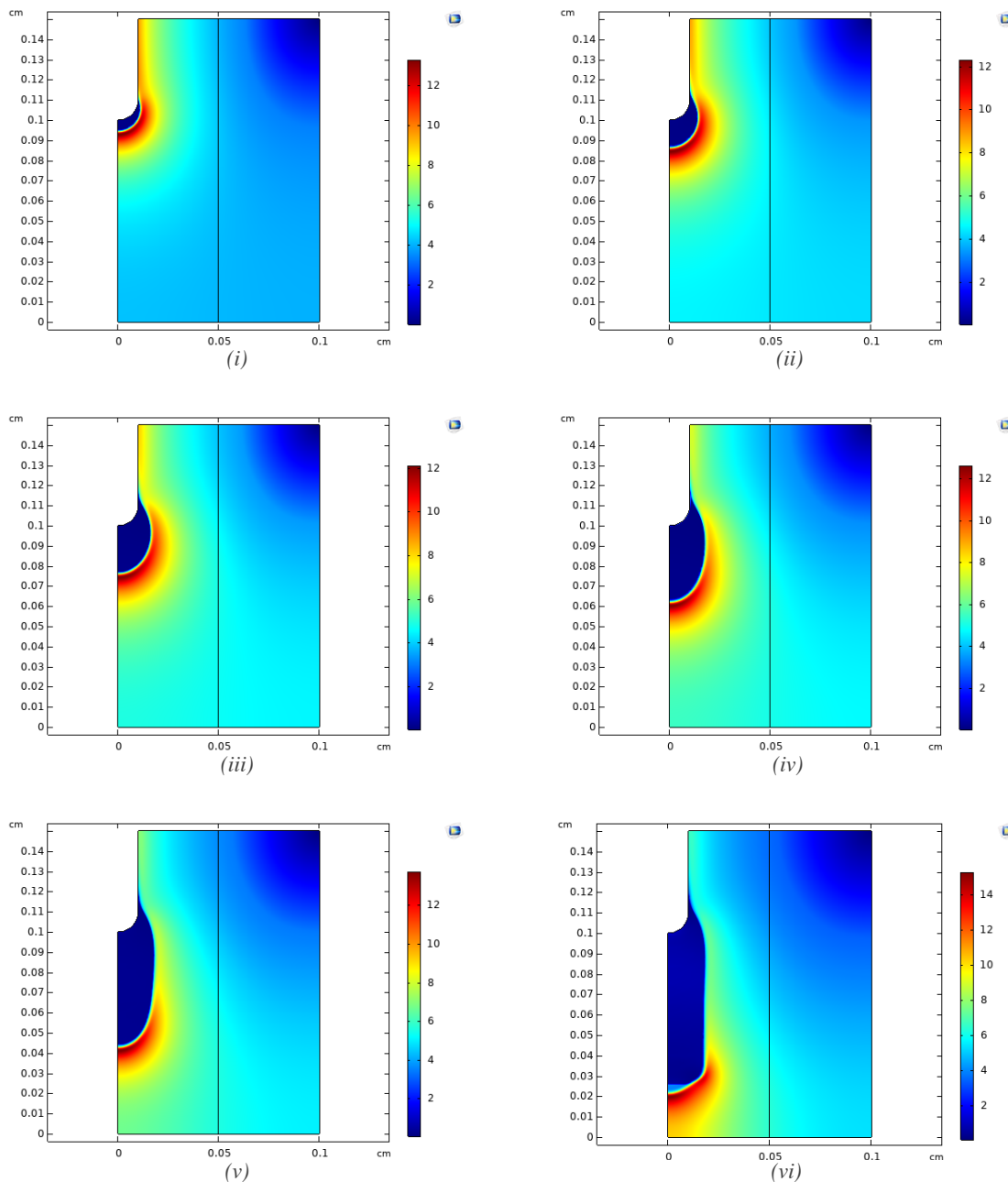


Figure 49 - The 2D surface plots of the electron mean energy (eV) profile for the streamer that propagates in a 1 mm air gap. (i) - $t = 0.3$ ns. (ii) - $t = 0.6$ ns. (iii) - $t = 1$ ns. (iv) - $t = 1.5$ ns. (v) - $t = 2$ ns. (vi) - $t = 2.5$ ns.

From the results in Figure 49, it is seen that the mean electron energy in the streamer channel is approximately 2 eV whilst the electron energy at the tip of the streamer ranges between 9 eV and 12

eV. The mean electron energy increases in magnitude to a value greater than 14 eV as the streamer reaches the cathode.

4.9.7 Positive and Negative Ion Density

Figure 50 below is the line graph of the positive ion density which is plotted against the symmetrical axis for different times.

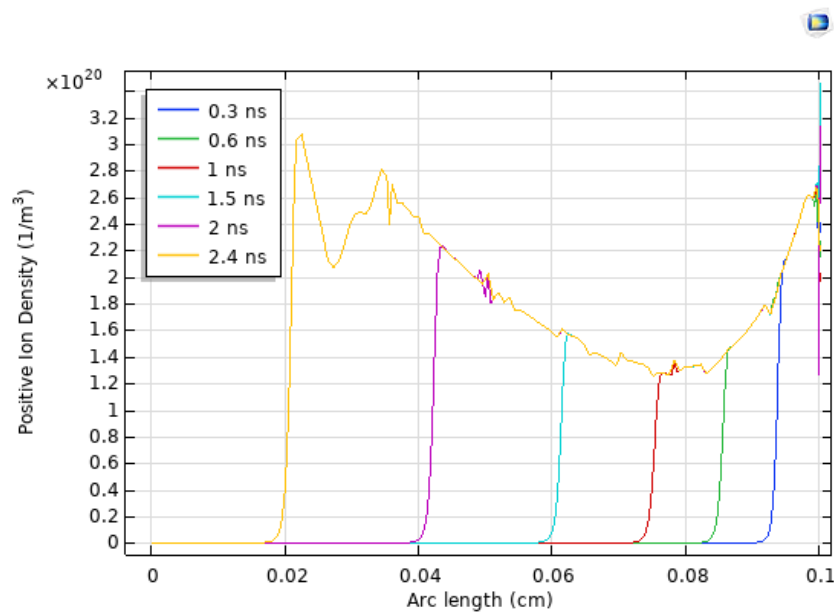


Figure 50 - Line graph showing the variation of the positive ion density on the symmetrical axis for different time steps.

Referring to Figure 50, it is seen that there is a reduction in the positive ion density when moving away from the anode as the positive ions that are produced from the ionization reactions have enough time to leave the anode due to the high axial fields. There is an increase in the regions that are closer to the anode as there is a long column of positive ions that exist within the positive column. The positive ion density increased at regions close to the grounded cathode when the time was equal to 2.4 ns thus resulting in a region of net positive charge. This occurs due to ionization processes that are caused by electrons that were emitted from the cathode. These ions attempt to be absorbed by the cathode but due to the ionization rate being much higher than the absorption rate, it results in a net positive charge [119].

Figure 51 below is the line graph of the negative ion density which is plotted against the symmetrical axis for different times.

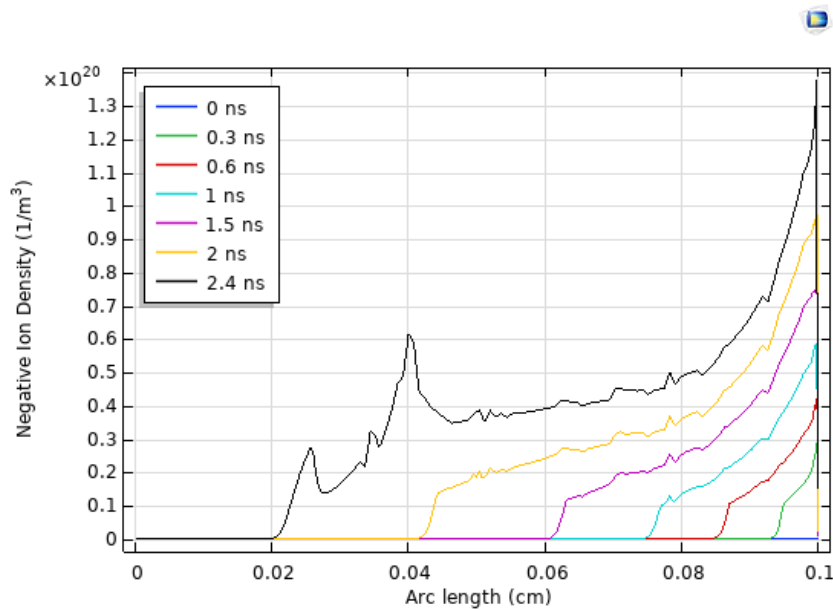


Figure 51 - Line graph showing the variation of the negative ion density on the symmetrical axis for different time steps.

Referring to Figure 51, it is seen that negative ion density is 0 m⁻³ at the cathode and the density increases when moving towards the anode. The negative ion density is the greatest with an approximate magnitude of 1.39×10²⁰ m⁻³ in the region that is closer to the anode. The increase in concentration of the negative ions at the anode is attributed to the attachment of the electrons to the neutral gas particles. There is a reduction in the concentration of these ions due to the recombination of positive ions and negative ions. Attachment is a process that dominates over recombination near the anode due to there being a reduced number of positive ions in this area. Therefore, it results in there being a maximum value of negative ions in that region [119]. When comparing both the line graphs of positive ion and negative ion densities, it is seen that the positive ion density is much greater in magnitude and the magnitude of the negative ion concentration is only comparable in regions that are closer to the anode.

4.9.8 A Comparison of Breakdown Voltage to Relative Humidity Using COMSOL Multiphysics

An investigation to determine the influence of humidity and pressure on the breakdown voltage in atmospheric air was also performed using the numerical model created of the cathode directed streamer. The change in humidity was done by altering the water content in the gas composition ratio mentioned in section 2.6.6. The water content values which were investigated using the numerical model was 0% (dry air), 0.5%, 1% and 1.35% and these water composition values correspond to a relative humidity of 0%, 35%, 70% and 94.4% respectively.

Figure 52 below, is a plot that depicts the change that occurs in the Townsend attachment coefficient when the relative humidity increased from 0% to 94.4%. The Townsend attachment coefficient is plotted against the reduced electric field.

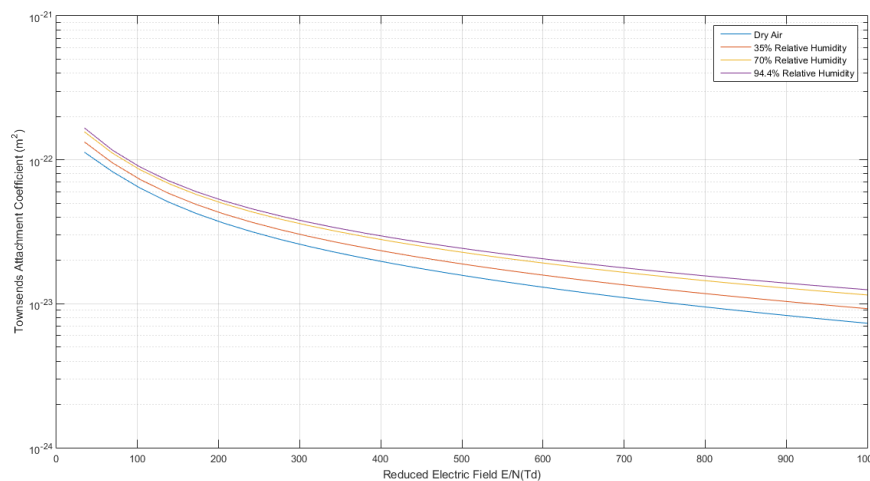


Figure 52 - Plot of the Townsend attachment coefficients as a function of the reduced electric field [61]. The water content values which were investigated in this comparison was 0%, 0.5%, 1% and 1.35% and these water composition values correspond to a relative humidity of 0%, 35%, 70% and 94.4% respectively. It should be noted that the y axis is on a log scale.

As seen in Figure 52, the Townsend attachment coefficient increases in magnitude as the water content in air increases. This is expected and a resulting increase in the attachment coefficient will cause the breakdown voltage of the air gap to increase.

Figure 53 is a plot that depicts change in breakdown voltage that occurs when the relative humidity increased in the system. The comparison was performed by keeping the pressure and temperature constant at magnitudes of 1 atm and 300 K respectively

It is seen in Figure 53, that there is a directly proportional relationship that exists between the relative humidity of the air gap and the breakdown voltage. This is expected as explained in section 2.5.10.1 and as seen in Figure 52, where the attachment coefficients increased as the water content increased. The breakdown voltage of the dry air gap was 2.7 kV and it increased by 9.3 % to a value of 2.95 kV when the relative humidity increased to 35%. The breakdown voltage of the air gap then increased by

1.7% to a magnitude of 3 kV when the relative humidity increased to a value of 70%. Despite there being a directly proportional relationship between the breakdown voltage and the relative humidity of the air gap, it is seen that there is a small increase in the magnitude of the breakdown voltage when the humidity increased from 0%-70%. There was a significant increase in breakdown voltage from 3 kV to 4 kV when the relative humidity increased from 70% to 94.4%. The breakdown voltage increased significantly by 33.33%. This occurred as there were more water molecules present in the air gap which subsequently increased the attachment coefficient, thus causing the breakdown strength of air to increase.

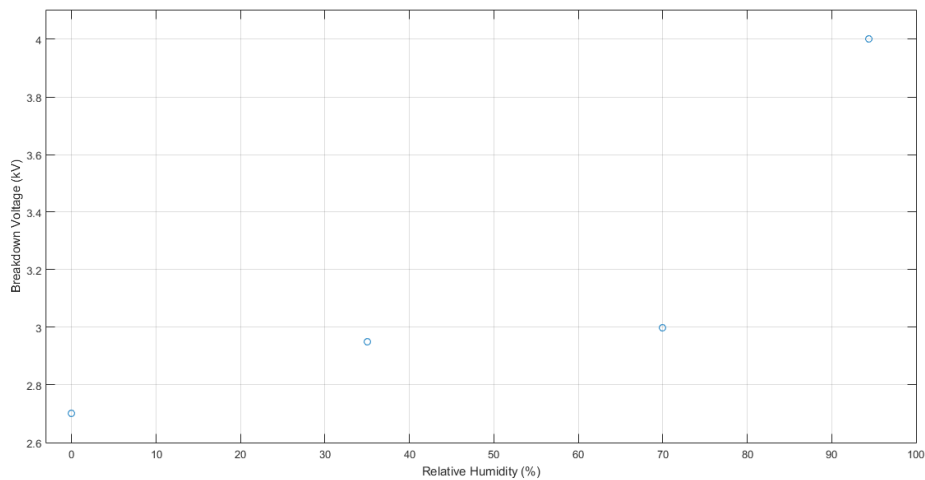


Figure 53 - The variation of breakdown voltage as a function of relative humidity (%) for an electrode gap length of 0.1 cm.

4.9.9 A Comparison of Breakdown Voltage to Pressure Using COMSOL Multiphysics

Figure 54 is a plot that is used to represent the change in breakdown voltage that occurs in the air gap modelled on COMSOL Multiphysics when pressure increases in it. The change in pressure was done by altering the pressure parameter (p) stated in section 4.9.1. The pressure magnitudes which were investigated were 1 atm, 2 atm, 3 atm and 4 atm. This comparison was performed by keeping the water content and temperature constant at magnitudes of 1% (70% relative humidity) and 300 K respectively.

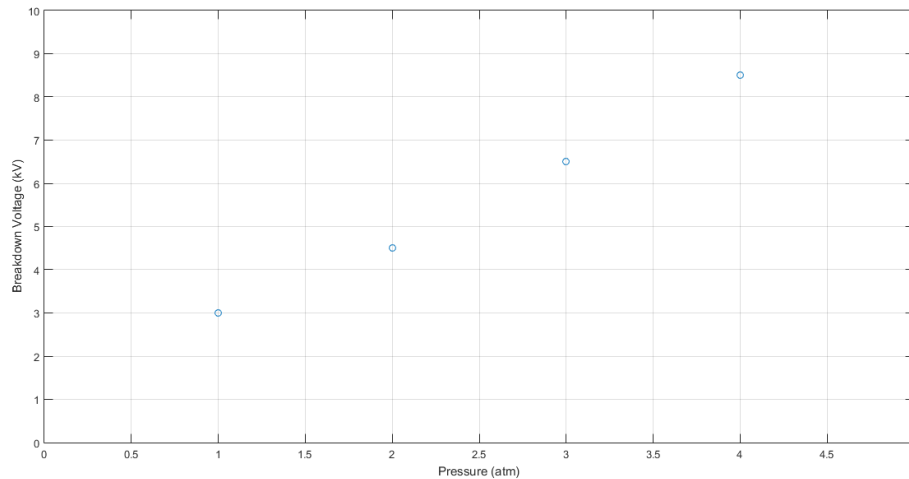


Figure 54 - The variation of breakdown voltage as a function of pressure (atm) for an electrode gap length of 0.1 cm.

Referring to Figure 54, it is seen that the breakdown voltage is directly proportional to the pressure in the air gap. This result is expected as explained in section 2.5.10.2. The breakdown voltage increases significantly when the pressure increases. There is 5.5 kV increase when the pressure of the system increased from 1 atm to 4 atm. Referring to Figure 55, it is observed from the 2D surface plots of the electron density that as the voltage increased the streamer would radially expand more at the anode tip and become narrow when propagating. This is seen when comparing frame (i) where the voltage was 3 kV to frame (ii) and (iii) where the voltage applied to the anode was 6.5 kV and 8.5 kV respectively.

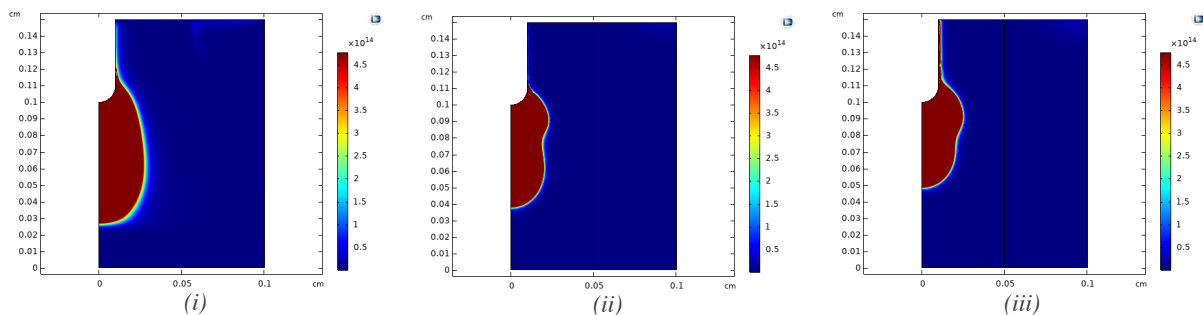


Figure 55 - The 2D surface plots of the electron density for a streamer modelled at different pressures in a 1 mm air gap .
(i) – $p = 1$ atm. (ii) – $p = 2$ atm. (iii) – $p = 3$ atm.

4.10 Chapter Summary

A numerical model of a cathode directed streamer propagating, in an air gap, was implemented on COMSOL Multiphysics. The distance between the high voltage electrode and grounded electrode was 0.1 cm. The following is a summary of the results obtained from the numerical simulation:

1. As expected, the application of a high voltage to the electrode resulted in concentrations of electrons moving towards the cathode. As seen in the 2D surface plot of the electron density in Figure 43, the streamer initiated and propagated towards the cathode. The electron density was in the range of 10^{19} - 10^{20} m^{-3} and this corresponds to an ionization degree of 10^{-5} - 10^{-4} which was expected for a streamer discharge.
2. From the results obtained it is seen that the time taken for the initiation of the streamer was 0.3 ns and it took 2.1 ns to propagate to the cathode therefore the total time that was required for the streamer to initiate and propagate in the air gap was 2.4 ns.
3. The velocity of the cathode directed streamer was 4.17×10^5 $\text{m}\cdot\text{s}^{-1}$ and this was in the required range of a short streamer (10^5 - 10^7 $\text{m}\cdot\text{s}^{-1}$).
4. Results from the numerical simulation showed that the enhanced electric field had a magnitude of 6×10^6 V/m whilst the streamer channel consisted of an electric field that had an approximate magnitude of 1×10^6 V/m.
5. It is seen in Figure 47 that the applied voltage collapsed when the enhanced electric field reached the cathode.
6. The magnitude of current at the anode was in the range of 0.01 A to 0.64 A which is expected for streamer discharges.
7. The mean electron energy in the streamer channel is approximately 2 eV whilst the electron energy at the tip of the streamer ranged between 9 eV and 12 eV. The mean electron energy then increased in magnitude to a value greater than 14 eV when the streamer reached the cathode.
8. The positive ion density has a greater magnitude at regions closer to the anode and the magnitude reduces when moving away from the anode. The positive ion density then increased at regions closer to the grounded cathode.
9. The negative ion density was 0 m^{-3} at the cathode and the density increased when moving towards the anode.

10. The results obtained from the investigation using the numerical model showed that the relative humidity and breakdown voltage have a directly proportional relationship with each other. There is a relatively small increase in breakdown voltage when the relative humidity increased from 0% to 70%. There is a substantial increase in breakdown voltage that occurred when the relative humidity increased from 70% to 90%.

11. The results obtained from the investigation that was performed using the numerical model showed that atmospheric pressure and breakdown voltage have a directly proportional relationship with each other. It was observed that the streamer would radially expand more at the anode tip and become narrow when the voltage applied to the anode increased.

5 Conclusion

The research that was presented in this dissertation consisted of an experiment and numerical models that were used to investigate the streamer breakdown of air gaps in subtropical conditions. Positive polarity HVDC was applied to the electrode. This investigation also involved finding out the influence humidity and pressure has on the breakdown voltage of various air gaps. As the streamer breakdown was investigated, the experimental work consisted of recording the initiation and propagation of the streamers that were formed in the needle-plane air gap using a high-speed camera. This allowed for the investigation to determine if the presence of space charge influences the path a streamer takes when propagating towards the cathode. This chapter includes the conclusions that were obtained from the research presented in this dissertation and includes recommendations for future work.

Humidity does influence the breakdown voltage of an air gap. The results showed that humidity did not influence the breakdown voltage significantly for the 2 cm air gap as pressure and temperature could have influenced the breakdown voltage. It was observed from the results of the 5 cm, 10 cm, and 12 cm air gap lengths that humidity has a directly proportional relationship with the breakdown voltage as seen on days when the atmospheric pressure was within the same magnitude. It was also seen in the results obtained from the experiment that there was a reduction in the breakdown voltage when the humidity increased. This could be a result of the breakdown developing out of the glow discharge without impulses present when a DC voltage is applied. The breakdown voltage of the largest gap length which was 15 cm had a significant trend with humidity as the breakdown voltage increased with an increase in humidity.

Analysing the results obtained from the numerical modelling chapter, it was observed that the breakdown voltage had a directly proportional relationship with the relative humidity in the 0.1 cm air gap. There was a small increase in breakdown voltage when the relative humidity increased from 0% to 70% but a significant increase occurred when the breakdown voltage increased from 70% to 90%. The directly proportional relationship is expected because the pressure and temperature of the system was controlled during the investigation.

The breakdown voltage is influenced by the atmospheric pressure, and this was seen in both experimental and numerical modelling chapters. The breakdown voltage of the smaller gaps did not have a significant trend with the atmospheric pressure. This could have been a result of humidity and temperature influencing the breakdown voltage. It was seen in the experiment that the breakdown voltage had significant trend for the longer air gaps as the breakdown voltage increased with an increase in temperature which was expected. There were deviations from this trend which is seen and could have been a result of both humidity and temperature having an influence on breakdown voltages.

The results that were obtained from the numerical model showed that there was a linear increase in the breakdown voltage as the pressure of the system increased and this was expected. It was also observed in the numerical model that the streamer would radially expand more at the anode tip and become narrow when the voltage applied to the electrode increased substantially.

For gap lengths that were greater than 10 cm in the experiment, it was observed that the streamer would take a bent path instead of taking a straight path when propagating towards the cathode. This is a result of space charge being present in the gap as the streamer is unable to propagate through areas of high concentration and it is required to go around these regions of excess concentration.

In conclusion, the results presented in this dissertation indicated that both humidity and pressure influence the breakdown voltage of an air gap. The hypothesis stated in this dissertation is accepted as the breakdown voltage of an air gap does increase when the humidity increases. Lastly, as observed in the results of the experiment and the necessary FEMM models, the presence of space charge does influence the path a streamer takes when propagating towards the cathode.

5.1 Recommendations

A test chamber will have to be designed and manufactured to control the pressure. This will keep it constant when determining humidity's influence on the breakdown voltage. This will negate the effects of pressure and will prevent it from influencing the breakdown voltage. This will also have to be done when determining the influence of pressure on the breakdown voltage. Another test chamber will have to be designed and manufactured for the humidity to be controlled throughout the experiment thus negating the effects of it on the breakdown voltage.

The experiment should also be performed in a room where the temperature is controlled and kept constant throughout the duration of the experiment. This will ensure that the breakdown voltage is not influenced by temperature.

As observed in the experiment, it was not possible to record the initiation and progression of streamer in small air gaps. The Schlieren method should be implemented to observe these structures as it is an optical effect that is caused by localised density changes in air. These changes are a result of thermal or shock effects and is seen by observing the light that is emitted from an external source which is refracted at different angles through the Schlieren [8].

The modelling of cathode directed streamers for longer air gaps will have to include the photoionization process in the numerical model. It ensures that enough electrons are present at the streamer head, and this assists the streamer in propagating towards the cathode. The photoionization rate for the numerical model is obtained by solving the Helmholtz equation which is represented by equation 48 below [120]:

$$\nabla^2 U - (\lambda_j p_{O_2})^2 U = -A_j p_{O_2}^2 I(r) \quad (48)$$

Where:

U : The intensity of photoionization per unit volume

λ_j and A_j : These are fitting parameters

p_{O_2} : The partial pressure of Oxygen

$I(r)$: The photon production rate which is proportional to the ionization rate.

A 3D model of a cathode directed streamer could be developed and it should include a region of space charge that is of a high concentration. It should be located at a point in the path a streamer would normally take when propagating in the air gap. This is done to see if the streamer will take a bent path and go around the region of excess space charge when propagating towards the cathode.

6 References

- [1] J. Schmid, "Influence of Absolute Humidity on the Electrical Breakdown in Air," *European Transactions on Electrical Power*, vol. 2, no. 5, pp. 327-331, 1992.
- [2] Y. Wang, D. Huang, J. Liu, Y. Zhang and L. Zeng, "Alternative Environmentally Friendly Insulating Gases for SF₆," *Processes*, vol. 7, no. 4, p. 216, 2019.
- [3] A. H. Mostajabi, M. H. Samimi, M. Arabzadeh, A. A. S. Akmal and H. Mohseni, "Effect of Humidity on the Breakdown Voltage of Insulators at Varying Humidity and Temperature Conditions," in *XVII International Symposium on High Voltage Engineering*, Hannover, 2011.
- [4] D. Wu, G. Asplund, B. Jacobson, M. Li and F. Sahlen, "Humidity Influence on Switching-Impulse Breakdown Voltage of Air Gaps for Indoor High-Voltage Installations," in *14th International Symposium on High Voltage Engineering*, Beijing, 2005.
- [5] E. Hussian, M. R. Nandgopal and B. R. Prabhakar, "Effect of Humidity on Breakdown Voltages of Gaps and Insulators," 1974. [Online]. Available: <http://journal.library.iisc.ernet.in/index.php/iisc/article/viewFile/3430/3479>. [Accessed 12 October 2021].
- [6] WorldData.info, "The Climate in South Africa," [Online]. Available: <https://www.worlddata.info/africa/south-africa/climate.php>. [Accessed 18 November 2021].
- [7] WorldData.info, "Climate of KwaZulu-Natal (South Africa)," [Online]. Available: <https://www.worlddata.info/africa/south-africa/climate-kwazulu-natal.php>. [Accessed 18 November 2021].
- [8] D. Mitchard, P. Widger and A. Haddad, "Analysis of Light Emission and Schlieren from Short Gap High Voltage Streamer Impulses Representing Lightning," 13 May 2021. [Online]. Available: <https://www.researchsquare.com/article/rs-310823/v2>. [Accessed 8 November 2021].
- [9] E. Kuffel, "Influence of Humidity on the Breakdown Voltage of Sphere-Gaps and Uniform-Field Gaps," *The Institution of Electrical Engineers*, vol. 108, no. 40, pp. 295-301, 1961.
- [10] D. Rodriguez, R. S. Gorur and P. M. Hansen, "Effect of Humidity on the Breakdown Characteristics of Air in Non-uniform Fields at 30 kHz," *IEEE Transactions on Dielectrics and*

Electrical Insulation, vol. 17, no. 1, pp. 45-52, 2010.

- [11] T. Takuma, O. Yamamoto and S. Hamada, "Gases as a Dielectric," in *Gaseous Dielectrics X*, New York, Springer Science+Business Media, Inc, 2004, pp. 195-204.
- [12] C. Wadhwa, *High Voltage Engineering*, New Delhi: New Age International (P) Limited, 2007.
- [13] D. Kind and H. Karner, *High-Voltage Insulation Technology*, Braunschweig: Springer Fachmedien Wiesbaden GmbH, 1985.
- [14] A. Küchler, *High Voltage Engineering*, Berlin: Springer Vieweg, 2018.
- [15] H. M. Ryan, *High-Voltage Engineering and Testing*, London: The Institution of Engineering and Technology, 2013.
- [16] F. A. Rizk and G. N. Trinh, *High Voltage Engineering*, Boca Raton: Taylor & Francis Group, LLC, 2014.
- [17] H. Schlager, V. Grewe and A. Roiger, "Chemical Composition of the Atmosphere," *Research Topics in Aeroapce*, pp. 17-35, 2012.
- [18] M. Seeger, T. Votteler, J. Ekeberg, S. Pancheshnyi and L. Sánchez, "Streamer and Leader Breakdown in Air at Atmospheric Pressure in Strongly Non-Uniform Fields in Gaps Less than One Metre," *IEEE Transactions on Dielectrics and Electrical Insulation*, vol. 25, no. 6, pp. 2147-2156, 2018.
- [19] L. Zheng-ying and C. Zhang, "Measurements of Synergisms of Strongly Electronegative Gaseous Mtxtures," in *Gaseous Dielectrics VII*, New York, Springer Science+Business Media, 1994, pp. 177-182.
- [20] D. W. Möller, "Fundamentals of Plasma Physics," 2006. [Online]. Available: <https://www.hzdr.de/db/Cms?pOid=23689>. [Accessed 6 February 2021].
- [21] E. Morse, *Nuclear Fusion*, Berkeley: Springer, 2018.
- [22] P. M. Bellan, *Fundamentals of Plasma Physics*, Cambridge: Cambridge University Press, 2008.
- [23] U. Inan and M. Gołkowski, *Principles of Plasma Physics for Engineers and Scientists*, New York: Cambridge University Press, 2011.

- [24] C. Lee, D. B. Graves, M. A. Lieberman and D. W. Hess, "Global Model of Plasma Chemistry in a High Density Oxygen Discharge," *Journal of The Electrochemical Society*, vol. 141, no. 6, pp. 1546-1555, 1994.
- [25] D. B. Go, "Gaseous Ionization and Ion Transport: An Introduction to Gas Discharges," 19 March 2012. [Online]. Available: https://www3.nd.edu/~sst/teaching/AME60637/notes/Go_ions_v4_031912.pdf. [Accessed 7 April 2021].
- [26] M. Ziaur Rahman and M. Mynuddin, "Kinetic Modelling of Atmospheric Pressure Nitrogen Plasma," *American Journal of Modern Physics*, vol. 7, no. 5, pp. 185-193, 2018.
- [27] N. S. J. Braithwaite, "Introduction to Gas Discharges," <https://iopscience.iop.org/journal/0963-0252>, vol. 9, p. 517–527, 2000.
- [28] E. N. Pusateri, H. E. Morris, E. . M. Nelson and W. Ji, "Determination of Equilibrium Electron Temperature and Times Using an Electron Swarm Model With BOLSIG+ Calculated Collision Frequencies and Rate Coefficients," *Journal of Geophysical Research: Atmospheres*, vol. 120, no. 15, pp. 7300-7315, 2015.
- [29] M. S. Naidu and V. Kamaraju, High Voltage Engineering, New Delhi: McGraw Hill Education (India) Private Limited, 2013.
- [30] S. Nijdam, E. van Veldhuizen and U. EbertP, "Photo and Background Ionization/ Streamer Propagation," in *XIIIth International symposium on High Pressure Low Temperature Plasma Chemistry HAKONE XIII*, Kazimierz Dolny, 2012.
- [31] J. R. Lucas, High Voltage Engineering, Sri Lanka, 2001.
- [32] M. A. Salem, H. Anis, A. El-Morshedy and R. Radwan, High-Voltage Engineering Theory and Practice, New York: Marcel Dekker, Inc., 2000.
- [33] G. Lehner, Electromagnetic Field Theory for Engineers and Physicists, Heidelberg: Springer, 2010.
- [34] E. Kuffel, W. Zaengl and J. Kuffel, High Voltage Engineering Fundamentals, Oxford: Butterworth-Heinemann, 2000.
- [35] M. Macken, "Modelling and Simulations of Corona Discharge Currents in a Large Scale

- Coaxial Geometry with a Dielectric Barrier due to Low Frequency Triangular Voltages,” 2014. [Online]. Available: <https://publications.lib.chalmers.se/records/fulltext/215798/215798.pdf>. [Accessed 19 May 2021].
- [36] R. Arora and W. Mosch, High Voltage And Electrical Insulation Engineering, New Jersey: John Wiley & Sons, Inc. , 2011.
- [37] A. Hallac, G. E. Georghiou and A. C. Metaxas, “Secondary Emission Effects on Streamer Branching in Transient Non-Uniform Short-Gap Discharges,” *Journal Of Physics D: Applied Physics*, vol. 36, pp. 2498-2509, 2003.
- [38] N. Y. Babaeva and G. . V. Naidis, “Dynamics of Positive and Negative Streamers in Air in Weak Uniform Electric Fields,” *IEEE Transactions On Plasma Science*, vol. 25, no. 2, pp. 375-379, 1997.
- [39] T. M. P. Briels, J. Kos, G. J. J. Winands, E. M. van Veldhuizen and U. Ebert, “Positive and Negative Streamers in Ambient Air: Measuring Diameter, Velocity and Dissipated Energy,” *Journal Of Physics D: Applied Physics*, vol. 41, p. 243004, 2008.
- [40] B. Bagheri , J. Teunissen , U. Ebert, M. M. Becker , S. Chen, O. Ducasse , O. Eichwald , D. Loffhagen, A. Luque , D. Mihailova, J. M. Plewa, J. van Dijk and M. Yousfi, “Comparison of Six Simulation Codes for Positive Streamers in Air,” *Plasma Sources Science and Technology*, vol. 27, no. 9, p. 095002, 2018.
- [41] S. Nijdam, J. Teunissen and U. Ebert, “The Physics of Streamer Discharge Phenomena,” *Plasma Sources Science and Technology*, vol. 29, p. 103001, 2020.
- [42] A. Luque, V. Ratushnaya and U. Ebert, “Positive and Negative Streamers in Ambient Air: Modeling Evolution and Velocities,” *Journal of Physics D Applied Physics*, vol. 41, no. 23, p. 234005, 2008.
- [43] Y. Geng and C. Zhuang, “Streamer Inception Electric-Field Criterion Under Positive Lightning Impulse Voltage Considering Voltage Rise Rate,” in *20th International Conference on Gas Discharges and their Applications*, Orleans, 2014.
- [44] Z. Wang and Y. Geng, “Study on the Streamer Inception Characteristics Under Positive Lightning Impulse Voltage,” *AIP Advances*, vol. 7, no. 11, p. 115115, 2017.
- [45] M. F. Abd Alameer and T. H. Khalaf , “Computational Analysis for Electrical Breakdown in

Air due to Streamer Discharge in Rod-to-Plane Arrangement,” in *IOP Conf. Series: Materials Science and Engineering*, Istanbul, 2020.

- [46] N. L. Allen and P. N. Mikropoulos, “Dynamics of Streamer Propagation in Air,” *Journal of Physics D Applied Physics*, vol. 32, pp. 913-919, 1999.
- [47] H. Kojima, T. Kitamura , S. Goto, K. Kobayashi , T. Kato, T. Rokunohe and N. Hayakawa, “Breakdown Mechanism Based on Secondary Streamer Propagation and Channel Heating Under Non-Uniform Electric Field in Air,” in *The 19th International Symposium on High Voltage Engineering*, Pilsen, 2015.
- [48] M. Radmilovic ´-Radjenovic ´ , B. Radjenovic ´ , Z. Nikitovic ´ , Š. Matejcik and M. Klas, “The Humidity Effect on the Breakdown Voltage Characteristics and the Transport Parameters of Air,” *Nuclear Instruments and Methods in Physics Research B*, vol. 279, pp. 103-105, 2012.
- [49] A. Paul Abraham and B. R. Prabhakar, “Effect of Humidity and Temperature on the DC Breakdown of Rod-Rod and Rod-Plane Gaps,” *IEEE Transactions on Electrical Insulation*, vol. 27, no. 2, pp. 207-213, 1992.
- [50] M. Kamarudin, N. Radzi, S. Zulkifli and R. Abd-Rahman, “Experimental Investigation on Air Breakdown Under Lightning Impulses with Various Electrode Configurations,” in *3rd IET International Conference on Clean Energy and Technology (CEAT)*, Kuching, 2014.
- [51] G. Govinda Raju and R. Hackam, “Sparking Potentials of Dry Air, Humid Air and Water Vapour Between Concentric Sphere-Hemisphere Electrodes,” *Proceedings of the Institution of Electrical Engineers*, vol. 120, no. 8, pp. 927-933, 1973.
- [52] T. Gora, “Investigating the Effects of Altitude (Air Density) on the HVDC Breakdown Voltage of Small Rod-Plane Air Gaps,” Johannesburg, 2016.
- [53] H. S. Uhm, S. . J. Jung and H. S. Kim, “Influence of Gas Temperature on Electrical Breakdown in Cylindrical Electrodes,” *Journal of the Korean Physical Society*, vol. 42, pp. 989-993, 2003.
- [54] G. Dandaron, G. Y. Dautov and G. Mustafin, “Effect of Gas Temperature on Breakdown Potential,” *Journal of Applied Mechanics and Technical Physics*, vol. 11, no. 1, pp. 140-143, 1970.
- [55] K. Ratnakar and B. R. Kamath, “Influence of Electrode Configuration on AC Breakdown Voltages,” *International Journal of Research and Scientific Innovation (IJRSI)*, vol. IV, no. VI,

pp. 60-63, 2017.

- [56] H. C. T. Fan , L. J. Ann , K. W. Loon, P. Y. Khai , H. Ahmad and R. . A. Gamboa , “Analysis of DC Breakdown Characteristics in Different Types Electrodes,” *Journal of Engineering Science and Technology*, pp. 157-167, 2019.
- [57] M. E. Abdel-kader, W. H. Gaber, F. A. Ebrahim and M. A. Abd Al-Halim, “Characterization of the Electrical Breakdown for DC Discharge in Ar-He Gas Mixture,” *Vacuum*, vol. 169, pp. 1-6, 2019.
- [58] S. Ward, H. Anis and A. Mahdy, “Electrode Roughness Effects on the Breakdown of Air-insulated Apparatus,” *IEEE Transactions on Dielectrics and Electrical Insulation*, vol. 5, no. 4, pp. 612-616, 1998.
- [59] T. Shioiri, T. Kamikawaji, E. Kaneko, M. Homma, H. Takahashi and I. Ohshima, “Influence of Electrode Area on the Conditioning Effect in Vacuum,” *IEEE Transactions on Dielectrics and Electrical Insulation*, vol. 2, no. 2, pp. 317-320, 1995.
- [60] H. Sharifpanah, A. Gholami and S. Jamali, “Effect of Electrode Material on the Breakdown Voltage of SF6-N2 and SF6-CO2 Mixtures in a Weakly Non-Uniform Electric Field,” in *2nd IEEE International Conference on Power and Energy* , Johor Baharu, 2008.
- [61] G. J. M. Hagelaar and L. C. Pitchford, “Solving the Boltzmann Equation to Obtain Electron Transport Coefficients and Rate Coefficients For Fluid Models,” *Plasma Sources Sci. Technol.* , vol. 14, no. 4, pp. 722-733, 2005.
- [62] J. Dutton, “A Survey of Electron Swarm Data,” *Journal of Physical and Chemical Reference Data*, vol. 4, no. 3, p. 1975, 577-856.
- [63] J. Liu and G. R. Govinda Raju, “Electron Swarm Parameters in Nitrogen Oxygen and Air,” *IEEE Transactions on Electrical Insulation*, vol. 28, no. 1, pp. 154-156, 1993.
- [64] G. G. Raju, “Collision Cross Sections in Gaseous Electronics Part I: What Do They Mean?,” *IEEE Electrical Insulation Magazine*, vol. 22, no. 4, pp. 5-23, 2006.
- [65] P. Verma, D. Mahato, J. Kaur and B. Antony, “Electron Induced Inelastic and Ionization Cross Section for Plasma Modeling,” *Physics of Plasmas*, vol. 23, no. 9, p. 093512, 2016.
- [66] F. Sohbatzadeh and H. Soltani, “Time-Dependent One-Dimensional Simulation of Atmospheric

- Dielectric Barrier Discharge in N₂/O₂/H₂O using COMSOL Multiphysics,” *Journal of Theoretical and Applied Physics* , vol. 12, pp. 53-63, 2018.
- [67] J. J. Lowke, “Theory of Electrical Breakdown in Air - The Role of Metastable Oxygen Molecules,” *Journal of Physics D: Applied Physics*, vol. 25, no. 2, p. 202, 2000.
- [68] M. Bordage, S. Pancheshnyi, S. Biagi , W. Morgan , G. Hagelaar , A. Phelps and L. Pitchford , “The LXCat project: Electron Scattering Cross Sections and Swarm Parameters for Low Temperature Plasma Modeling,” *Chemical Physics*, vol. 398, p. 148–153, 2012.
- [69] L. & A. Pitchford, L. & Bartschat, K. & Biagi, S. & Bordage, M. & Bray, I. & Brion, C. & Brunger, M. & Campbell, L. & Chachereau, A. & Chaudhury, B. & Christophorou, L. & Carbone, E. & Dyatko, N. & Franck, C. & Fursa and D. & Gangwar, “LXCat: An Open-Access, Web-Based Platform for Data Needed for Modeling Low Temperature Plasmas,” *Plasma Processes and Polymers*, vol. 14, p. 1600098, 2017.
- [70] Biagi database, [Online]. Available: www.lxcat.net/Biagi. [Accessed 14 June 2021].
- [71] Biagi database, [Online]. Available: www.lxcat.net/Biagi. [Accessed 13 June 2021].
- [72] Hayashi database, [Online]. Available: www.lxcat.net/Hayashi. [Accessed June 13 2021].
- [73] Y. Itikawa, “Cross Sections for Electron Collisions with Nitrogen Molecules,” *Journal of Physical and Chemical Reference Data*, vol. 35, no. 1, pp. 31-53, 2006.
- [74] M. Brown, “Replacement Insulation Gas for SF₆,” Durban, 2016.
- [75] Y. Itikawa, “Cross Sections for Electron Collisions with Oxygen Molecules,” *Journal of Physical and Chemical Reference Data*, vol. 38, no. 1, pp. 1-20, 2009.
- [76] H. K. Ibrahim, E. . A. Jawad and M. K. Jassim, “Studying the Swarm Parameters and Electron Transport Coefficients in N₂- CH₄ Mixtures Using BOLSIG+ Program,” *NeuroQuantology* , vol. 18, no. 2, pp. 106-111, 2020.
- [77] G. J. M. Hagelaar, “Brief Documentation of BOLSIG+ Version 03/2016,” 3 March 2016. [Online]. Available: <http://www.bolsig.laplace.univ-tlse.fr/manual.html>. [Accessed 1 July 2021].
- [78] E. Obame Ndong and A. Traore Ndama, “Breakdown Performance of N₂/O₂ Gas Mixtures in Quasi-Homogeneous Electric Field,” *SSRG International Journal of Electrical and Electronics*

Engineering, vol. 7, no. 11, pp. 22-30, 2020.

- [79] Y. V. Serdyuk, "Propagation of Cathode-Directed Streamer Discharges in Air," in *COMSOL Conference*, Rotterdam, 2013.
- [80] G. J. M. Hagelaar, "Coulomb Collisions in the Boltzmann Equation For Electrons In Low-Temperature Gas Discharge Plasmas," *Plasma Sources Science and Technology*, vol. 25, no. 1, pp. 1-15, 2016.
- [81] W. Sima, Q. Peng, . Q. Yang, T. Yuan and J. Shi, "Study of the Characteristics of a Streamer Discharge in Air Based on a Plasma Chemical Model," *IEEE Transactions on Dielectrics and Electrical Insulation*, vol. 19, no. 2, pp. 660-670, 2012.
- [82] N. L. Aleksandrov and E. M. Bazelyan, "Step Propagation of a Streamer in an Electronegative Gas," *Journal of Experimental and Theoretical Physics*, vol. 91, no. 4, pp. 724-735, 2000.
- [83] X. Chen, W. He, X. Du, X. Yuan, L. Lan, X. Wen and B. Wan, "Electron Swarm Parameters and Townsend Coefficients of Atmospheric Corona Discharge Plasmas by Considering Humidity," *Physics of Plasmas*, vol. 25, p. 063525, 2018.
- [84] S. Pancheshnyi, "Effective Ionization Rate in Nitrogen–Oxygen Mixtures," *Journal of Physics D: Applied Physics*, vol. 46, no. 15, p. 155201, 2013.
- [85] T. Iwata, H. Okubo, H. Kojima, N. Hayakawa and F. Endo, "Positive Streamer Propagation and Breakdown Characteristics in Non-uniform Air Gap," in *2010 International Conference on High Voltage Engineering and Application*, New Orleans, 2010.
- [86] A. S. Menesy, X. Jiang, M. A. Ali, H. M. Sultan, N. M. Alfakih and S. Kamel, "Partial Discharge and Breakdown Characteristics in Small Air Gap Lengths Under DC Voltage in Needle-Plane Electrode Configuration," in *IEEE IAS Industrial and Commercial Power System Asia Technical Conference*, Weihai, 2020.
- [87] P. N. Mikropoulos, B. C. Sarigiannidou, C. A. Stassinopoulos and C. Tsakiridis, "Influence Of Humidity On Positive Streamer Propagation and Breakdown in a Uniform Field in Air," *IEEE Transactions on Dielectrics and Electrical Insulation*, vol. 15, no. 2, pp. 416-425, 2008.
- [88] A. Luque, V. Ratushnaya and U. Ebert, "Positive and Negative Streamers in Ambient Air: Modeling Evolution and Velocities," *Journal of Physics D Applied Physics*, vol. 41, no. 23, 2008.

- [89] V. F. Tarasenko, G. V. Naidis, D. V. Beloplotov, M. I. Lomaev, D. A. Sorokin and N. Y. Babaeva, "Streamer Breakdown of Atmospheric-Pressure Air in a Non-Uniform Electric Field at High Overvoltages," *Russian Physics Journal*, vol. 61, no. 6, pp. 1135-1142, 2018.
- [90] IEEE, "IEEE Standard for High-Voltage Testing Techniques," *IEEE Std 4-2013 (Revision of IEEE Std 4-1995)*, pp. 1-213, 2013.
- [91] D. Taylor, T. Hallett, P. Lowe and P. Sanders, *Digital Photography Complete Course*, New York: DK Publishing, 2015.
- [92] M. Hanif, "Atmospheric Corrections in Dielectric Dry Tests," in *Institution of Engineers Pakistan Saudi Arabian*, Karachi, 2014.
- [93] D. Xiao, "Dielectric Strength of Atmosphere Air," in *Gas Discharge and Gas Insulation*, Shanghai, Springer-Verlag Berlin Heidelberg, 2016, pp. 149-194.
- [94] A. Fischer, "The Influence of Humidity on DC and AC Breakdown Voltage of Air Gaps," *Electra*, vol. 10, pp. 65-77, 1969.
- [95] L. B. Loeb and J. M. Meek, "The Mechanism of Spark Discharge in Air at Atmospheric Pressure. I," *Journal of Applied Physics*, vol. 11, pp. 438-447, 1940.
- [96] S. Pancheshnyi, M. Nudnova and A. Starikovskii, "Development of a Cathode-Directed Streamer Discharge in Air at Different Pressures: Experiment and Comparison with Direct Numerical Simulation," *Physical Review E*, vol. 71, pp. 016407-1 - 016407-12, 2005.
- [97] C. Zhang , V. F. Tarasenko, . T. Shao, D. V. Beloplotov, M. I. Lomaev, R. Wang, D. A. Sorokin and P. Yan, "Bent Paths of a Positive Streamer and a Cathode-Directed Spark Leader in Diffuse Discharges Preionized by Runaway Electrons," *Physics of Plasmas*, vol. 22, no. 3, pp. 033511-1 - 033511-8, 2015.
- [98] N. J. West, "Investigation into Phenomena Observed During the Interaction of a Focused High-Energy Laser Beam with High Voltage Electric Fields," Johannesburg, 2008.
- [99] N. Hayakawa, K. Hatta, S. Okabe and H. Okubo, "Streamer and Leader Discharge Propagation Characteristics Leading to Breakdown in Electronegative Gases," *IEEE Transactions on Dielectrics and Electrical Insulation*, vol. 13, no. 4, pp. 842-849, 2006.
- [100] O. Ducasse, L. Papageorghiou, O. Eichwald, N. Spyrou and M. Yousfi, "Critical Analysis on

Two-Dimensional Point-to-Plane Streamer Simulations Using the Finite Element and Finite Volume Methods,” *IEEE Transactions On Plasma Science*, vol. 35, no. 5, pp. 1287-1300, 2007.

- [101] COMSOL Multiphysics, “Plasma Module User’s Guide,” 2018. [Online]. Available: <https://doc.comsol.com/5.4/doc/com.comsol.help.plasma/PlasmaModuleUsersGuide.pdf>. [Accessed 16 July 2021].
- [102] COMSOL Multiphysics, “Model Low-Temperature Nonequilibrium Discharges with the Plasma Module,” 2021. [Online]. Available: <https://www.comsol.com/plasma-module>. [Accessed 16 July 2021].
- [103] COMSOL Multiphysics, “Introduction to Plasma Module,” 2019. [Online]. Available: <https://doc.comsol.com/5.5/doc/com.comsol.help.plasma/IntroductionToPlasmaModule.pdf>. [Accessed 16 July 2021].
- [104] S. Singh, “Computational Framework for Studying Charge Transport in High-Voltage Gas-Insulated Systems,” Gothenburg, 2015.
- [105] COMSOL Multiphysics, “Negative Streamer in Nitrogen,” 2021. [Online]. Available: <https://www.comsol.com/model/negative-streamer-in-nitrogen-44551>. [Accessed 21 July 2021].
- [106] M. Benziada, A. Boubakeur and A. Mekhaldi, “Numerical Simulation of Streamer Propagation in Point-Plane Air Gaps using COMSOL Multiphysics,” in *The Electrical Engineering International Conference EEIC'19*, Bejaia, 2019.
- [107] COMSOL Multiphysics, “Atmospheric Pressure Corona Discharge in Air,” 2021. [Online]. Available: <https://www.comsol.com/model/atmospheric-pressure-corona-discharge-in-air-44311>. [Accessed 21 July 2021].
- [108] H. Lu, Z. Liu, X. Yan, D. Li, L. Parent and H. Tian, “Electron Work Function – A Promising Guiding Parameter for Material Design,” *Scientific Reports*, vol. 6, p. 24366, 2016.
- [109] C. Li, U. Ebert and W. Brok, “Avalanche-to-Streamer Transition in Particle Simulations,” *IEEE Transactions on Plasma Science*, vol. 36, no. 4, pp. 910-911, 2008.
- [110] W. J. Yi and P. F. Williams, “Experimental Study of Streamers in Pure N₂ And N₂/O₂ Mixtures and A \approx 13 cm Gap,” *Journal of Physics D: Applied Physics*, vol. 35, no. 3, pp. 205-218, 2002.

- [111] H. Sun, S. Huang, Q. Wang, S. Wang and W. Zhao, “Characteristics of Negative Corona Discharge in Air at Various Gaps,” <https://ieeexplore.ieee.org/xpl/RecentIssue.jsp?punumber=27>, vol. 47, no. 1, pp. 736-741, 2019.
- [112] F. Boakye-Mensah, N. Bonifaci, R. Hanna and I. Niyonzima, “Implementation of a Cathode Directed Streamer Model in Air Under Different Voltage Stresses,” in *COMSOL Conference 2020 Europe*, Grenoble, 2020.
- [113] W. Frei, “Meshing Considerations for Linear Static Problems,” COMSOL Multiphysics, 22 October 2013. [Online]. Available: <https://www.comsol.com/blogs/meshing-considerations-linear-static-problems/>. [Accessed 23 July 2021].
- [114] S. Pancheshnyi, P. Segur, . J. Capeillere and A. Bourdon, “Numerical Simulation of Filamentary Discharges with Parallel Adaptive Mesh Refinement,” *Journal of Computational Physics*, vol. 227, no. 13, pp. 6574-6590, 2008.
- [115] W. Frei, “Using Adaptive Meshing for Local Solution Improvement,” COMSOL Multiphysics, 27 December 2013. [Online]. Available: <https://www.comsol.com/blogs/using-adaptive-meshing-local-solution-improvement/>. [Accessed 23 July 2021].
- [116] M. Macken, “Modelling and Simulations of Corona Discharge Currents in a Large Scale Coaxial Geometry with a Dielectric Barrier due to Low Frequency Triangular Voltages,” Gothenburg, 2014.
- [117] A. Griesmer, “Size Parameters for Free Tetrahedral Meshing in COMSOL Multiphysics,” COMSOL Multiphysics, 30 January 2014. [Online]. Available: <https://www.comsol.com/blogs/size-parameters-free-tetrahedral-meshing-comsol-multiphysics/>. [Accessed 30 September 2021].
- [118] COMSOL Multiphysics, “Introduction to Solvers and Studies,” [Online]. Available: https://doc.comsol.com/5.5/doc/com.comsol.help.comsol/comsol_ref_solver.27.002.html. [Accessed 2 October 2021].
- [119] A. Papadakis, G. Georghiou and A. Metaxas, “Two-Dimensional Axisymmetric Simulations and the Heating Effects Associated with DC Atmospheric Pressure Discharges During the Post-Streamer Stage,” *IET Science, Measurement & Technology*, vol. 1, no. 2, pp. 113-120, 2007.
- [120] S. Singh, Y. Serdyuk and R. Summer, “Adaptive Numerical Simulation of Streamer

Propagation in Atmospheric Air,” in *COMSOL Conference*, Rotterdam, 2013.

[121] T. N. Olney, N. M. Cann, G. Cooper and C. E. Brion, “Chemical Physics,” *Absolute Scale Determination for Photoabsorption Spectra and The Calculation Of Molecular Properties Using Dipole Sum-Rules*, vol. 223, no. 1, pp. 59-98, 1997.

[122] E. Önal, “Breakdown Characteristics of Gases in Non-Uniform Fields,” *Journal of Electrical & Electronics Engineering*, vol. 4, no. 2, pp. 1177-1182, 2011.

Appendix A

Tabulated Results Obtained from the Bolsig+ Simulation

Table 10 - The results obtained from the BOLSIG+ simulation. The reduced electric field was varied from 0-1000 Td and the values for the corresponding mean electron energy, electron mobility, diffusion coefficient, Townsend's ionization, and attachment coefficient is seen.

Reduced Electric Field (Td)	Mean Electron Energy (eV)	Mobility (1/m·V·S)	Diffusion Coefficient (1/m·s)	Townsend Ionization Coefficient (m ²)	Townsend Attachment Coefficient (m ²)
0.000	0.1543E-01	0.2153E+26	0.2217E+24	0.000	0.000
34.48	3.375	0.1420E+25	0.3414E+25	0.2193E-23	0.1566E-21
68.97	4.457	0.1317E+25	0.4202E+25	0.7237E-22	0.1114E-21
103.4	5.343	0.1239E+25	0.4752E+25	0.3475E-21	0.8516E-22
137.9	6.113	0.1177E+25	0.5171E+25	0.8639E-21	0.6862E-22
172.4	6.802	0.1127E+25	0.5513E+25	0.1569E-20	0.5743E-22
206.9	7.416	0.1084E+25	0.5780E+25	0.2396E-20	0.4943E-22
241.4	8.004	0.1051E+25	0.6049E+25	0.3292E-20	0.4342E-22
275.9	8.545	0.1021E+25	0.6271E+25	0.4222E-20	0.3874E-22
310.3	9.057	0.9956E+24	0.6475E+25	0.5165E-20	0.3499E-22
344.8	9.546	0.9726E+24	0.6662E+25	0.6107E-20	0.3191E-22
379.3	10.01	0.9518E+24	0.6834E+25	0.7040E-20	0.2932E-22
413.8	10.46	0.9333E+24	0.6999E+25	0.7958E-20	0.2711E-22
448.3	10.90	0.9161E+24	0.7151E+25	0.8857E-20	0.2521E-22
482.8	11.33	0.9008E+24	0.7302E+25	0.9737E-20	0.2355E-22
517.2	11.75	0.8868E+24	0.7448E+25	0.1060E-19	0.2209E-22
551.7	12.15	0.8737E+24	0.7588E+25	0.1143E-19	0.2078E-22
586.2	12.56	0.8616E+24	0.7723E+25	0.1225E-19	0.1962E-22
620.7	12.95	0.8507E+24	0.7863E+25	0.1305E-19	0.1858E-22
655.2	13.34	0.8402E+24	0.7992E+25	0.1382E-19	0.1763E-22
689.7	13.72	0.8303E+24	0.8118E+25	0.1458E-19	0.1677E-22
724.1	14.10	0.8208E+24	0.8238E+25	0.1531E-19	0.1598E-22
758.6	14.47	0.8121E+24	0.8360E+25	0.1603E-19	0.1526E-22
793.1	14.84	0.8039E+24	0.8480E+25	0.1672E-19	0.1460E-22
827.6	15.21	0.7961E+24	0.8598E+25	0.1740E-19	0.1398E-22
862.1	15.58	0.7889E+24	0.8720E+25	0.1806E-19	0.1342E-22
896.6	15.94	0.7819E+24	0.8836E+25	0.1870E-19	0.1289E-22
931.0	16.30	0.7752E+24	0.8950E+25	0.1933E-19	0.1240E-22
965.5	16.66	0.7688E+24	0.9064E+25	0.1994E-19	0.1194E-22
1000.	17.01	0.7625E+24	0.9169E+25	0.2053E-19	0.1151E-22

MATLAB Code Used for the Calculation of the Effective Ionization Coefficient

```
reducedelectricfield=1.000;35.45;69.90;104.3;138.8;173.2;207.7;242.1;276.6;  
311.0;345.5;379.9;414.4;448.8;483.3;517.7;552.2;586.6;621.1;655.5;690.0;724  
.4;758.9;793.3;827.8;862.2;896.7;931.1;965.6;1000.];  
ionization=[0.000;0.2410E-23;0.7575E-22;0.3567E-21;0.8782E-21;0.1587E-  
20;0.2415E-20;0.3311E-20;0.4241E-20;0.5184E-20;0.6125E-20;0.7056E-  
20;0.7973E-20;0.8871E-20;0.9750E-20;0.1061E-19;0.1145E-19;0.1226E-  
19;0.1306E-19;0.1383E-19;0.1458E-19;0.1532E-19;0.1603E-19;0.1673E-  
19;0.1740E-19;0.1806E-19;0.1871E-19;0.1933E-19;0.1994E-19;0.2053E-19];  
attachment=[0.5304E-22;0.1571E-21;0.1108E-21;0.8473E-22;0.6834E-22;0.5722E-  
22;0.4928E-22;0.4332E-22;0.3867E-22;0.3493E-22;0.3185E-22;0.2927E-  
22;0.2708E-22;0.2518E-22;0.2353E-22;0.2207E-22;0.2077E-22;0.1961E-  
22;0.1857E-22;0.1762E-22;0.1676E-22;0.1598E-22;0.1526E-22;0.1460E-  
22;0.1398E-22;0.1342E-22;0.1289E-22;0.1240E-22;0.1194E-22;0.1151E-22];  
effectiveionization=ionization-attachment;  
semilogy(reducedelectricfield,effectiveionization);  
xlabel('Reduced Electric Field E/N (Td)')  
ylabel('Effective Ionization Coefficient (\alpha-\eta)/N (m^2)')  
grid on;
```

Appendix B

HVDC Generator

The circuit diagram of the high voltage DC generator used is seen by referring to Figure 56 below.

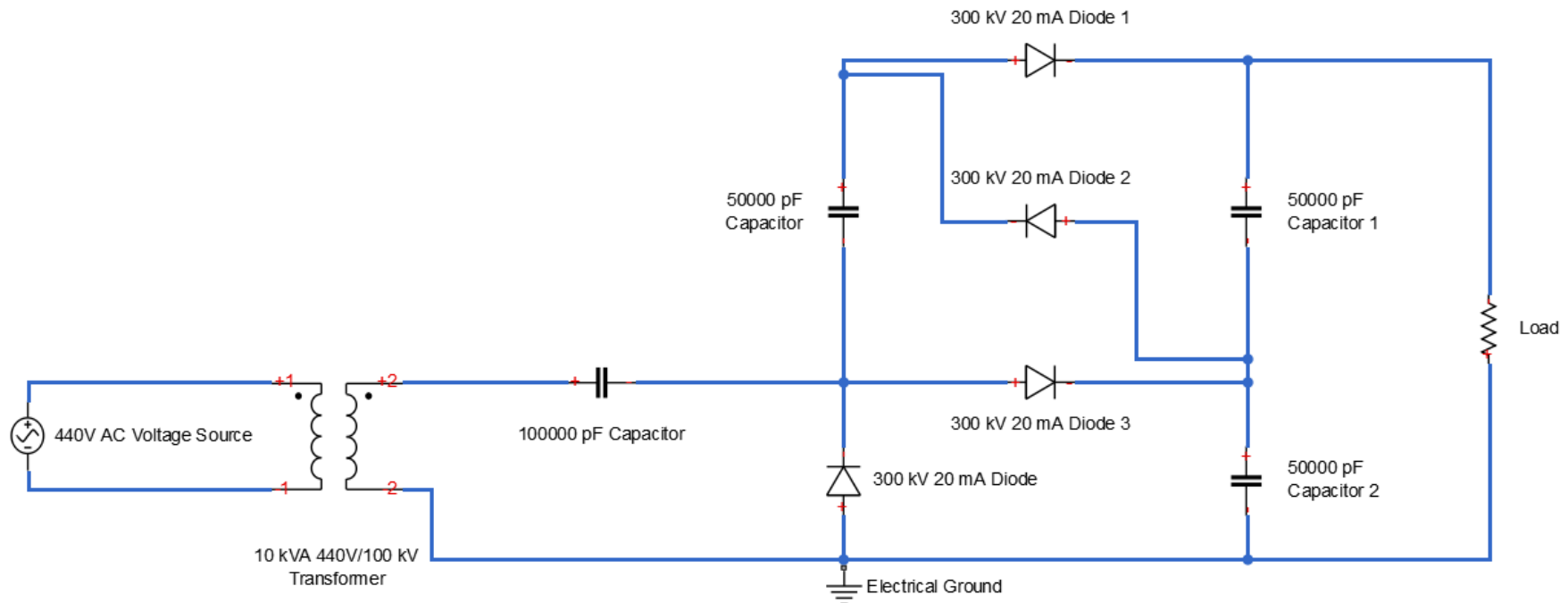


Figure 56 - The circuit diagram of the high voltage direct current generator with ratings of the components that was used in the experimental procedure. The needle-plane air gap was the "load" for the experiment.

Calibration of Haefely Hipotronics Vertical Sphere Gap System

The system was initially designed to perform AC, DC and impulse voltage calibration using the spheres that were installed. These spheres were replaced with needle-plane electrodes that were required for the experiment. A recalibration of the machine was required when the electrodes were changed. This was done to determine the amount of distance the mechanical shaft was required to move when setting a gap length.

The recalibration was done by first manually adjusting the gap length between the electrodes to 2 cm and record the value seen on the control unit. This value was 720 mm. It was then required to find out how much the control unit needs to be adjusted so that the distance between the electrodes has been changed by one centimetre. Through a trial-and-error method it was determined that a change in 34 mm on the control unit resulted in a change in length of 1 cm between the two electrodes. As the experiment was conducted for gap lengths of 2cm, 5 cm, 10 cm, 12 cm, and 15 cm, it was required to calculate the distance that needed to be set on the control unit. This value was then set on the control unit when performing the experiment for a specific gap length. Table 11 below indicates the value that was set on the control unit for the corresponding gap length.

Table 11 - Table indicating the values the control unit was set to when a specific gap length was being investigated.

Gap Length (cm)	Control Unit Value (mm)
2	720
5	822
10	992
12	1060
15	1162

The Procedure of Atmospheric Correction

As indicated in [90], the standard atmosphere conditions are:

Temperature (t_0): 20°C

Pressure (p_0): 101.3 kPa

Absolute humidity: 11 g/m³

Two factors were required to be obtained when calculating the equivalent value in Method 2. These factors were the air density correction factor (k_d) and the humidity correction factor (k_h).

The disruptive discharge voltage is obtained using equation 49 [90]:

$$V_0 = V \div \left(\frac{k_d}{k_h} \right) \quad (49)$$

Where:

V_0 : The voltage at standard reference atmosphere.

V : Breakdown voltage obtained in the experiment.

The air density correction factor, k_d , is obtained using equation 50 [90]:

$$k_d = \left(\frac{p}{p_0} \right)^m \times \left(\frac{273 + t_0}{273 + t} \right)^n \quad (50)$$

Where:

p_0 : Atmospheric pressure when test was performed

t_0 : Atmospheric temperature when test was performed

m : 1

n : 1

The humidity correction factor, k_h , is obtained using equation 51 [90]:

$$k_h = k^w \quad (51)$$

Where:

k : constant that is a function of the absolute humidity obtained in [90].

w : 1

The factors were entered into the MATLAB code created to calculate the voltage at standard atmosphere. The MATLAB code is seen in figure 57.

```
t0=20;
p0=101.3;
prompt='Please input pressure in hPa: ';
phpa=input(prompt);
pbar=phpa/10;
promptemp='Please input temperature in
centigrade: ';
tcent=input(promptemp);
promptBDV='Please input breakdown
voltage: ';
BDV=input(promptBDV);
promptkh='Please input kh value: ';
kh=input(promptkh);
kd=(pbar/p0)*((273+t0)/(273+tcent));
CorrectedBDV=BDV/(kd/kh);
display(pbar);
display(tcent);
display(kd);
display(kh);
display(BDV);
display(CorrectedBDV);
```

Figure 57 - The MATLAB code created to correct the breakdown voltage to standard atmosphere conditions.

Tabulated Results Obtained in the Experiment

Day 1

Table 12 - The atmospheric conditions and the breakdown voltage recorded for various air gaps on day one of the experiment. To improve accuracy, the experiment was conducted five times and the average breakdown voltage was used.

Gap Length (cm)	Temp (°C)	Pressure (hPa)	Relative Humidity (%)	Absolute Humidity (g/m ³)	V _{BD-1} (V)	V _{BD-2} (V)	V _{BD-3} (V)	V _{BD-4} (V)	V _{BD-5} (V)	V _{BD-Avg} (V)
2	21.7	986.4	73.9	14.11	16.28	15.95	15.84	15.95	16.28	16.06
5	22.1	986.5	71.6	13.98	34.1	33.77	35.53	33.55	34.1	34.21
10	22.4	986.3	71.4	14.23	52.8	51.7	52.03	53.46	53.46	52.69
12	22.8	985.8	71.1	14.46	61.93	61.71	61.05	61.93	62.37	61.80
15	22.4	986.2	69.7	13.85	73.7	72.38	72.27	72.71	73.81	72.97

Table 13 - The atmospheric conditions and the corrected breakdown voltage recorded for various air gaps on day one of the experiment.

Gap Length (cm)	Temp (°C)	Pressure (hPa)	Absolute Humidity (g/m ³)	V _{BD-Avg} (V)	k _d	k _h	V ₀ (V)
2	21.7	986.4	14.11	16.06	0.9681	0.976	16.1906
5	22.1	986.5	13.98	34.21	0.9669	0.979	34.6378
10	22.4	986.3	14.23	52.69	0.9657	0.974	53.1411
12	22.8	985.8	14.46	61.80	0.9639	0.972	62.3169

15	22.4	986.2	13.85	72.97	0.9656	0.978	73.9044
-----------	------	-------	-------	-------	--------	-------	---------

Day 2

Table 14 - The atmospheric conditions and the breakdown voltage recorded for various air gaps on day two of the experiment. To improve accuracy, the experiment was conducted five times and the average breakdown voltage was used.

Gap Length (cm)	Temp (°C)	Pressure (hPa)	Relative Humidity (%)	Absolute Humidity (g/m ³)	V _{BD-1} (V)	V _{BD-2} (V)	V _{BD-3} (V)	V _{BD-4} (V)	V _{BD-5} (V)	V _{BD-Avg} (V)
2	22.4	989.7	58.7	11.66	16.5	15.29	15.18	18.59	14.52	16.02
5	22.8	989.5	58.3	11.85	36.3	36.52	37.4	41.69	35.20	37.42
10	23.1	989.6	58.1	12.06	59.62	61.27	70.51	66.55	58.63	63.32
12	23.4	989.3	58.2	12.25	75.13	67.98	78.21	71.61	63.80	71.35
15	23.7	989.1	58.8	12.59	79.31	81.4	79.97	88.00	75.90	80.92

Table 15 - The atmospheric conditions and the corrected breakdown voltage recorded for various air gaps on day two of the experiment.

Gap Length (cm)	Temp (°C)	Pressure (hPa)	Absolute Humidity (g/m ³)	V _{BD-Avg} (V)	k _d	k _h	V ₀ (V)
2	22.4	989.7	11.66	16.02	0.9691	0.994	16.4323
5	22.8	989.5	11.85	37.42	0.9676	0.993	38.4041
10	23.1	989.6	12.06	63.32	0.9667	0.992	64.9790
12	23.4	989.3	12.25	71.35	0.9654	0.990	73.1680
15	23.7	989.1	12.59	80.92	0.9642	0.988	82.9148

Day 3

Table 16 - The atmospheric conditions and the breakdown voltage recorded for various air gaps on day three of the experiment. To improve accuracy, the experiment was conducted five times and the average breakdown voltage was used.

Gap Length (cm)	Temp (°C)	Pressure (hPa)	Relative Humidity (%)	Absolute Humidity (g/m ³)	V _{BD-1}	V _{BD-2}	V _{BD-3}	V _{BD-4}	V _{BD-5}	V _{BD-Avg}
2	21.4	994.7	62.3	11.69	16.61	15.51	16.17	15.29	16.06	15.93
5	21.6	994.6	61.5	11.67	27.94	33.33	36.08	35.42	34.98	33.55
10	22.4	994.3	62.5	12.42	71.39	66.33	56.98	66.00	62.92	64.72
12	22.6	994.2	61.6	12.38	68.09	79.2	68.42	76.01	77.44	73.83
15	23.0	994.0	61.6	12.67	85.36	78.98	85.80	88.00	87.56	85.14

Table 17 - The atmospheric conditions and the corrected breakdown voltage recorded for various air gaps on day three of the experiment.

Gap Length (cm)	Temp (°C)	Pressure (hPa)	Absolute Humidity (g/m ³)	V _{BD-Avg} (V)	k _d	k _h	V ₀ (V)
2	21.4	994.7	11.69	15.93	0.9773	0.995	16.2191
5	21.6	994.6	11.67	33.55	0.9765	0.994	34.1511
10	22.4	994.3	12.42	64.72	0.9736	0.982	65.2807
12	22.6	994.2	12.38	73.83	0.9728	0.981	74.4517
15	23.0	994.0	12.67	85.14	0.9713	0.988	86.6040

Day 4

Table 18 - The atmospheric conditions and the breakdown voltage recorded for various air gaps on day four of the experiment. To improve accuracy, the experiment was conducted five times and the average breakdown voltage was used.

Gap Length (cm)	Temp (°C)	Pressure (hPa)	Relative Humidity (%)	Absolute Humidity (g/m ³)	V _{BD-1}	V _{BD-2}	V _{BD-3}	V _{BD-Avg}
2	22.6	989.1	67.4	13.55	15.73	14.85	12.87	14.48
5	23.4	989.5	68.0	14.31	34.98	30.36	33.22	32.85
10	23.9	989.7	66.2	14.33	63.58	54.56	63.36	60.50
12	24.4	990.1	65.9	14.68	71.72	66.77	58.19	65.56
15	25.0	990.8	63.4	14.61	88.00	88.00	88.00	88.00

Table 19 - The atmospheric conditions and the corrected breakdown voltage recorded for various air gaps on day four of the experiment.

Gap Length (cm)	Temp (°C)	Pressure (hPa)	Absolute Humidity (g/m ³)	V _{BD-Avg} (V)	k _d	k _h	V ₀ (V)
2	22.6	989.1	13.55	14.48	0.9678	0.980	14.6623
5	23.4	989.5	14.31	32.85	0.9656	0.974	33.1359
10	23.9	989.7	14.33	60.50	0.9642	0.975	61.1799
12	24.4	990.1	14.68	65.56	0.9629	0.972	66.1773
15	25.0	990.8	14.61	88.00	0.9617	0.972	88.9449

Appendix C

Numerical Simulation of a 2 cm Air Gap

As stated previously, it was attempted to perform a numerical simulation of a 2 cm air gap as it was investigated in the experiment. The geometric model of the air gap created on COMSOL Multiphysics is seen in Figure 58.

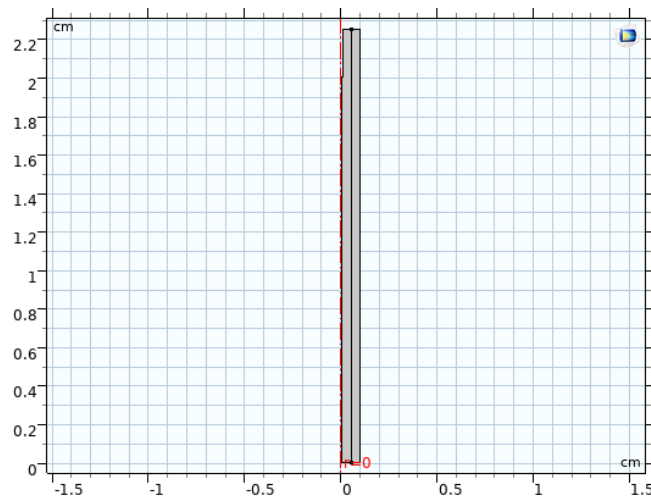


Figure 58 - The geometry of the 2 cm air gap that was implemented in COMSOL Multiphysics.

The model was simulated and the 2D surface plot of the electron density is seen in Figure 59.

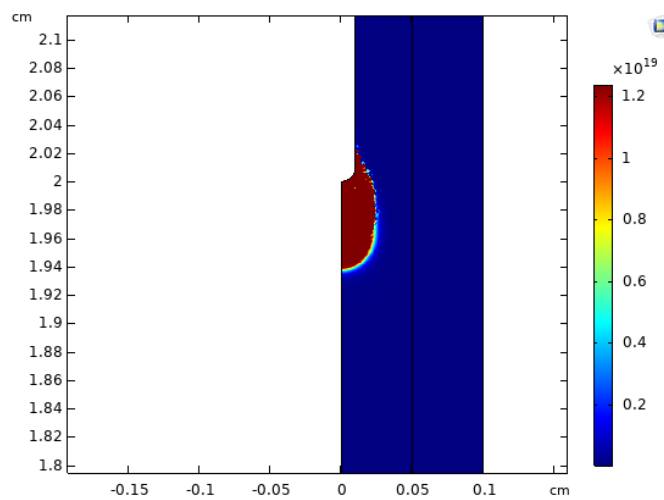


Figure 59 - The 2D surface plots of the electron density which shows the initiation of the streamer at 1 ns.

The streamer would initiate as seen in Figure 59, but it would not propagate any further. This occurred as the model did not have photoionization implemented in it. Cathode directed streamers require electrons to be fed into the head of the streamer to propagate. Therefore, photoionization is necessary to ensure propagation of a cathode directed streamer.

Numerical Instabilities Observed

The “Extremely Fine Mesh” setting was selected to create a mesh as it is commonly used for modelling of plasma. The magnitude of the elements is predefined by COMSOL Multiphysics and is seen in Table 20.

Table 20 - The settings used to create a mesh that resulted in numerical instabilities.

	Domain – Extremely Fine Mesh
Adaptive Mesh Refinement	Included
Minimum Element Size	0.00113
Maximum Element Size	0.135
Maximum Element Growth Rate	1.1
Curvature factor	0.2

The numerical instabilities that are a result of an incorrectly sized mesh is seen in Figure 60. It is seen in these plots that they are of a poor resolution which resulted in pixelated portions of electron density in (i) and caused there to be a significant amount of fluctuation in (ii). This negatively influences the results and prevents the propagation of the streamer.

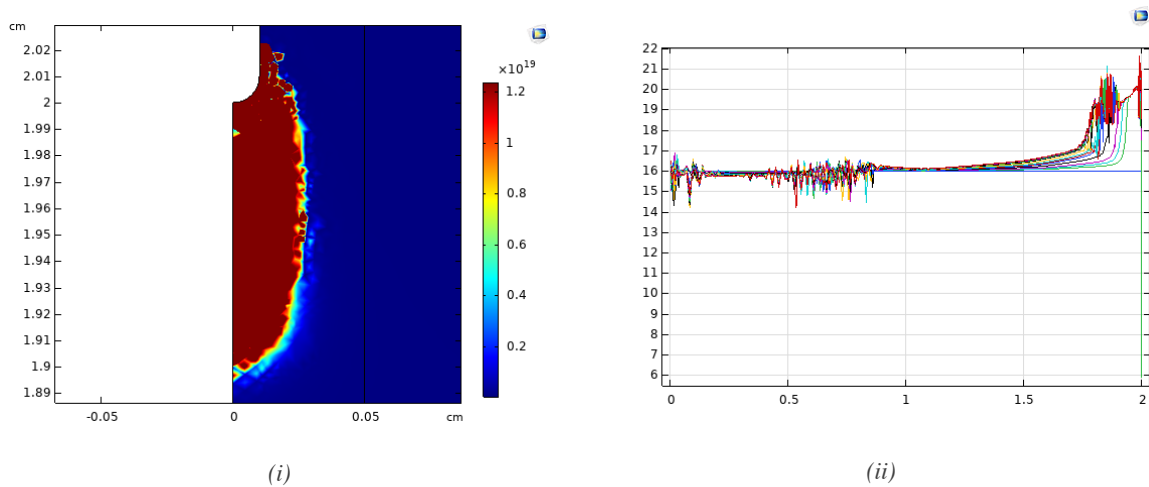


Figure 60 - The 2D surface plot and line graph of the electron density. The numerical instabilities in these plots are seen.